Towards a Human-like Robot for Medical Simulation

NICHOLAS DAVID THAYER

Thesis submitted to the faculty of the Virginia Polytechnic Institute and State University in partial fulfillment of the requirements for the degree of

Master of Science

In

Mechanical Engineering

Committee Chair: Shashank Priya

Committee Member: Daniel J. Inman

Committee Member: Dennis W. Hong

9/2/2011

Blacksburg, VA

Keywords: Humanoid, medical simulator, biomimetic, mechatronic

Towards a Human-like Robot for Medical Simulation

Nicholas David Thayer

ABSTRACT

Medical mannequins provide the first hands-on training for nurses and doctors and help eliminate human mistakes that would otherwise take place with a real person. The closer the mannequin is to mimicking a human being, the more effective the training; thus, additional features such as movable limbs and eyes, vision processing and realistic social interaction will provide a more fulfilling learning experience. A humanoid robot with a 23 degree of freedom (DOF) hand was developed which is capable of performing complex dexterous tasks such as typing on a keyboard. A single DOF elbow and two DOF shoulder was designed and optimized to maintain human form while being able to dynamically lift common household items. A 6 DOF neck and 13 DOF face with a highly expressive silicone skin-motor arrangement has been developed. The face is capable of talking and making several expressions and is used to train the student to pick up on emotional cues such as eye contact and body language during the interview stage. A pair of 3 DOF legs and a torso were also developed which allows the humanoid to be in either the laying down or sitting up position. An algorithm was developed that only activates necessary areas of code in order to increase its cycle time which greatly increases the vision tracking capabilities of the eyes. The simulator was tested at Carilion Clinic in Roanoke VA with several of the medical staff and their feedback is provided in this document.

Acknowledgements

I need to thank all of the people who have shared their time, ideas and laughter over the last three years. I have stories that came from late nights in the lab and late nights downtown that I will tell for the rest of my life. If you are a part of these stories then I am thanking you.

I also want to thank my advisor, Dr. Priya, for all of his guidance and open mindedness. You always listened to my ideas and gave me your time even if you had little for yourself. You are the most dedicated person I know and I know you will continue to do great things for yourself and other people.

Of all people though, I would like to thank my patient wife Amber who has been so understanding of my long hours at the lab. Without her support and care, I would not be where I am today.

Thank you everyone!

Contents

List of Figures

List of Tables

Chapter 1

Introduction and Literature Review

A medical mannequin, or virtual patient, is an intelligent device used in hospitals to give medical students a hands-on learning experience without the risk of injury to a human being. These systems come in various shapes and sizes to simulate a multitude of patients such as babies, the elderly or pregnant women. Some mannequins may only be able to simulate Cardiopulmonary resuscitation (CPR), while others can simulate how a patient will react to several types of treatments over the span of hours. Their capabilities may include drug delivery, suture practice, intubation, pupil dilation, heart rate, respiratory rate, blood pressure, pulse sensing, swelling and internal noises. The closer these mannequins become to mimicking the functionality of a human being, the better the quality of training students receive.

1.1 Review of Medical Mannequins

1.1.1 Literature Review

Here we summarize some important developments in the history of medical mannequins. Medical mannequins have been used in practice since the early 1960s. The first medical mannequin, Resusci-Anne, was used to practice mouth to mouth ventilation. Encouraged by Lind and several other anesthesiologists, Laerdal created Resusci-Anne for practicing mouth to mouth resuscitation [17]. In this early model, the neck had to be repositioned in order to open the airway. Later a spring was added into the chest for simulated chest compression. The first computer controlled mannequin simulator was Sim-One, developed at the University of Southern California in mid-1960s [17]. This lifelike mannequin had many “high fidelity features” including a chest that moved up and down, blinking eyes, dilating/constricting pupils and a jaw

that opened and closed. Sim-One never achieved commercialization, mostly due to expensive computing technology and a narrow market [17].

The next breakthrough in medical mannequin technology was the cardiology mannequin, Harvey [17]. Demonstrated in 1968, Harvey was able to display physical findings such as blood pressure by auscultation, bilateral jugular venous pulse wave forms and arterial pulses, precordial impulses, and auscultatory events which were synchronized with pulse and varied with respiration. Harvey could simulate "a spectrum of cardiac disease by varying blood pressure, breathing, pulses, normal heart sounds, and murmers" [17]. Harvey became a significant part of the medical community in the 1980s when a study showed that medical students performed significantly better on tests after training with the simulator.

The Comprehensive Anesthesia Simulation Environment, or CASE, was the earliest prototype of a mannequin simulator developed for investigating human performance in anesthesia [17]. Developed in 1987, CASE blended a human-like physical structure with a computer model analyzing how drugs affected the physiological characteristics of the human body over time. These characteristics included cardiovascular and respiratory function, acid-base balance, pharmacokinetics and pharmacodynamics [17]. It was also able to simulate multiple interior and exterior physical effects including airway anatomy that could be altered to mimic degrees of difficulty of intubation, palpable carotid and radial pulses, lungs that simulated behavior during spontaneous and controlled ventilation, heart and breath sounds, eyes that opened and closed, and a thumb twitch. During similar time frame, the Gainesville Anesthesia Simulator, or GAS, was developed. GAS aimed to train anesthesia residents in basic clinical skills and was initially outfitted with the ability to diagnose faults in anesthesia machines [17]. Later, a lung simulator was attached and the system was developed into a complete mannequin. The mannequin had a sophisticated lung model which could predict uptake and distribution of anesthetic gases and had sensors that recognized drugs as they were injected [17].

Several companies exist today that sell medical mannequins or partial simulators. However, there are three companies whose products are widely used by hospitals: Gaumard Scientific, METI and Laerdal. Gaumard Scientific [98] has featured a product line of birthing simulator mannequins since the 1990s called NOELLE, shown in figure 1.1 (a) [98]. These systems have many high-fidelity features including changing physiological states, airway

breathing and circulation, vertex, breech and C-section deliveries, maternal and neonatal vital signs monitors, heart and respiratory sounds, speech, convulsions, and a log of caregiver actions which are time stamped. Gaumard also sells a variety of infant mannequins which can be used within NOELLE and can be outfitted with various high-fidelity features. METI [101], a company that was formed through the success of GAS, sells several types of medical mannequins but their most advanced system is a simulator called iStan which is a general educational medical simulator, shown in Figure 1.1 (b) [101]. iStan is capable of breath, heart, bowel phonation and pulmonary system noises, pulse sensing, bleeding and secretion, simulated cardiovascular system, reactive pupils, convulsions and many other detailed trauma and simulated clinical experiences [101]. Laerdal [99] was founded by the inventors of Resusci-Anne. Currently, the company has a product called SimMan 3G, shown in Figure 1.1 (c) [99], which is widely utilized in training schools. SimMan 3G is capable of CPR feedback, convulsions, bleeding and wounds, secretions, drug and event recognition, eye signs such as papillary responses to light and blinking rates, vascular access and chest decompression and drain.

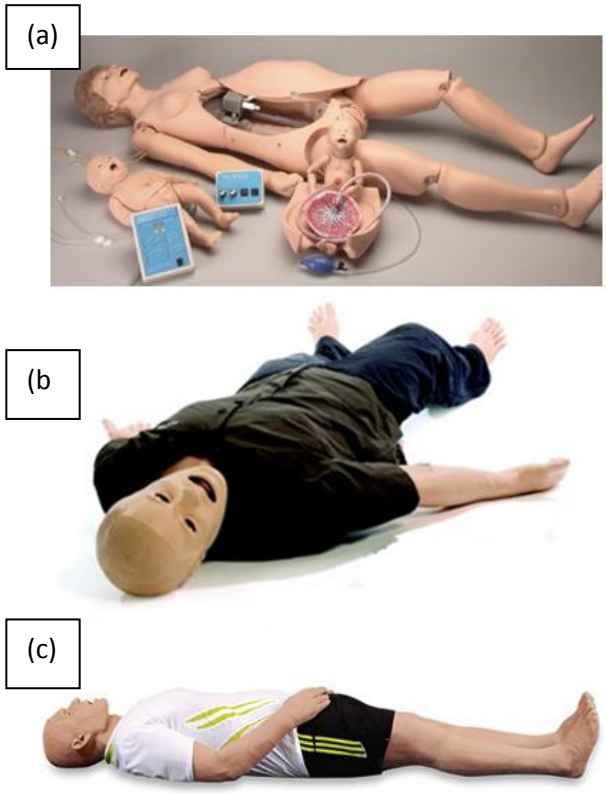

Figure 1.1: Photos of the S575 NOELLE (a), SimMan 3G (b) and iStan (c) medical mannequin simulators [98, 99, 101].

1.1.2 Areas for Improvement

While medical mannequin technology has achieved success in replicating many of the desired medical functions, it is still a far cry from their ultimate goal of simulating a human being. Through collaboration with Carilion Clinic in Roanoke VA, we have identified a few major areas in which medical mannequin technology should be improved.

In terms of actuation or movement, the most sophisticated systems thus far can dilate/construct their pupils, open and close the jaw, blink the eyes or convulse. Convulsion is usually achieved through small solenoid actuators located underneath the body to push the body up and down and from left to right while lying down. No medical mannequins currently have the ability to move their limbs and other joints actively. The majority of medical simulators lay flat or can be adjusted to sit at a low angle thus limiting their application. For instance, during Triage, a patient may be asked to move their limbs to test their range of motion, or follow a pencil with their eyes. Movable limbs would help simulate a seizing patient where limbs may tighten up and shake violently. Perhaps the most useful scenario is the combative patient where a person would resist treatment or even begin flailing their arms and legs. Functionally realistic hands would also help in communicating more of the subtle signs of a patient's symptoms, especially during the Triage stage. During examination, the patient might fold their hands in a position that indicates nervousness about answering which can help a doctor come to a more accurate diagnosis. Also, if the hands are tightly clenched during a physical examination then the patient may be experiencing pain.

Another area that deserves attention is the appearance of the medical mannequin simulators. If the face and body of the mannequin do not look realistic then the medical students may not feel the urgency of the situation since they mentally conceived it as a simple a mechanical system. Thus, the robot must be structurally and functionally similar to the human sensori motor system [52]. A medical simulator is in contact with medical professionals all the time and could be categorized as "social robot". The face in particular deserves careful design and should be outfitted with expressive capabilities instead of the static faces of nearly all

medical mannequins seen today. This is a key to developing a personal attachment with human users [30].

1.2 Overview of Humanoid Hands

1.2.1 Literature Review

Hundreds of robotic hand systems have been developed over the past 50 years. These hands can vary in design from being a static plastic hand to mimicking the exact musculoskeletal structure of a human being. An extensive literature search was performed and the following robotic hands were found to be sufficient, both functionally and aesthetically as an end effector for medical mannequins.

The Gifu Hand III [48] was developed as a prosthetic device with 16 degrees of freedom and is driven with servo motors. This five-fingered design features a large degree of underactuation through 4-bar linkages. Underactuation is a term that describes a system with more degrees of freedom (DOF) than degrees of mobility (DOM), or more joints than actuators. This cuts down on the number of actuators and thus weight which makes this design feature valuable for most prosthetics. Perhaps the most innovative feature of the Gifu Hand III is the large area tactile sensor. The Utah/MIT hand [44] utilizes 32 pneumatic actuators to drive 3 fingers and a thumb through a system of cables. A dense haptic sensing system is integrated with vision to perform trajectory planning. The DIST hand [10] utilizes Bowden cables to provide extrinsic actuation to a four-fingered, 16 DOF hand with 20 brushless DC motors. Bowden cables allows the designer to easily put distance between the actuators and the joint they are trying to move in a wire-driven system. Fingertip force, joint angle and a novel conductive rubber tactile sensor also greatly increase the sensing capability of this hand. The DLR hand II [58] has four fingers, 16 DOF and is driven with 13 BLDC motors with underactuation provided by a 4-bar linkage of two distal joints. Over 90 sensors and an impressive electronics packaging gives this hand great potential for conducting research. The RCH-1 [104] is ultra-light (320 grams) especially with 16 DOF. High underactuation through a passive cable-pulley system allows control of 5 fingers with 6 BLDC motors and makes it a perfect candidate for prosthetics.

The Blackfingers Prosthetic [26] uses 31 pneumatic cylinders to control the 23 DOF in an antagonistic cable setup that almost completely mimics the skeletal structure of the human hand. While this hand is intended for prosthetic use, the necessary hardware for pneumatics makes a portable system very difficult. The SHADOW hand, developed by Shadow Inc., uses 20 air muscles to fluidly actuate a 21 DOF, five-fingered humanoid hand with a 2 DOF wrist. The folding-palm structure of this hand as well as its human-like structure lends it to extremely dexterous manipulation. The Robonaut hand [20], created by NASA, uses 14 BLDC motors to control 14 DOF. Flex shafts and lead screw assemblies are used instead of cables to eliminate frictional problems. Two fingers have a single DOF for grasping which reduces the minimum number of motors and 3 fingers have 3 DOF for precision manipulation. With the addition of 42 integrated sensors, this is a robust tool for manipulation tasks in space.

1.2.2 Design Considerations

When designing a robotic hand there are several key questions that must be answered:

1) What kinds of tasks are required from the hand?

Some of the major consumer arenas for robotic hands include prosthetics, industrial applications (assembly lines, etc) and research (humanoid robots). The answer to this question already tells us a great deal about its design. For instance, prosthetics need to be light weight in order for the customer to be able to use it frequently; therefore, the number of actuators must be reduced thus leading to underactuated designs. Industrial robots are often required to lift several hundreds of pounds so they are less concerned about dexterity and more concerned with have a few large motors and a beefy support structure.

2) Is size an issue?

In the case of medical mannequins, we try to design a system which mimics the musculoskeletal structure of the human body. In this case we are not worried about minimizing the number of actuators but rather striking a balance between functionality and the other issues.

If size were not an issue then designing the robotic hand would be simple, but size is usually coupled with weight and price.

3) Is weight an issue?

Weight and size change proportionally to each other. If size were an issue but weight was not then one may be inclined to design a hand with properly sized actuators but with a support structure made from stainless steel. If weight was an issue but size not then it would make more sense to build a support structure from Styrofoam. Actuator choice also becomes extremely difficult since traditional lightweight actuators usually have fairly poor energy densities.

4) Is price an issue?

Price is always the issue that makes or breaks a design. If price is not an issue then purchasing the high-class, Swiss-made motor for $1500 over the $150 motor from a hobby website, which has a tendency of breaking down after 40 hours, is the obvious choice. Rarely is this the case, so the designer must also be a bargain hunter and be willing to make compromises in design performance. Designing a system for ease of repair becomes extremely important if cheaper components are used.

5) Is noise an issue?

If a medical mannequin is designed to have a trainee listen to heart, breath and digestive noises then it becomes important to eliminate noise from other components. There are two approaches here: purchase components with little noise (usually more expensive), or find a way to shield existing noise by using cases or installing sound absorbing foam.

6) Is power an issue?

This issue spells the difference between a tethered and untethered design. Have components been chosen that draw enough power to be run from batteries or will there always have to be a cord following the robot at all times? Usually, in robotics, the more power something pulls the larger and more expensive it is.

1.3 Overview of Humanoid Heads

1.3.1 Literature Review

Many robotic faces have been reported in literature but only a handful of them are potential candidates for medical simulation robots. Kim et al have developed a robotic head that has a 1 DOF jaw, 2 DOF eyes with internal cameras, 2 DOF neck and movable eyebrows and cheekbones [50]. However, there is no artificial skin that can mimic the complexion and functionality of human skin so the facial expressions are limited in their representation. Minoru Hashimoto et al developed a face with 11 separate muscle groups for creating expression in a silicone based skin [33]. With no neck, eye or jaw movement and cameras for vision, the functionality of this face was limited. Takuya Hashimoto et al developed the popular receptionist robot, Saya, which uses 19 McKibben air muscles for creating expression in a soft urethane resin [34]. A 3 DOF neck, 2 DOF eyes with blinking capabilities and an internal camera was used to create an extremely realistic human appearance with great functionality. Hirth et al have developed the ROMAN head which creates expressions on a silicone skin by moving attachment plates controlled by 11 servo motors [35]. This head had a 4 DOF neck, 6 DOF eyes including blinking with internal cameras capable of stereo vision and a 1 DOF jaw. An emotional architecture was also built into ROMAN that allowed the robot to modify expressions over time with different scenarios. Many of the robotic heads developed by Hanson Robotics are considered the most realistic artificial heads. Albert HUBO has 28 servo motors dedicated for facial expression [70]; however, most of the Hanson's robots do not contain enough functionality to be used as a medical simulator since vision and other medical capabilities are not included. Ishiguro and Nishio have developed several realistic androids with a high number of DOF [43]. Their adult sized robot, Repliee-Q2, has 13 pneumatic actuators to control facial expressions but has to rely on external cameras for information from its surroundings. Spexard et al developed

BARTHOC, a robotic head with a single DOF jaw, 2 DOF eyes with internal cameras as well as facial expression capabilities [85]. BARTHOC has highly developed vision tracking behaviors as well as speech recognition and can shift its attention according to social cues. HRP-4C (AIST) is a full body humanoid robot with a face driven by 11 servo motors [47]. The lips are synced with audio output to enhance its talking realism. HRP-4C is also capable of bipedal walking which is its most impressive feature. EveR-2 has 59 degrees of freedom in the body and is capable of making facial expressions and holding a conversation through a dialog database and visual information from CCD cameras in the eyes [30]. Tadesse et al has twelve shape memory alloy actuators to drive facial expressions and a jaw [88]. This system is housed in a very small workspace, the size of a baby's head, since SMA actuators have very low volumes. Delaunay et al have developed a robotic face that uses a projected image on a semitransparent outer shell to simulate expressions [19]. They claim the advantages are low mechanical complexity and low costs compared to traditional mechanical systems. Another system, "Lilly", utilizes 10 servo motors to actuate facial expressions and 4 to drive a pair of two DOF eyes [90]. The silicone skin has an array of embedded piezoelectric sensors that Lilly can react to when pressed.

The above mentioned robotic facial systems have advanced mechatronic systems but none are equipped to handle the demands placed on medical mannequins and they are not designed particularly for medical simulation. In this study, we address this drawback and describe the design process and analysis for creating a robotic face that can be used by hospitals to enrich the learning experience of medical students.

1.3.2 Facial Expression and their Effects on Perception

Most muscles in the human body provide some type of mechanical advantage that helps us in our survival. Unique muscle sets exist in the face which at one point may have only served a mechanical feature such as opening the mouth or shielding the eyes now serve to assist the communication of intent or mental state. These stereotyped patterns are not actions in which food is found, or opponents or predators pushed away or beaten back. Instead they occur as animals interact, court, dispute over territories, or defer to or dominate one another [28].

Humans have evolved nonverbal forms of communication far beyond that of any other living creature. Slight leans of the body, bends of the neck or gaze directions can mean the

difference between complete attention and boredom. If humanoid robots are expected to fluidly communicate and interact with humans then they should have the ability to convey their emotional state and desires through human-familiar modalities. Communication modalities like gesture, facial expressions, and gaze directions are relevant for interaction, both on the functional as well as on the perceptive side. For developing a robot platform with human-oriented interaction capabilities, it is important that the robot has multimodal communication channels [85].

The authors in [77] have performed a study to identify if a robot's physical attributes can have a significant impact on people's mental models and their response. It was found that the robot's voice and physiognomy (reading traits from facial characteristics) changed people's perceptions of the likeness, knowledge, and sociability. In turn, perceptions of knowledge and sociability changed people's intention to follow the robot's advice. Another study showed how the expressive degrees of freedom of a robot's head and face affect people's social responses toward it in a self-disclosure task [55]. In this study, the robot asked a human participant a number of questions of varying degrees of intimacy where some are more intrusive than others. It was concluded that as the number of expressive degrees of freedom increased so did the willingness to disclose information. The results of these studies indicate that people apply mental models (a perception of intelligence and social aptitude) to robots with human-like attributes or communication abilities.

Techniques for fabricating humanoid robots have improved to the point that some exterior features are nearly indistinguishable from humans. However, due to the complexity of human social interaction and brain function, behavioral algorithms are still far from achieving near-human capabilities. The gap between appearance and ability often leads to disappointment and misnomers about humanoids. As discussed by Foner [27], people's expectations based on strong anthropomorphic paradigms overly increase a user's expectations of the system's performance. In situations where the robot is a source of information for a person, the person's beliefs about the quality of that information is important. Particularly in educational applications, the learner must believe that the information coming from the robot is reliable [49]. Since the humanoid discussed in this thesis is intended to be used as an educational tool for medical students it is important to match the system's capabilities to the expectations of the users

otherwise the simulations may not be taken seriously and the quality of the training could be compromised.

1.3.3 Design Considerations

When designing a robotic head the main issue that will arise again and again is space. It is assumed that when designing a head it will be of human dimension since humans are so keen on picking up small discrepancies between the size and symmetry of faces. The authors in [37] sum it up, "The most difficult is the face. People's reactions will really change depending on whether the face is good or bad." A small workspace usually means a performance sacrifice. This is why so many medical mannequins have static faces and eyes that do not move because they need room for intubation simulation and their respective supply lines and papillary reaction.

Skin properties are also very important because medical mannequins are usually subject to harsh conditions. They are bumped and cut all the time so there needs to be a balance between required toughness and feeling. Also, the tougher the skin the more force your actuators will have to output in order to make facial expressions.

If a neck will supplement the design then keeping weight down is also important as the heavier the head is the larger the actuators will have to be for the neck. Also, depending on orientation and the type of mechanism used for the neck, centering the weight of the head over the neck mechanism will keep you from accidently overloading one of your actuators.

Another issue that is typically overlooked is cable management. It is more difficult than it seems to design an inconspicuous path for power and signal cables. This is more an issue with a robotic head since there is little room for a power supply and computer within the head itself.

1.4 Artificial Muscle Overview

As with any mobile robotic system, actuators must be chosen carefully. Selecting actuators too small results in not enough torque for the system to perform as expected therefore the risk of causing damage to equipment is increased. Choosing actuators too large makes it difficult to package other components such as power management and control electronics.

Larger electromagnetic actuators also run the risk of emitting electromagnetic interference which could cause nearby electronics to stop working properly.

An actuator is simply a transducer which takes some form of energy and transforms it into motion. There are the traditional actuators like electromagnetic motors, pneumatics, gas and steam engines and hydraulics which have existed for decades and have been well studied to the point where high efficiencies are achieved. Then there are non-traditional actuators like electroactive polymers, or EAP which are in their early stages of development but may prove to be a candidate for mimicking biological tissues. As more robotic systems are being developed that utilize flexible electronics and energy storing components, the need for an actuator with similar properties is needed. State of the art "soft" robots and how they closely mimic biological systems are discussed in [93]

A muscle-like technology would be of enormous benefit, particularly for medical implants and human assist devices [39]. The work in [31] documents the properties of mammalian skeletal muscle and derived typical actuation parameters including strain ~20%, stress ~0.1 MPa, and specific power ~50 W/kg. None of the proposed actuators in the literature yet meet all the specifications of natural muscle. Recently, conducting polymer actuators have attracted considerable attention for application in artificial muscles as they have great potential to meet the above mentioned criteria. High molecular weight polypyrrole (PPy) actuators have the potential to generate large stresses (34 MPa), strains up to 12% and specific power to mass ratio of 150W/kg at low driving voltages. Geometrical structures synthesized from conducting polymer composites have shown improved performance at low operating voltages [89, 91].

Several robotic systems exist that mimic biological systems, [1, 36, 53], and as the size of robot decreases the tendency to utilize electroactive polymers (EAP) as actuators has been increasing due to their small profiles and high volumetric efficiency. Electric motors are attractive because they feature high continuous power per unit mass (up to 300 W/kg when using rare earth magnets) [100] but the transmission system is heavy which increases size and reduces efficiency bringing the overall power per unit mass down to or below that of muscle [64]. Natural muscle is very compliant and can store energy while in tension. Since a highly geared electric motor cannot reproduce the compliance of natural muscle, it is necessary to include additional elements (such as springs and dampers) to provide muscle-like features [39].

Information from [51, 65, 75, 89, 91] was used to create table 1.1. Some of the characteristics of these actuators were not published so those slots were left blank. This data was modified to include drive voltages, controllability and the existence of a zero-energy holding state. Easy controllability would be low voltage, low current and a drive signal that is easily provided. Moderate controllability means there may be a high drive voltage or a special driving signal required to properly actuate. Difficult controllability would be a combination of high drive voltages and currents as well as specific driving signals and perhaps requires additional components to control position or speed. A zero-energy holding state is where the actuator maintains its current position without supplying any energy.

Table 1.1: Comparison of actuator technologies

Actuator Type	Strain (%)	Pressure (Mpa)	Energy Density (J/cm^3)	Efficiency (%)	Relative Speed	Drive Voltage (V)	Control	0-Engy. Hold State?
Natural Muscle	>40	0.35	0.07	>35	Medium	N/A	Difficult	no
Electric Motor	*	>500	~0.5	>90	Fast	~12	Easy	no
Hydraulics	50	>500	*	-	Medium	*	Easy	yes
Cylinder Pneumatics	50	>500	*	-	Medium	*	Difficult	yes
Pneumatic Air Muslces	35	900	~0.9	-	Medium	~12 V	Difficult	yes
Silicone (ESP)	32	0.21	0.034	90	Fast	200	Difficult	no
Polyurethane (ESP)	11	1.9	0.1	80	Fast	1e6	Difficult	no
P(VDF-TrFE) (ESP)	4	15	0.3	30	Fast	3e7	Difficult	no
Acrylic (DE)	215	7.2	3.4	80	Medium	3e7	Difficult	no
Silicone(CF 19-2186) (DE)	63	3	0.75	90	0.001	250	Difficult	no
Electrostatic devices (integrated force array)	50	0.03	0.0015	90	Fast	-		no
Ceramic (PZT)	0.2	110	0.1	90	Fast	500	Difficult	no
Single crystal (PZN-PT)	1.7	131	1	90	Fast	500	Difficult	no
PVDF (PZT)	0.1	4.8	0.0024	5	Fast	500	Difficult	no
MFC (d33 mode)	0.45	60	5	15	Fast	1500	Difficult	no

Electromagnetic (voice coil)	50	0.1	0.025	90	Fast	-		no
SMA (NiTi)	5	200	5	10	3	16	Moderate	no
BISMAC (NiTi)	110	0.003	0.003	1	slow	16	Moderate	no
SMP (polyurethane)	100	4	2	10	100	10	Moderate	no
Conducting Polymer (average)	12	34	0.1	15	20	10	Difficult	yes
(TFSI-doped PPy)	37	1	0	1	Slow	10	Difficult	no
Strip PPy	18	0.44	0	0	Slow	8	Difficult	no
Zigzag PPy-PVDF	20	0.21	0	0	Slow	12	Difficult	no
Conducting Polymer (polyaniline)	10	450	23	1	3	1	Difficult	no
IPMC	5	15	0.005	2.9	Medium	7	Difficult	no
Liquid crystal elastomer	45	0.45	0.056	5	Medium	5e5	Difficult	no
Carbon nanotubes	1	20	0.04	1	Medium	2	Difficult	no
Molecular actuators	20	1	0.1	0	-	2	Difficult	no
MCP/gels (polyelectrolyte)	60	0.3	0.06	30	Slow	10	Difficult	no
Terfenol-D, Etrema Products	0.2	70	0.025	60	Fast	(mag. field)	Difficult	no

* Depends on additional system characteristics

~ Rough or average

Chapter 2

Biomimetic Hand, Arm and Shoulder

2.1 Actuator Selection

2.1.1 Actuator Comparison and Selection

Our goal is to create a biomimetic hand which can function similarly to a human in order to convey information about the patient state. At the same time we do not wish to limit ourselves only to this application. We also want this robotic hand to be nearly as dexterous as the human hand in order to be able to perform activities of daily living (ADLs) which include opening doors, reaching objects from shelves and dressing ourselves. We decided that typing on a keyboard would serve as a good benchmark for a successful design since, as [46] puts it, "Typing and piano playing are often considered to be among the more complex forms of skilled serial action performed by human beings." If it can type on a keyboard, it can open doors, reach objects from shelves and dress itself.

Several actuators such as pneumatics, hydraulics, brushless direct-current (BLDC) motors, servo motors, air muscles, shape memory alloy and electroactive polymers were considered. Pneumatics and hydraulics were eliminated from consideration due to bulky system requirements like regulators, filters and tanks which significantly reduces their energy density. Air muscles were eliminated due to their size and difficulties with control stemming from highly nonlinear behavior. We knew there were several commercially available BLDC and servo motor options that would work in our system but we decided to investigate the use of EAP actuators first.

In order to determine which EAP actuators would work for this application we must first compare existing technologies. The compiled data for EAP actuators in table 1.1 was used to create the graphs shown in figure 2.1.

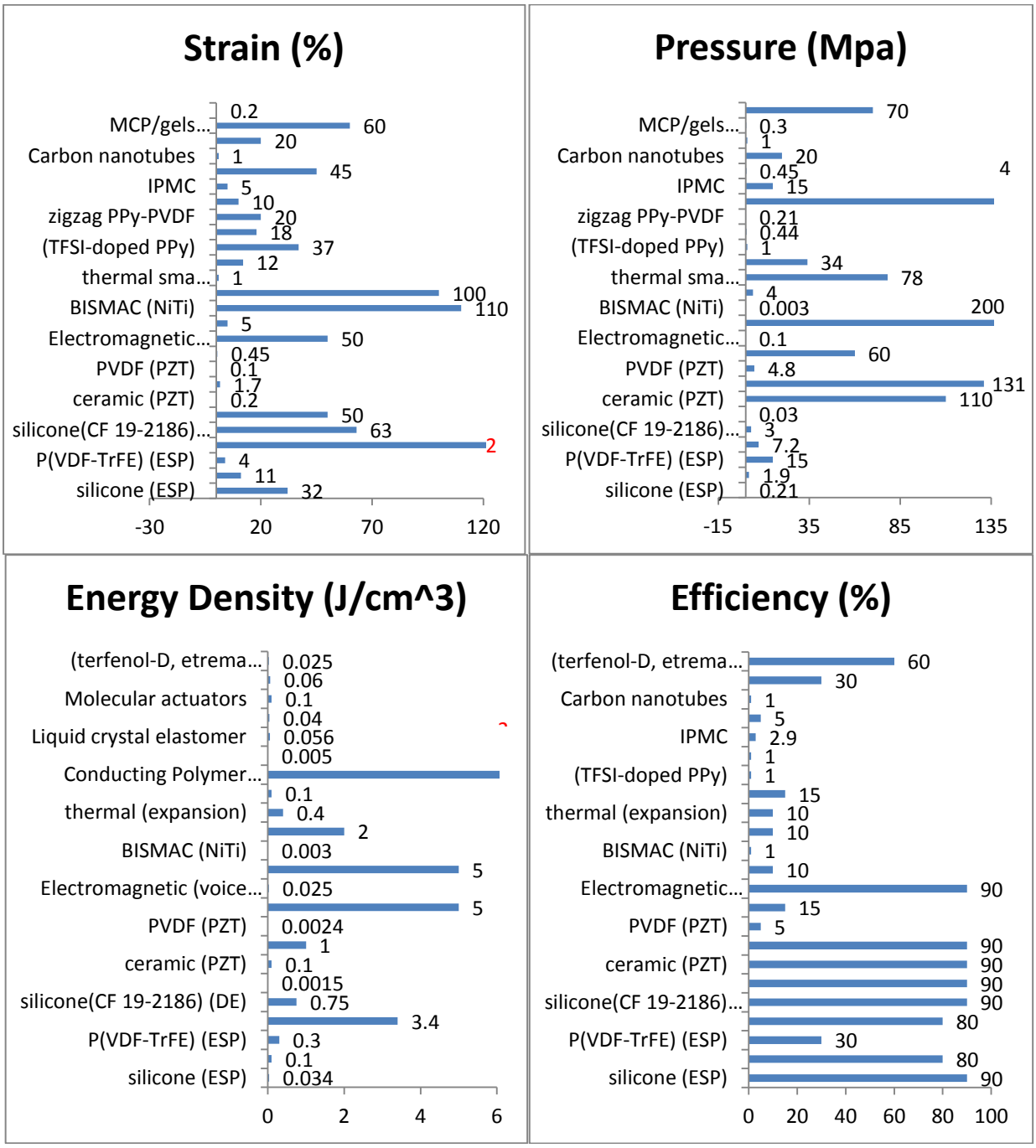

Figure 2.1: Comparison of strain, pressure energy density and efficiency for commonly used EAP.

EAP with incomplete data were excluded from their respective plots and analysis. A simple cost function was created by multiplying the values of strain, pressure, energy density and efficiency for each actuator (units – $kg^2*cm^{-3}*s^{-4}$). The EAPs with the highest cost function value

are the ones that present immediate possibility for application in the robotic hand. Actuators that do not have available characteristics either in published literature or company technical specifications were excluded from the cost function analysis. Table 2.1 shows the attractive options (cost function value over 500) and their relevant properties.

Table 2.1: Candidate EAPs for hand application

Actuator Type	Strain (%)	Pressure (Mpa)	Energy Density (J/cm^3)	Efficiency (%)	Response Time (sec)	Drive Voltage (V)	Cost Function Value
Conducting Polymer (polyaniline)	10	450	23	<1	3	1	103500
Conducting Polymer (overall)	12	34	0.1	15	<40	10	612
SMP (polyurethane)	100	4	2	10	100	-	8000
SMA (NiTi)	5	200	5	10	3	-	50000
MFC (d33 mode)	0.45	60	5	15	<0.01	1500	2025
Single Crystal (PZN-PT)	1.7	131	1	90	<0.01	500	20043
Silicone(CF 19-2186) (DE)	63	3	0.75	90	<0.01	250	12758
Acrylic (DE)	215	7.2	3.4	80	<0.1	30000000	421056

"Conducting polymer (overall)" is an overall average of CP characteristics and should not be thought of as representing any one particular type of CP.

We now narrow down the list by excluding single crystal PZN-PT, MFC, silicone and acrylic dielectric elastomers as potential candidates since their driving voltage is high (>250V) which is cumbersome for autonomous systems due to large power supplies. Response time is very important in a robotic system tying to mimic biology; therefore, shape memory polymer (SMP) can be excluded from consideration due to their large cycle response time (~60 sec). Polyaniline can also be excluded from consideration due to its low efficiency (<1%). This leaves NiTi shape memory alloy as the best suited actuator for the robotic hand.

NiTi shape memory alloy (SMA) is a wire-type actuate that can produce large pressures and at the diameter of a human hair can output 15 N of linear force. NiTi SMA can only constrict 5% of its overall length so as long as the actuator is long enough, we can achieve the types of displacements we want. The only catch with this actuator is that it has a thermal response time of around 3 seconds (for 100 μm) to go from extended to constricted and back to the extended position. Since the human hand can go from fully open to closed in less than a second it is important for us to try to reduce the response time of this actuator as much as possible. Other characteristics such as the effects of cyclic loading and heat transfer from the SMA would also be important to know for modeling purposes.

2.2 Shape Memory Alloy Thermal Characterization

2.2.1 Literature Review

Shape memory effect is generally referred to as the recovery of original shape from deformed shape with residual strain through thermal cycling. The superelastic behavior found in shape memory alloys (SMAs) is defined as the recovery of large strain by mechanical cycling under constant temperature [72].

Prior studies on SMA actuators indicate that there are challenges in terms of achievable velocity [76]. In order to overcome the problem of response time, the authors in [79] proposed the use of SMA coupled with fluid cooling system to realize torsional actuator. The authors in [7] have proposed SMA springs coupled with fluid cooling system for similar purpose and obtained a cutoff frequency of 2.0 Hz using a 0.5mm diameter coiled wire. [83] proposes the use of a mobile sink that uses a friction clutch mechanism to cool a rotating lever arm. They determined that temperature feedback could help the cooling time by preventing the wire from overheating. [63] implemented a series of Peltier modules to characterize the improvement in response time in SMA. Their results yielded a decrease in response time by 10 times, but it was still too slow to use in most robotic systems. [60] ran a SMA wire through a small metal tube filled with silicone grease that had a high thermal conductivity and reported a frequency response of 0.2 Hz but the power consumption was too high. [41] improved the response time of SMA by providing the wire a brief but large pulse of current. This improved the recovery time of the wire

but displacement was less than a millimeter for each cycle, which may not be suitable for some robotic systems. [38] suggests pneumatic cooling for controlling a tactile display. They managed to reach a working frequency of 6-7 Hz through air cooling. All of these prior reported methods yielded some improvement but are not directly applicable towards using SMA in compact areas demanding large strain and force with minimum power consumption. There are several studies that describe methods for rapid heating of SMAs [78], but our objective is to achieve low overall response time.

SMA actuators based on nickel and titanium (NiTi) are commercially available in wire forms. Two widely used SMA wires known as Flexinol (Dynalloy Inc., USA) and Biometal fiber (Toki Corporation, Japan) have been demonstrated in variety of applications. Biometal fiber is being experimented for applications in robotics, micro-gripper, artificial arm, and wing morphing. Implantable artificial myocardium has been proposed using Biometal fiber to mimic natural ventricular contraction [84]. Biometal fiber has also been demonstrated as a variable damping isolator to enhance precision of optical equipments on-board satellites [69] and Jellyfish unmanned underwater vehicle [94]. Flexinol has been demonstrated in various applications including a robotic-eye system [14], prosthetic hands [60, 61], and robotic manipulator [2]. An anti-glare rear-view mirror based on SMA actuation has been demonstrated by [62] for automobile application where silicone elastomer coating was used to reduce the cooling time as well as thermal stress in SMA. Thus, both of these commercial SMAs are important actuator systems with potential in practical applications.

2.2.2 Thermal Model of SMA

Determining the heat transfer coefficient can provide insight into the phenomena associated with different types of active cooling techniques. The heat transfer coefficient of SMA wires can be obtained mathematically by assuming a lumped capacitance model. A lumped parameter model works on the assumption that the hot wire is suddenly submerged in an infinite medium with constant temperature. In order for the model to be valid we assume that the wire must be thin enough that it has no internal thermal gradient. For these assumptions to be valid, the Biot number defined by equation (2.1) has to be much less than 1.

$$Bi = \frac{hL_c}{k} << 1, \qquad [2.1]$$

where *Bi* is the Biot number, *h* is the average heat transfer coefficient $\left[W/m^2K\right]$, L_c is the characteristic length in meters , and *k* is the thermal conductivity of SMA $\left[W/m*K\right]$. If equation (2.1) is satisfied then the transient temperature can be obtained from lumped capacitance heat transfer equation [42] and given by equation (2.2) as:

$$\dot{T} = -\frac{hA}{\ell Vc}\left(T - T_\infty\right), \qquad [2.2]$$

For constant convective heat transfer the solution is given by equation (2.3):

$$T = T_\infty + \left(T_i - T_\infty\right)e^{\lambda t} \qquad [2.3]$$

Where $\lambda = A_S h/\ell vc$, ℓ the density, C is the heat capacity, *V* is the volume, A_s is the surface area, *t* is the time, *T* is the temperature of the wire, T_∞ is the ambient temperature, and T_i is the initial temperature of the wire. Note that equation (2.3) is a simplistic equation, which can be used to study the heat transfer coefficient for active fluid cooling.

2.2.3 Experimental Setup for Active Cooling

In this section, we describe the method used to characterize the heat dissipation from SMA wires and discover a suitable active cooling mechanism for our robotic medical simulator. We investigated various suitable active cooling techniques such as free and forced convection in air, liquid media and heat sink. Each of these methods were tested and compared with natural convective cooling in ambient air. Figure 2.2 shows the experimental setup used to study the effect of active cooling techniques

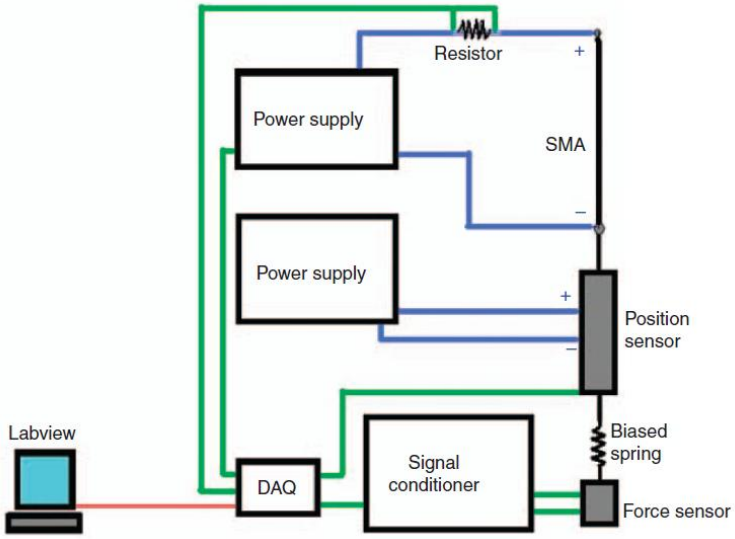

Figure 2.2: Schematic diagram of the experimental setup to test active cooling techniques.

The electrical power for driving the SMAs was supplied from a Agilent Dual output E3648A, DC power supply at the recommended operating values, 180mA for Flexinol and 200mA for Biometal. A Novotechnik T-Series position sensor with a resolution of 0.002mm and stroke-length of 50mm was used to measure displacement. The SMA wire was mounted to a rigid surface and fixed to the position sensor at one end. The other end of position sensor was connected to the force sensor with a bias spring to assist the SMA in returning to its original position during cooling. Input current was measured by inserting a known resistance in the current loop and measuring the voltage across it. NI 9215 DAQ system with a 4-input voltage module was used to collect the incoming analog data. A LabVIEW program was created to read voltages from from DAQ at a frequency of 1000 Hz. These voltages were then converted into current, force and displacement using the transfer functions of the transducers. The experiment was conducted on a vibration isolated table to prevent any interference from external sources. All of the experiments were under repeated identical conditions to ensure the consistency of measured data.

2.2.4 Active Cooling Experimental Procedure

This section describes the procedure for collecting and processing the data on heat dissipation from both Flexinol and Biometal SMA wires. Figure 2.3 (a) shows the setup for

characterizing the response time of SMA wire with a heat sink. For this experiment, an aluminum tube was used as the sink. As soon as the voltage to SMA wire was cut off the tube was allowed to make contact with wire. Careful experimentation was conducted to push the aluminum tube immediately in contact with SMA wire while voltage was being shut off. The aluminum tube was as long as the contracted length of SMA wire (~185 mm) and had a diameter of 26mm and thickness of 2 mm. The next active cooling method tested was using thermal gel shown in figure 2.3 (b). This method is similar to that reported by [60] where the SMA wire was run through a small copper tube that was filled with thermal grease (Arctic Silver) which had a thermal conductivity of 8.9 W/mK. This provides the SMA wire a large surface area to dissipate heat rapidly. Figure 2.3 (c) shows the setup for low-speed forced convection. An air speed of 0.3 m/s was achieved by using a 12V computer fan and confining the flow within a rectangular channel of dimensions 40mm width by 89mm height by 245mm length. The second high-speed forced air convection was achieved by using compressed air, a hose and nozzle. The experimental setup in figure 2.3(d) shows the SMA wire running through an 8.9mm diameter carbon fiber tube with an incoming air-speed of 4.6 m/s. The carbon fiber tube covered almost the entire length of SMA wire, which was suspended inside the tube. Since the velocity of airflow was high and the thermal conductivity of carbon is low, we can neglect heat transfer from the SMA wire to the tube. The last active cooling method tested was fluid quenching shown in figure 2.3 (e). Using a carbon fiber tube, water was injected onto the wire via a syringe at velocity of 2.7 m/s. All of these experiments were first conducted on Flexinol wire and then the cooling methods that yielded the highest decrease in response times were experimented on Biometal fiber.

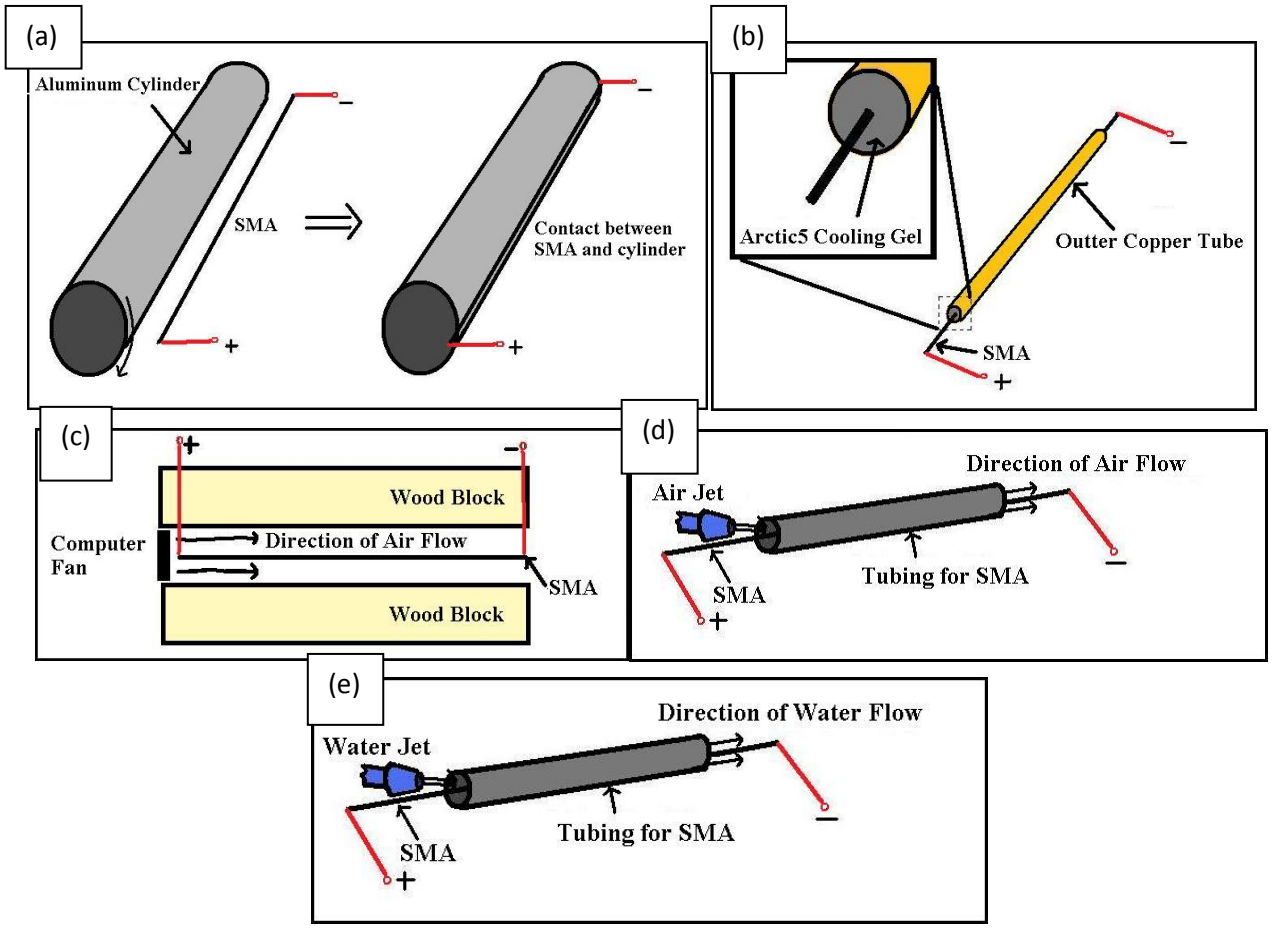

Figure 2.3: Illustration of various active cooling methods: (a) heat sink, (b) thermal gel, (c) top view of low-speed air, (d) high-speed air, (e) fluid quenching

2.2.5 Effect of Cooling on Response Time

In this section, the response time of SMAs is compared utilizing the active cooling methods described earlier as well as variable initial conditions. Figure 2.4 shows the comparison between various methods of active cooling and the changes in profile of thermal response of a 195mm long, (a) 127 mm diameter and (b) 100 mm diameter Flexinol wire while being cooled from maximum strain state. The black line shows the response of SMA wire with no active cooling (ambient cooling) and as is evident from the figure, takes the longest time to reach the undeformed state (~1.6 s to reach zero percent strain). The fan cooling had a small effect on the response time, reducing it by 0.5 s as compared to ambient cooling. This may be due to the fact

that the fan needs some time itself to achieve maximum velocity. It may also be related to the fact that air flow takes some time to reach the end of channel where the SMA is mounted.

The data for thermal gel was neglected because the SMA wire failed to contract. There could be two possible reasons for this behavior: (i) the thermal gel is dissipating heat rapidly during actuation and thus the wire cannot retain enough heat to contract completely, and (ii) the SMA could not produce enough force to overcome the viscosity of thermal gel. Contraction was eventually produced by increasing the magnitude of current running through the wire from 0.2 A to 2 A. Using this much current is not practical and thus active cooling using thermal gel will not be discussed any further. The other three cooling methods, high-speed forced air, heat sink, and fluid quenching were found to be the most effective. Fluid quenching reduces the cooling time by 88% while the heat sink and forced air reduced the cooling time by 75% s. Also, smaller diameter wire leads to faster cooling times due to less energy being contained within the wire at a cost of lower actuation force. It is expected that Biometal fiber will follow a similar trend as a function of diameter.

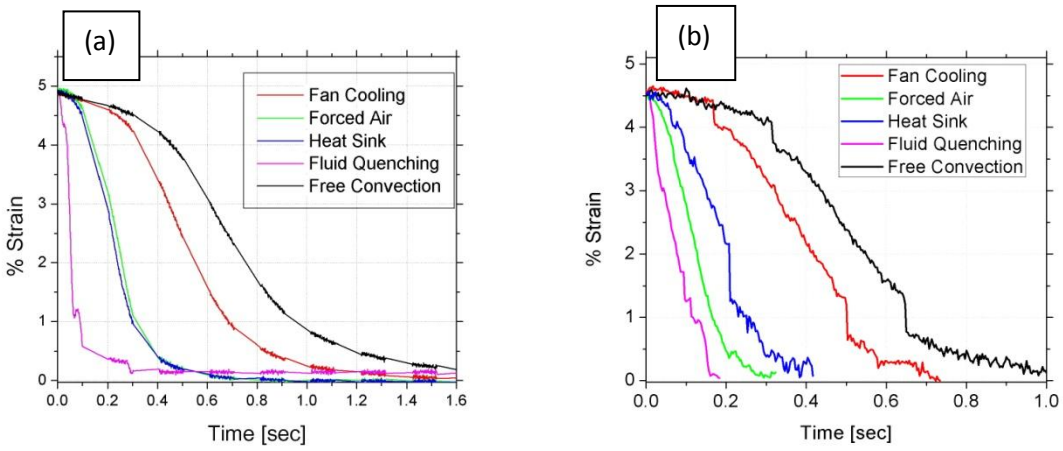

Figure 2.4: The thermal response times of Flexinol SMA wire for four active cooling methods: (a) 127 μm diameter, and (b) 100 μm diameter.

Figure 2.5 (a)-(c) compares the thermal response times for Flexinol and Biometal fiber using forced air, heat sink, and fluid quenching. Biometal fiber did not reach the same level of displacement as Flexinol and may be related to slight difference in pretension of the wire. Since the transformation temperature of Biometal wire (70^{o}C) is 20^{o}C less than that of Flexinol it shows faster response time in all of these three active cooling methods. These results are quite

interesting and in conjunction with the results presented in figure 2.4(above), it can be summarized that response time of Biometal fiber can be increased (reducing the delay) by active cooling without significantly affecting the generated force-displacement.

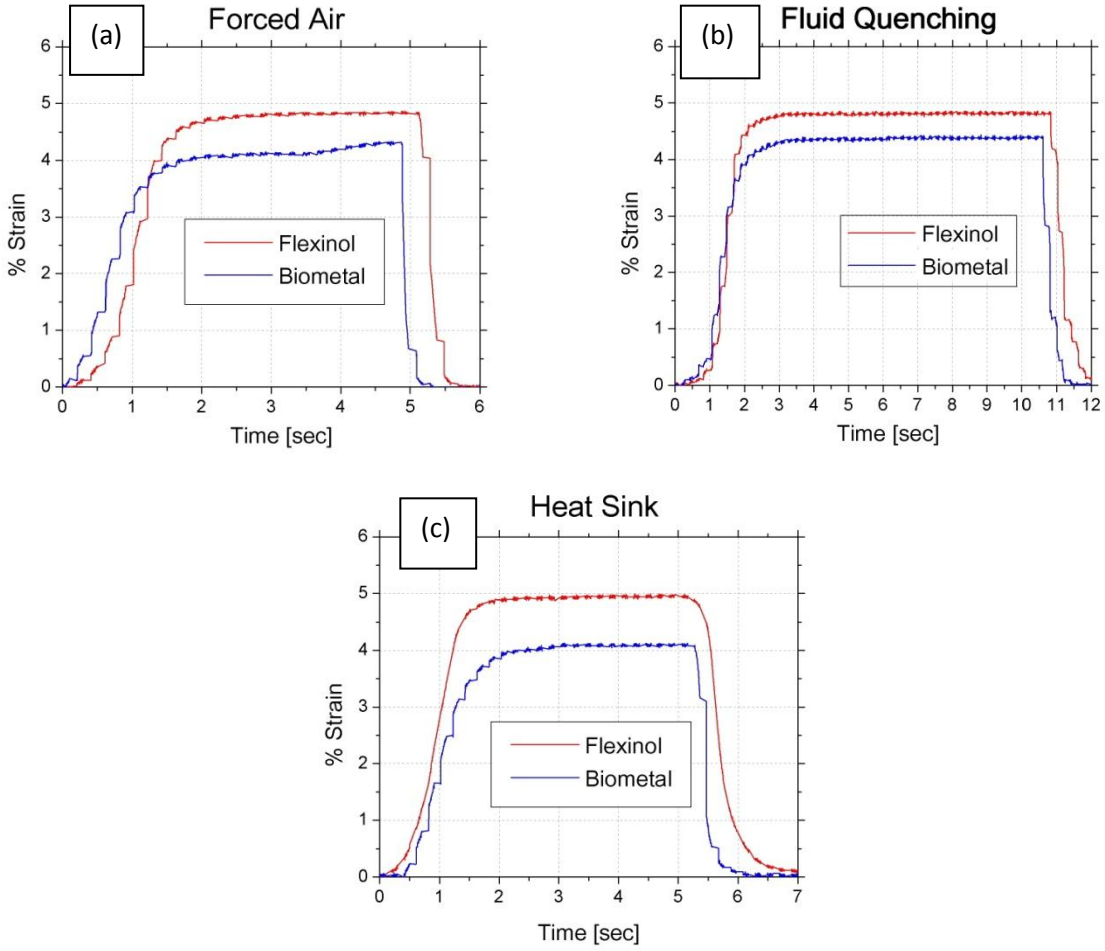

Figure 2.5: Comparison of response times for Flexinol and Biometal wires with three different active cooling methods: (a) high-speed air, (b) fluid quenching, and (c) heat sink.

2.2.6 Energy Dissipation during Heating

SMA wires contract due to phase change from martensite to austenite, which is dependent upon the temperature. Therefore, if a wire is dissipating heat while it is being heated, the phase change will not occur unless the heating method is generating enough energy to overcome the dissipation. Since SMAs are traditionally heated by passing current through the wire, the effects of heat dissipation can be overcome by applying more current. Figure 2.6 shows the initial strain in Flexinol wire at different currents and its thermal response after current is cut

off while being cooling with the 12V computer fan. In this case, an increase in current by 44mA results in an increase of strain from 1% to 3.3% while the computer fan was on during the heating cycle. Since our goal is to find the best method for increasing the response time while keeping the electrical power consumption small, we can conclude that any cooling during the heating cycle will negatively affect performance.

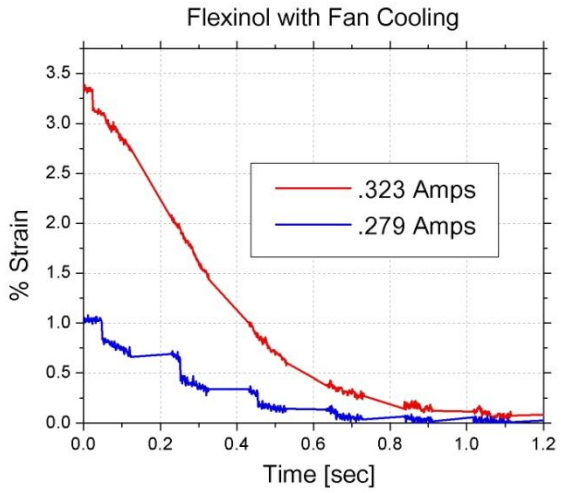

Figure 2.6: Behavior of SMA wires for low-speed air cooling methods during the heating phase with two current amplitudes.

2.2.7 Martensite Fraction

Determining the fraction of martensite within the SMA is important because it is directly related to strain. Since martensite fraction is also related to temperature, we can form a bridge between martensite fraction and strain through temperature data. The fraction martensite equation as a function of temperature can be obtained from the kinetic law. The characteristic curve for SMA actuators is shown in figure 2.7 (a) showing four transition temperatures; Ms and Mf are the martensite start and finish temperature, and As and Af are the austenite start and finish temperatures.

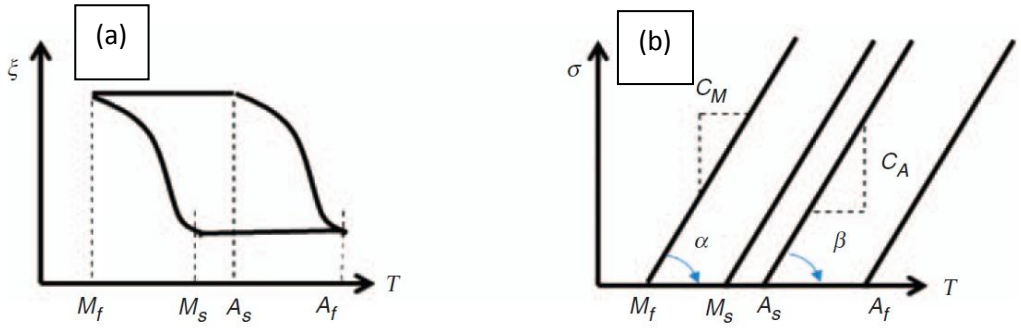

Figure 2.7: Characteristic curve for SMAs: (a) fraction of martensite as a function of temperature and (b) stress vs. transition temperature showing the four characteristic temperatures: M_f, M_s, A_s, A_f.

Considering the austenite-martensite and martensite-austenite transformations as harmonic functions of cosines, the fraction of martensite can be expressed as [56]:

$$\xi_{M-A} = 0.5\left\{\cos\left[a_A\left(T - A_S\right)\right] + 1\right\} \qquad [2.4a]$$

where $a_A = \pi / A_f - A_s$, and ξ_{M-A} is the martensite fraction going from martensite to austenite.

$$\xi_{A-M} = 0.5\left\{\cos\left[a_M\left(T - M_f\right)\right] + 1\right\} \qquad [2.4b]$$

where $a_M = \pi / M_s - M_f$, and ξ_{M-A} is the martensite fraction going from austenite to martensite.

The equations above are suitable for the case of zero applied stress. If pre-stress is applied on the SMA actuator, the transformation temperature changes and a modified form of equation (2.4) should be utilized as follows:

$$\xi_{M-A} = 0.5\left\{\cos\left[a_A\left(T - A_S\right) - \frac{a_A}{C_A}\sigma\right] + 1\right\} \qquad [2.5a]$$

$$\xi_{A-M} = 0.5\left\{\cos\left[a_M\left(T - M_f\right) - \frac{a_M}{C_M}\sigma\right] + 1\right\} \qquad [2.5b]$$

Figure 2.7 (b) illustrates the relationship between the transformation temperature and stress. The slope of stress and transformation temperature provides the value of CA and CM, which corresponds to the austenite and martensite, respectively.

The fraction of martensite can be determined indirectly from temperature versus time behavior during heating and cooling in combination with equation (2.5). The required temperature versus time curve can be obtained by creating a relationship between two sets of experimental data corresponding to strain versus time and strain vs. temperature. The strain versus temperature behavior of SMA during heating and cooling cycle is shown in figure 2.8. In this case, the strain data was recorded by a position sensor while the SMA was being heated in a furnace. The furnace was heated from room temperature (26^{o}C) to 150^{o}C and then cooled again to room temperature. A standard K-Type thermocouple was used for measuring the temperature. The temperature and strain data were collected multiple times using the same DAQ system as in the previous experiment to confirm the behavior.

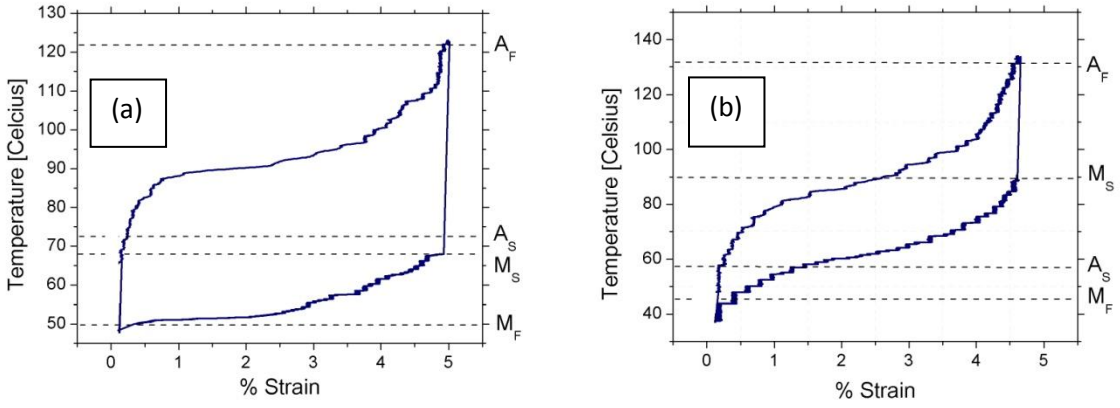

Figure 2.8: Experimental heating and cooling curves for (a) Flexinol and (b) Biometal.

The graphs shown in figure 2.8 (a) and (b) are average results from multiple repetitions for both Flexinol and Biometal fiber, respectively. By fitting a polynomial curve to the cooling cycles, a relationship between strain and temperature can be obtained for both types of SMAs. Equations (2.6a) and (2.6b) are given for Biometal fiber and Flexinol, respectively. This equation can then be used to transform the strain versus time data, which was measured for various active cooling methods separately into temperature versus time data.

$$T = 0.078\varepsilon^5 - 0.86\varepsilon^4 + 4.7\varepsilon^3 - 15\varepsilon^2 + 28\varepsilon + 36 \quad [2.6a]$$

$$T = -0.057\varepsilon^4 + 0.68\varepsilon^3 - 1.6\varepsilon^2 + 2\varepsilon + 50 \quad [2.6b]$$

Once the temperature profile as a function of time, *T(t)*, is known it can be inserted into equation (2.5). The characteristic temperatures, M_s and M_f can be found from figure 2.8 (Biometal: $M_S = 85^\circ C$, $M_F = 45^\circ C$ and Flexinol: $M_S = 68^\circ C$, $M_F = 49^\circ C$) while a commonly used average value of $C_M = 8MPa/^\circ C$ for Flexinol [68, 105] and $C_M = 5.88MPa/^\circ C$ was taken from the slope of stress versus transformation temperature for Biometal fiber. Stress was calculated from the deformation length of biasing spring (172 MPa). Figures 2.9 (a) and (b) show the variation of martensite fraction as a function of time calculate using Equation (2.5b).

As can be observed from figures 2.9 (a) and (b), both Biometal and Flexinol exhibited fast transformation from austenite to martensite during fluid quenching. Using the data in this figure, a strain vs. martensite fraction plot can be constructed as shown in figure 2.9 (c) for both Flexinol and Biometal fiber. Figure 2.9 (c) is characteristic curve for various methods of cooling investigated in this study because the martensite fraction is directly related to the percent strain generated. It can also be observed from this figure that Biometal fiber exhibits zero martensite fraction at lower strain magnitude which implies that Flexinol has slightly higher contraction percentages.

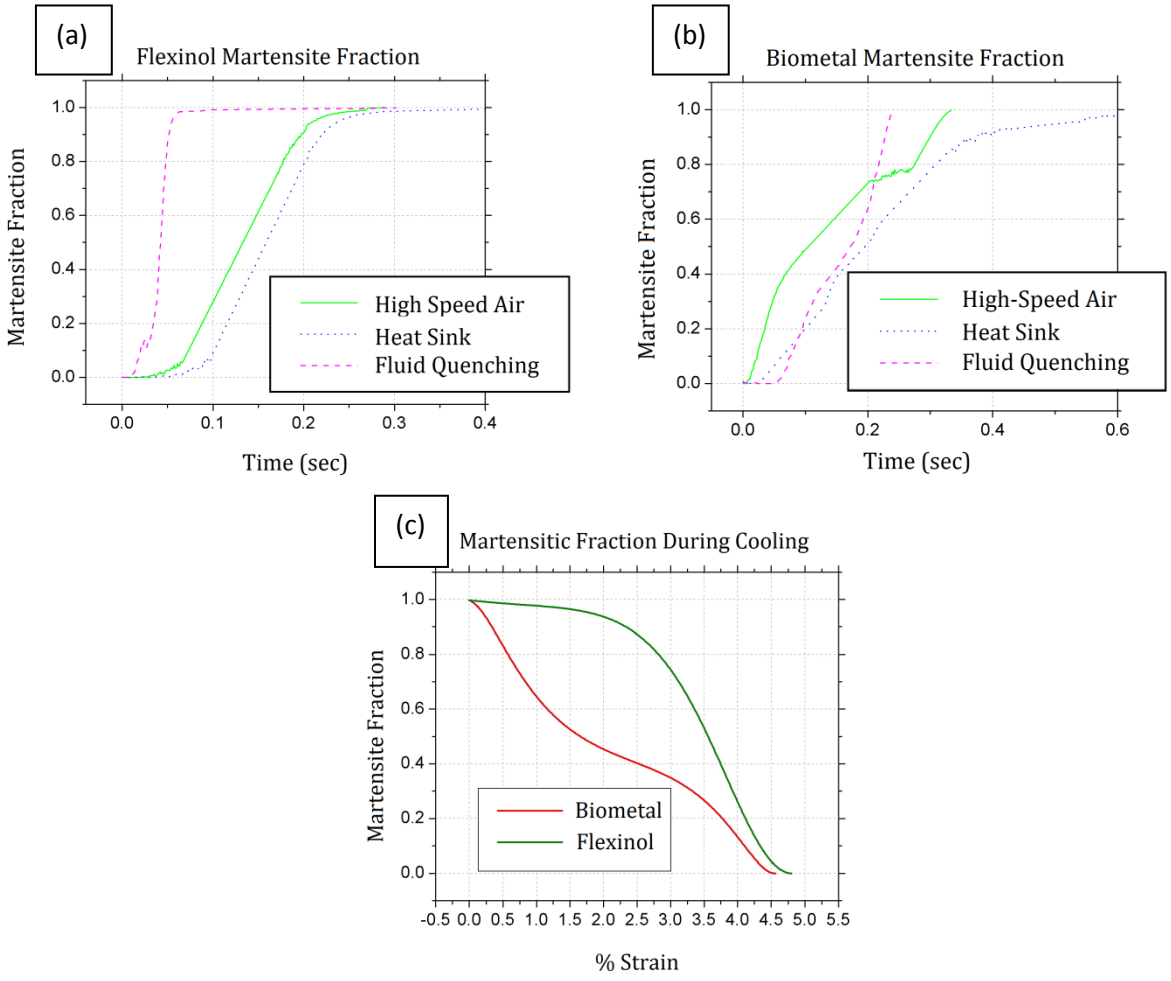

Figure 2.9: Fraction of martensite vs transition time behavior for (a) Flexinol and (b) Biometal fiber and (c) martensite fraction vs. strain curves for 0.005" diameter Flexinol and Biometal fiber.

2.2.8 Heat Transfer Analysis

It is interesting to compute the heat dissipation from SMA wire as a function of time. In order to use the lumped capacitance parameter model given by equation (2.1), it is important to satisfy the criterion used in its derivation. For a given characteristic length, $L_C = 2.54\,x10^{-5}$ (given by wire volume over surface area) and thermal conductivity of the wire, K = 18, the Biot number (Bi) must be less than 0.1. Substituting these parameters in Equation (2.1), the inequality

for heat transfer coefficient can be obtained as h < 70867 W/m^{2}K. Since this h value is much higher than that can be achieved in the experiment, the lumped capacitance model can be assumed to be valid. Using Equation (2.3), the heat transfer constant (h_o) was obtained by fitting the experimental data for temperature as a function of time for each active cooling method and the values are listed in table 2.2.

Table 2.2: Heat transfer coefficients for various active cooling method for Flexinol wire.

Cooling method	Constant heat transfer coefficient $h = h_0$ (W/m^{2}K)	Variable heat transfer coefficient ($h = h_0 + \beta T^2$)
Fluid quenching	2800	−0.3
High speed conv.	800	−0.1
Heat sink	650	−0.09
Low speed conv.	300	−0.04
Free	185	−0.02

In this calculation the magnitude of density was taken to be 6450 kg/m^3, heat capacity was taken to be 322 J/kg K, and the ambient temperature was taken as the martensite finish transformation temperature of 50^{o}C. To put it in perspective, a human hand has an average heat transfer coefficient of 6 W/m^{2}K and a steam turbine has an average heat transfer coefficient of 1200 W/m^{2}K. In literature [60, 56, 68] heat transfer coefficient for thermomechanical response of SMA is considered to be constant. For variable heat transfer coefficient which depends on environmental conditions and temperature of wire, a second order polynomial function can be used [45, 66] as given by equation (2.7):

$$h = h_O + \beta T^2, \qquad [2.7]$$

where h_0 is the constant value for heat transfer coefficient, β is the temperature coefficient and T is the temperature of the SMA wire. The magnitude of h shows a significant variation in the range of 185 – 2800 W/m^{2}K as shown in table 2.2. Figure 2.10 shows the measured temperature - time response and the fitted temperature profile by using different magnitudes of constant and variable heat transfer coefficients. As shown in each case, using a constant h value in equation (2.3) provides a temperature profile with reasonable accuracy. Variable heat transfer coefficients

lead to better estimates of the temperature profile mimicking the realistic condition. The coefficients of the heat transfer were also obtained by solving equations (2.2) and (2.7) in Simulink and Matlab and are compared with experimental values. It can be inferred from Figure 2.10 that values of the temperature coefficient are negative and small in magnitude. We can also see that variable heat transfer coefficient closely matches with experimental data.

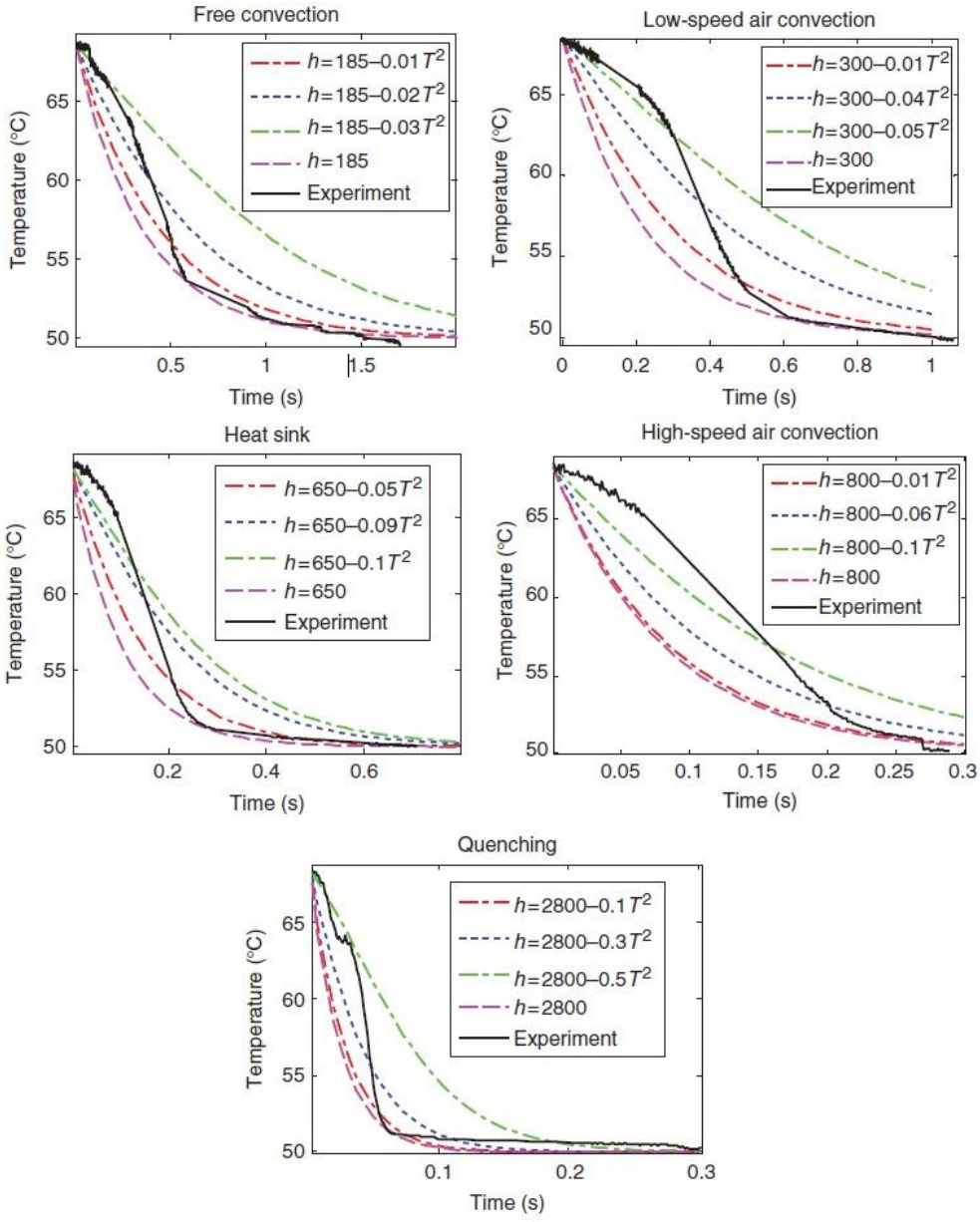

Figure 2.10: Constant and variable convective heat transfer coefficients for various active cooling techniques.

2.2.9 Cyclic Actuation

The cyclic actuation behavior of SMA wires for various active cooling methods was investigated because many systems require operation over extended periods of time. The SMA wires were subjected to square wave of 0.1 Hz for forced air and heat sink testing and a square wave of 0.05 Hz for fluid quenching test. The extra time between the contractions for fluid quenching test was necessary to remove excess water from the tube before the next contraction cycle. The results from these tests are shown in figure 2.11 (a) – (c). These graphs shows that the Flexinol wire maintains its strain characteristics over repeated actuation cycles while the Biometal fiber shows a downward trend in max strain especially in the forced air active cooling method. As the SMA wire is repeatedly contracted, some energy from the previous actuation is stored in the SMA wire, which causes shifts in the strain. There is a slight decrease in the magnitude of contraction but most of the effect was exhibited in the shifting of contraction. This result indicates that Flexinol wire would be better in repeated cycle application.

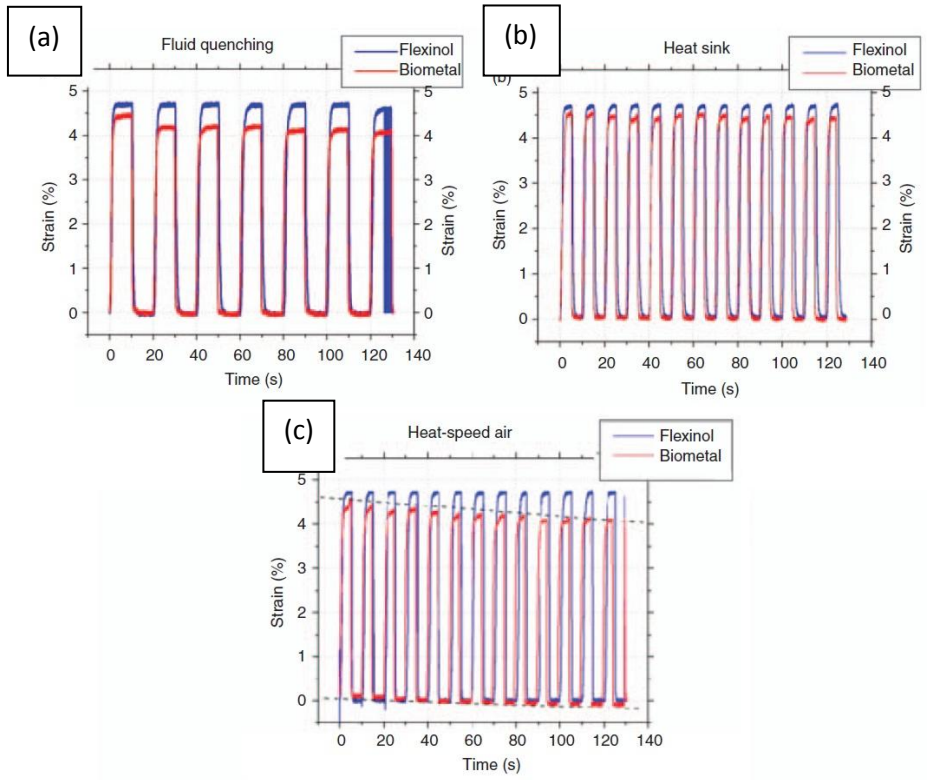

Figure 2.11: Thermal response of Biometal fiber and Flexinol under multiple heating/cooling cycles with (a) fluid quenching, (b) heat sink, and (c) high-speed forced air cooling.

2.3 Actuator Selection

So after characterizing the properties of SMA we conclude that a cooling mechanism can be implemented in order to decrease its thermal response time from ~2 to 0.3 seconds for SMA actuators with a diameter of 100μm. A potential solution can be shown below in figure 2.12.

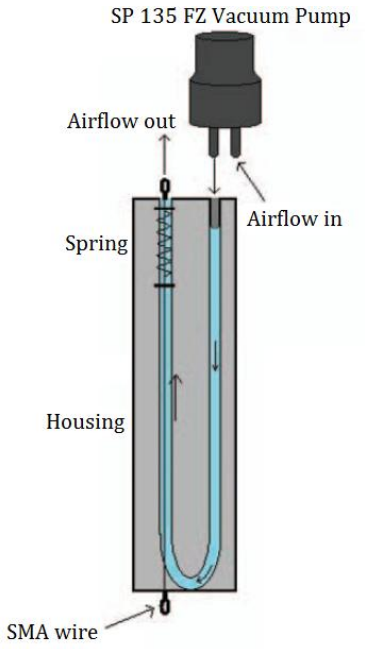

Figure 2.12: Potential SMA cooling mechanism utilizing airflow

This mechanism consists of a channel that allows airflow to pass over the SMA. The wire is rigidly attached at one end and a bias spring is at the other to provide return force during cooling. Airflow can be produced using a commercially available SP 135 FZ vacuum pump.

If we go back to our reason to investigate the use of SMA, we realize that its work density was one of its most attractive features. If we add a housing, spring and pump we are adding volume as well as more power consumption. These additions actually lower the energy density below levels of classic electromagnetic motors. Compound this with the difficulty of achieving precision control then SMA actuators are no longer the optimal solution for our robotic system.

Hitec-series servo motors are cost effective (usually less than $40 per motor) easily controlled and have a large support community for troubleshooting. They also have reasonable work densities (around 18 kJ/m^3) and low power consumption (between 1 and 5 Watts each) thus making them a sensible choice for our medical simulator. Figure 2.13 shows a comparison of weight to work capacity of many commonly used actuators as well as the HS-series servo motors chosen for our application.

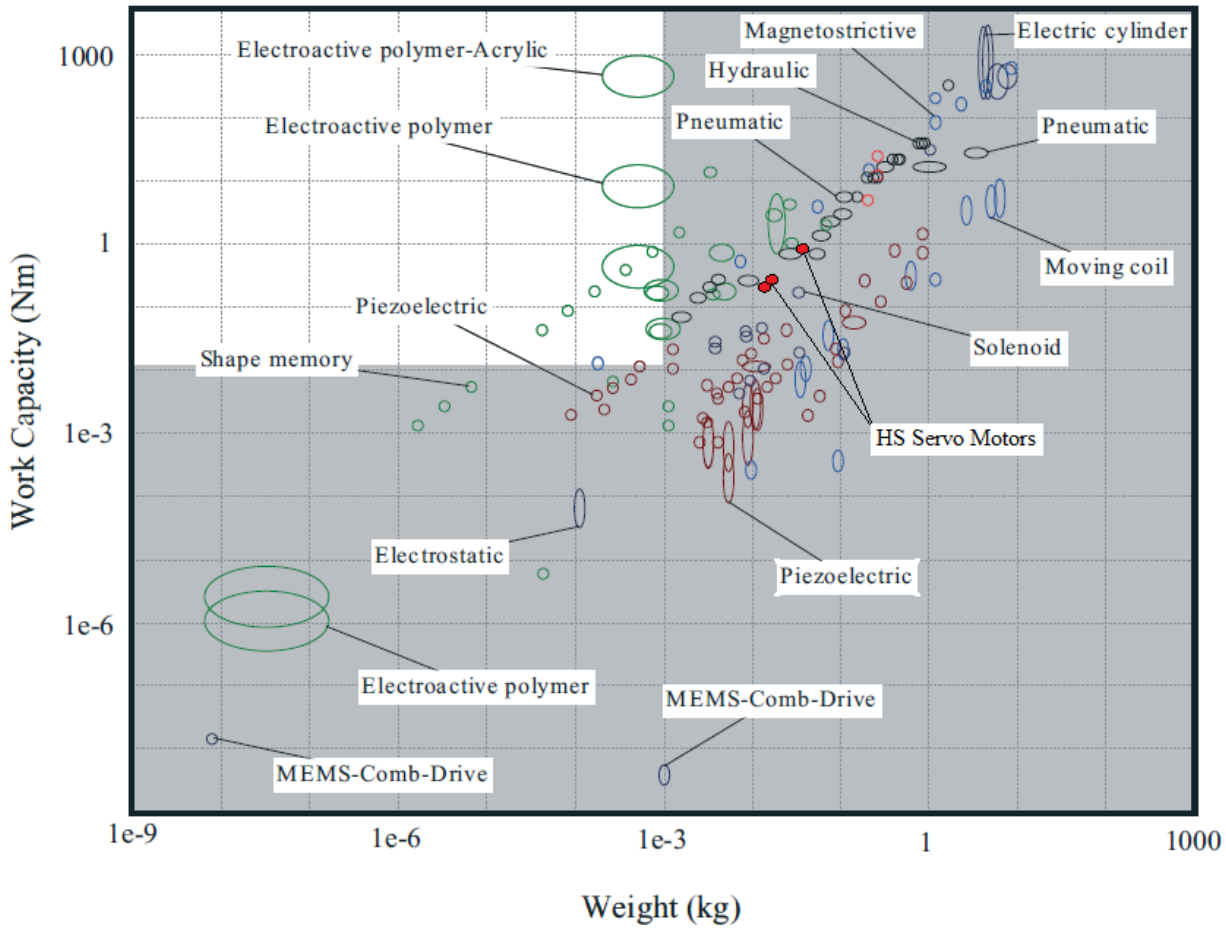

Figure 2.13: A plot of actuator work capacity versus mass including actuators chosen for the DART hand. Taken from: M. Zupan, M. F. Ashby and N. A. Fleck, Actuator Classification and Selection-The Development of a Database, Advanced Engineering Materials, 2002. 4. No. 12., pp 933-940. Copyright Wiley-VCH Verlag GmbH & Co. KGaA. Reproduced with permission.

2.4 Hand Design

2.4.1 Design Approach

The evolution of a body part is primarily based on the demands placed on it by the environment. Hooves, claws, fins and hands are examples of anatomical structures that provide mobility and surviving capability. A range of designs for these body parts can be found in nature, each showing the effect of species anatomy and the environment in which it survives. For example, primates often have five fingered hand similar to that of human but each species have optimized a different method for utilizing this appendage. Some species have developed tough skin above the knuckles in order to walk on all four limbs, while others have developed long slender fingers that assist with grasping tree branches. The human hand, with roughly 17,000 nerve endings [11], has evolved to take advantage of the precision grasp where fingertips are used in conjunction with the thumb to precisely manipulate objects. But as human society has evolved so has the demand placed on it by the environment. Human hands also communicate complex ideas and emotions on top of being highly dexterous. In 1834, Charles Bell [6] wrote: "and we must confess that it is in the human hand that we have the consummation of all perfection as an instrument." It is natural for a researcher to create a dexterous manipulator that mimics the human hand since its inherent capabilities can be observed in their own hand.

Slight changes in hand design from others such as fins or claws enables us to write, open doors, tie knots and perform many other activities of daily living (ADLs). Since the human hand is a naturally engineered biomechanical system it poses several design challenges in its replication, often leading to simplifications that degrade performance. A change in the architecture of an artificial hand from a human would result in different control schemes for performing ADLs and thus would no longer represent the functionality of a human hand. Therefore in trying to mimic functionality of the human hand it is important to mimic its musculoskeletal structure.

In several cases, human-like dexterity is not needed to accomplish a goal. For example – Prosimians (lemurs and lorises) possess only a single prehensile pattern; the hand opens and closes like the jaws of a toy crane in an amusement arcade [67]. Industrial robots are designed

for a specific job, exhibiting high dexterity in task-oriented pre-programmed applications in structured scenarios but exhibit low levels of anthropomorphism and manipulation capability [106]. However, in ADLs such as typing or opening doors, having many levels of dexterity becomes very important. In the past decades, due to a lack of high power density actuators suitable for prosthetics, mechatronic developers have basically focused on underactuated mechanisms design [16]. Some of the most advanced prosthetic devices utilize superficial electromyographic (EMG) signals to drive motors for grasping [71, 82, 104]. The trouble with using these signals is that it is hard to distinguish readings from different muscles that are physically near each other. Because of this, most prosthetics controlled by EMG signals have one or two actuators and a high degree of underactuation.

We started by investigating human hand physiology to gain an understanding of its musculoskeletal structure and how it contributes to overall functionality. Metrics commonly used to quantify various aspects of hand designs are size, weight, form, degrees of freedom, range of motion, grasp speed, and grasp force. Roughly 40 muscles are responsible for 23 degrees of freedom in the human hand and wrist, many existing to stabilize and connect biological tissue. Understanding which elements of the human hand are responsible for specific functions will help in eliminating unnecessary elements from the design therefore reducing redundancy and complexity.

2.3.2 Mechanical Design and Optimization

The human hand consists of a complicated set of muscles, bones, tendons, cartilage and ligaments that interact fluidly to produce efficient motion and high output forces. Figure 2.14 shows the bone structure and corresponding joint names for the human hand.

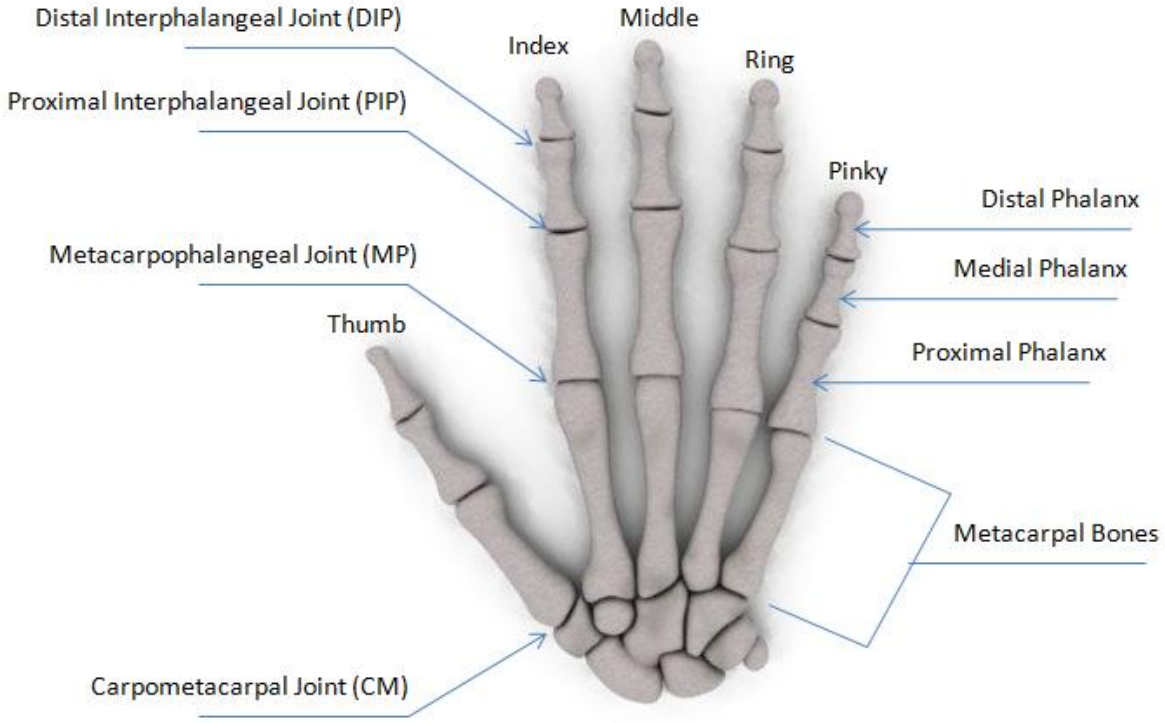

Figure 2.14: Skeletal nomenclature of the human hand.

The metacarpophalangeal (MP) joints are condylar joints which create two axes of motion, one more axis of motion than found in the DIP and PIP joints. The carpometacarpal (CM) joint of thumb is a saddle joint, similar to the condylar joint, but with greater range of motion and is responsible for thumb opposition. These joints are replicated in our dexterous, anthropomorphic, typing hand (DART) as universal joints which also create 2 axes of motion. The difference between artificial and biological joints is that a universal joint is rigidly locked in place at the intersection of the axes of rotation while human finger joints consist of concave and convex portions of cartilage that rest on each other and remain in place due to tension in passive and active tissue. The remaining joints in the human finger are hinge joints which allow motion about only one axis and are replicated in the DART hand as pin joints that behave similarly. The humanoid hand has 19 DOF broken down into 3 per finger, 4 for the thumb and 3 for the wrist.

The human finger represents a kinematic linkage system with nonorthogonal, nonintersecting axes of rotation at the CM and MP joints [13]. A system like this is difficult to

model because the axes of rotation in human fingers constantly change with respect to joint angle [106]. Modeling the IP joints as orthogonal joints with a fixed axis of rotation and MP joints as two orthogonal intersecting axes of rotations does not significantly change the system's kinematics. Plane joints between the carpal bones in the wrist are ignored and the wrist is modeled as three orthogonal intersecting axes of rotation.

Muscle groups assisting more than one degree of freedom in a single finger is a property of the human hand that improves grip strength and finger stability. Muscles like the flexor digitorum superficialis, which are primarily responsible for flexion of the proximal interphalangeal (PIP) joint, flex the DIP joint as well as the MP joint at some level of contraction. By excluding this feature from the DART hand, grip strength, stability and system complexity will decrease but not to a point where the hand is unable to perform all necessary ADLs.

Independent control of each finger is also a feature of DART hand that greatly reduces complexity. Muscles such as the flexor digitorum profundus, which are responsible for flexion of the distal interphalangeal (DIP) joint, are sometimes connected at the tendons and function to move joints in more than one finger (noticeable when one tries to flex the fingertips of the ring and pinky finger independently). Removing this constraint increases uniformity of the hand and reduces complexity in fabrication and control without sacrificing functionality.

An underactuated system has more DOF than DOM. Many underactuated robotic hands have been developed [9, 74, 80, 103], some utilizing 4-bar mechanisms while others use differential mechanisms to passively grasp objects. The TUAT/Karlsruhe hand [29] uses a single actuator to drive a multi-fingered differential hand for passive grasp shaping. DART hand uses a modified version of the underactuated 4-bar mechanism of the TUAT/Karlsruhe hand to couple the DIP and PIP joints. The design benefits of a 4-bar mechanism include rigid joint connections and the removal of an actuator per finger. This mechanism permits 70^{o} rotation for the DIP joint and 90^{o} for the PIP joint whereas human finger can achieve 70 and 110 degrees respectively. Since thumb dexterity is important in fine manipulation tasks it does not incorporate this 4-bar mechanism thus leaving independent control of each joint. A universal joint connects the thumb to the palm and allows the thumb to touch each fingertip as well as the opposing end of the palm.

Human hands have separate muscles for flexion and extension. Sometimes both sets of muscles actuate to help with stability but as mentioned before this function has been removed from the DART hand. Torsional springs placed at the joints eliminate the need for extensor muscles thus removing the need for these motors. Figure 2.15 (a) shows the CAD model of the finger mechanism built using Unigraphics 6.0. The MP adduction/abduction joint axis is perpendicular to the joint axis for flexion/extension (not shown in figure 2.15 (a). A rectangular block fits between the palm and proximal phalanx and is held together with pins which create a universal joint. An important feature is the tunnel that routs the wires from the dorsal (palm) to ventral (back) side of the hand. As the IP joints are flexed, extensor muscles are activated to keep other joints from also flexing. Since there are no extensor motors in the artificial hand the force experienced from IP joint flexion would overcome the holding force of the torsional springs and cause the MP joint to co-flex. Some designs take advantage of this feature to create a shape-forming grasping mechanism as mentioned earlier. To remedy this, IP joint wires are routed to the ventral (back) side of the finger to stabilize the flexion motion against the wire responsible for MP joint flexion much like opposing stabilizing cables on a radio tower.

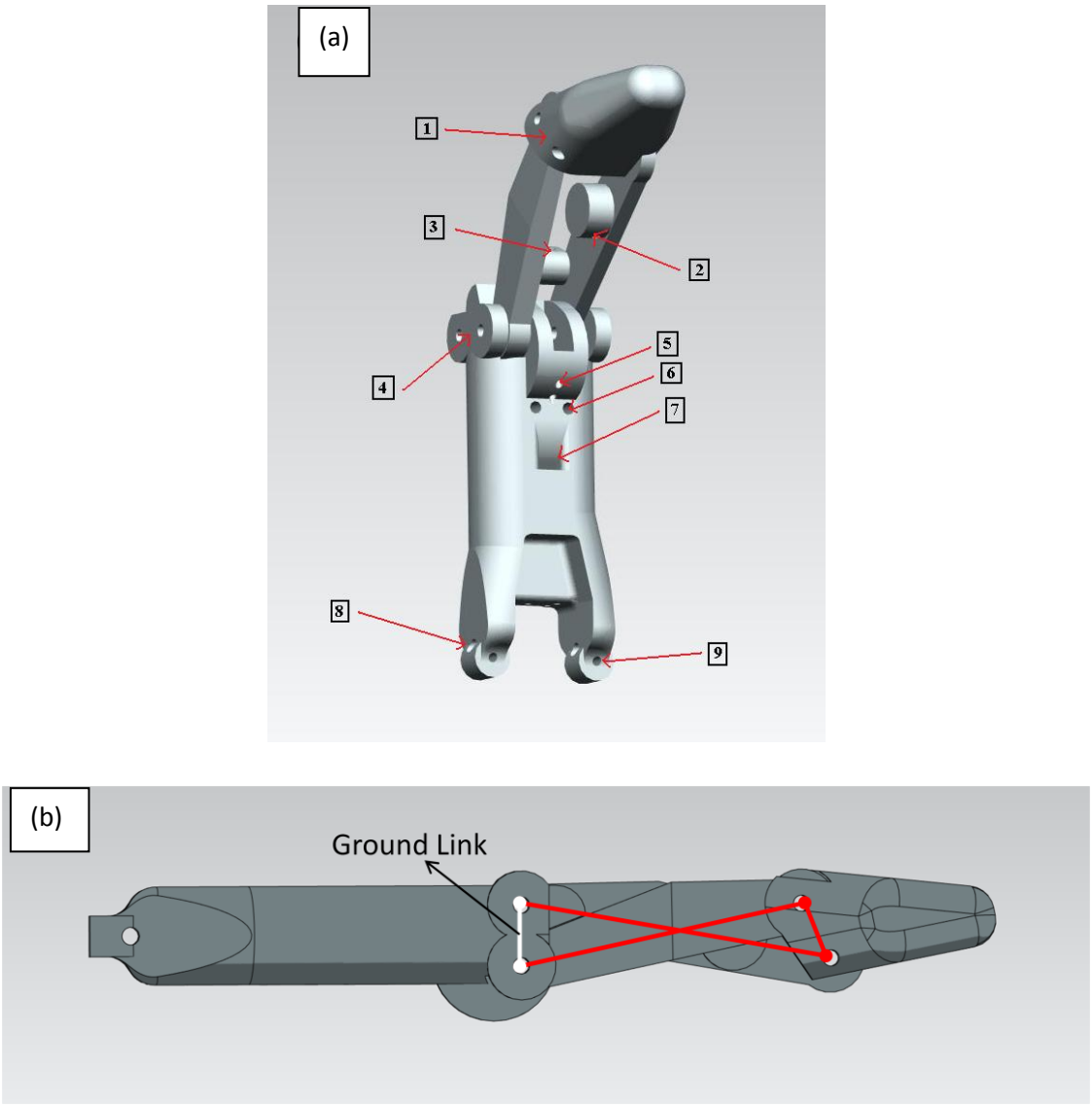

Figure 2.15: (a) Structure and functional elements of a finger of the DART hand. Arrows in this figure point important design features as: 1. DIP joint axis, 2. Insertion point for IP joint motion, 3. Attachment point for torsional spring on middle phalanx, 4. PIP joint axis, 5. Attachment point for torsional spring on proximal phalanx, 5. Insertion point for flexion/extension MP joint motion, 6. Tunnel to rout wires from dorsal (palm) to ventral (back) side of hand, 7. MP joint axis for flexion/extension, 8. Insertion point for adduction/abduction MP joint motion, (b) 4-bar mechanism created by the medial phalanx links.

In order to maintain human-like function and range of motion, kinematics of the 4-bar mechanism linking the DIP and PIP joints should mimic those of a human. A 4-bar mechanism

can produce trajectories through various link lengths and pin locations. Figure 2.15 (b) shows the finger link mechanism. To reach this configuration, the positions of pin joints and link lengths were varied until the trajectory of fingertip during flexion remains within 3mm of a human fingertip trajectory at all times. The multi-body dynamic simulation program, ADAMS, was used to simulate and measure the trajectory of the robot's fingertip as shown in figure 2.16 (a). To compare trajectories of the robot to a human, position data from a participant's finger was collected with a high speed camera. A program developed using MATLAB tracks and plots reflective points at the fingertip and IP joints on the participant's finger as it flexes as shown in figure 2.16 (b). A comparison between human and robot is shown in figure 2.16 (c) that reveals the trajectory is within 3 mm of human finger at all times and the difference at the end of the trajectory is 1.5 mm.

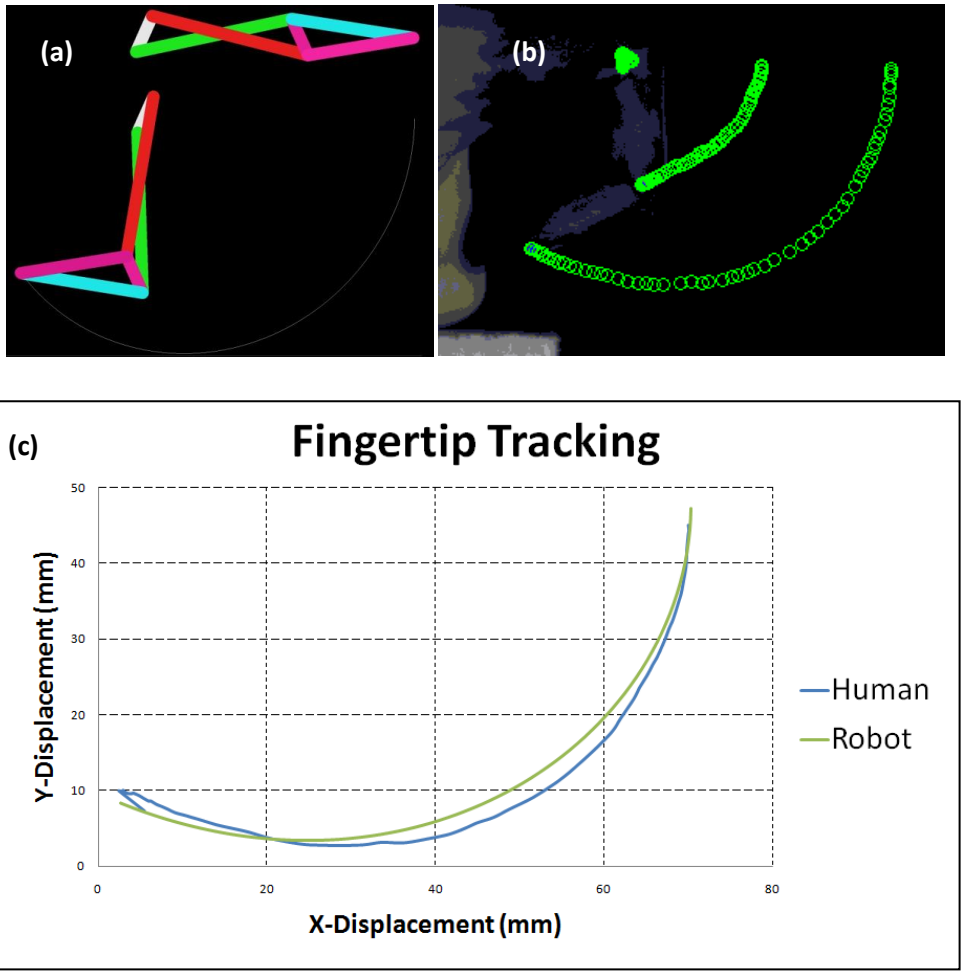

Figure 2.16: (a) Fingertip trajectory analysis carried out with ADAMS, (b) Tracking reflective points on a human finger with a high-speed camera and MATLAB, and (c) Fingertip trajectory

comparison between human participant and the robot. The robot maintained a maximum offset of 3mm from the human finger at all times.

It is known that an average peak force of 2 N is experienced while typing [46]. Unlike other nonprehensile skills like piano playing, striking a key with more force does not affect the input to a computer. During typing, force is a rather loosely controlled variable that is programmed simply to exceed the activation force of the key [46]. Figure 2.17 shows the experimental results for fingertip force normalized to the maximum output of the actuators versus joint angle for the given finger geometry.

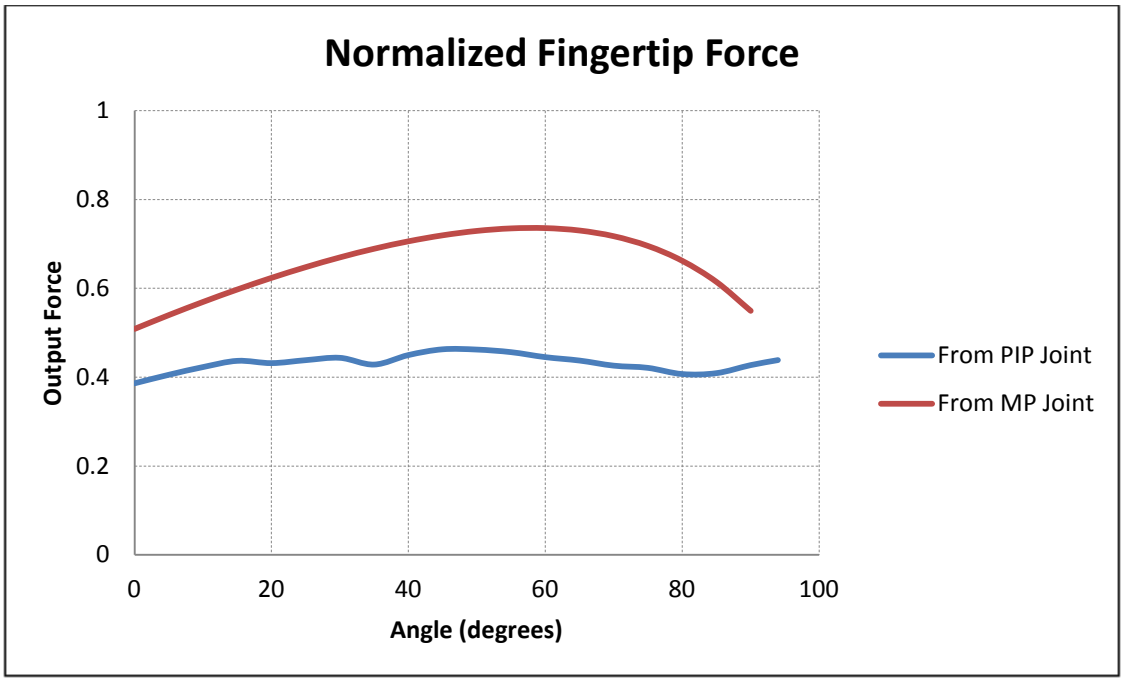

Figure 2.17: Percentage of maximum motor output experienced at the fingertip. PIP joint rotation produces less force at the fingertip and is therefore the limiting value for maximum fingertip force.

Flexion of the PIP joint is accomplished with the HS-85MG servo motors with a maximum output torque of 34.6 N-cm. The moment arm from the motor horn was 1.1 cm which creates a maximum linear force of 31.5 N leading to a maximum fingertip force of 12.1 – 14.4 N. The HS-225BB motor was used to flex the MP joint and provide a maximum fingertip force of 12 N to 17.3 N. Since the PIP joint is the limiting factor, a maximum fingertip force range of 12.1 N to 14.4 N was achievable without stalling the HS-85 motors.

The MP joints (or knuckles) of the artificial hand were offset from each other at average distances and angles as depicted in [3]. Other dimensions like finger length, palm size, finger spacing and forearm size were also optimized to be within the statistical average. Keeping dimensions of the artificial hand similar to that of an average person is important, especially for keyboard typing since slight deviations in dimensions will affect the user's ability to utilize a keyboard. For example, if the palm is proportionally larger to the fingers the wrist will have to compensate for this length by extending until the resting position of the fingers reaches the center row keys. The shoulder and elbow can also be used to move the position of the entire hand with respect to the keyboard to compensate for this disproportion but will add unnecessary complexity and cost.

Finger flexion, abduction and adduction are provided by high tensile strength wires that originate from servo motors in the forearm as shown in figure 2.18 (a) and run to insertion points on the fingers. This replicates the natural function of extrinsic muscles in the human forearm. The forearm is composed of four modules that houses the motors and provides a support structure. Two motors are placed near the hand to control the wrist and every succeeding module houses motors to actuate the fingers and thumb. Smaller motors are placed closer to the hand to reduce the moment arm for a future elbow mechanism. Between the last two modules is the Lynxmotion SSC-32 servo motor controller that is used to distribute pulse commands and amplify signals to the motors. At the end of forearm is a cover that houses a motor and gearbox for rotation of the entire forearm mimicking the ulna and radius crossover in a natural human arm as shown in figure 2.18 (b). A holding bolt runs through a central gear, cover plate, and thrust bearings attaching to a stationary elbow assembly. This mechanism allows 110^{o} of rotation while a human is able rotate their forearm roughly 150^{o}. Pictures of the fabricated DART hand are compared with the human hand in figure 2.18 (c) and (d). DART hand has been designed slightly smaller than average to account for silicone skin that will cover the entire skeletal structure of the hand and upper forearm as shown in figure 2.18 (e). The skin helps with gripping friction and also increases the resemblance to human hand. Future improvements to the design will include a similar skin with embedded piezoelectric sensors to assist with tactile sensing.

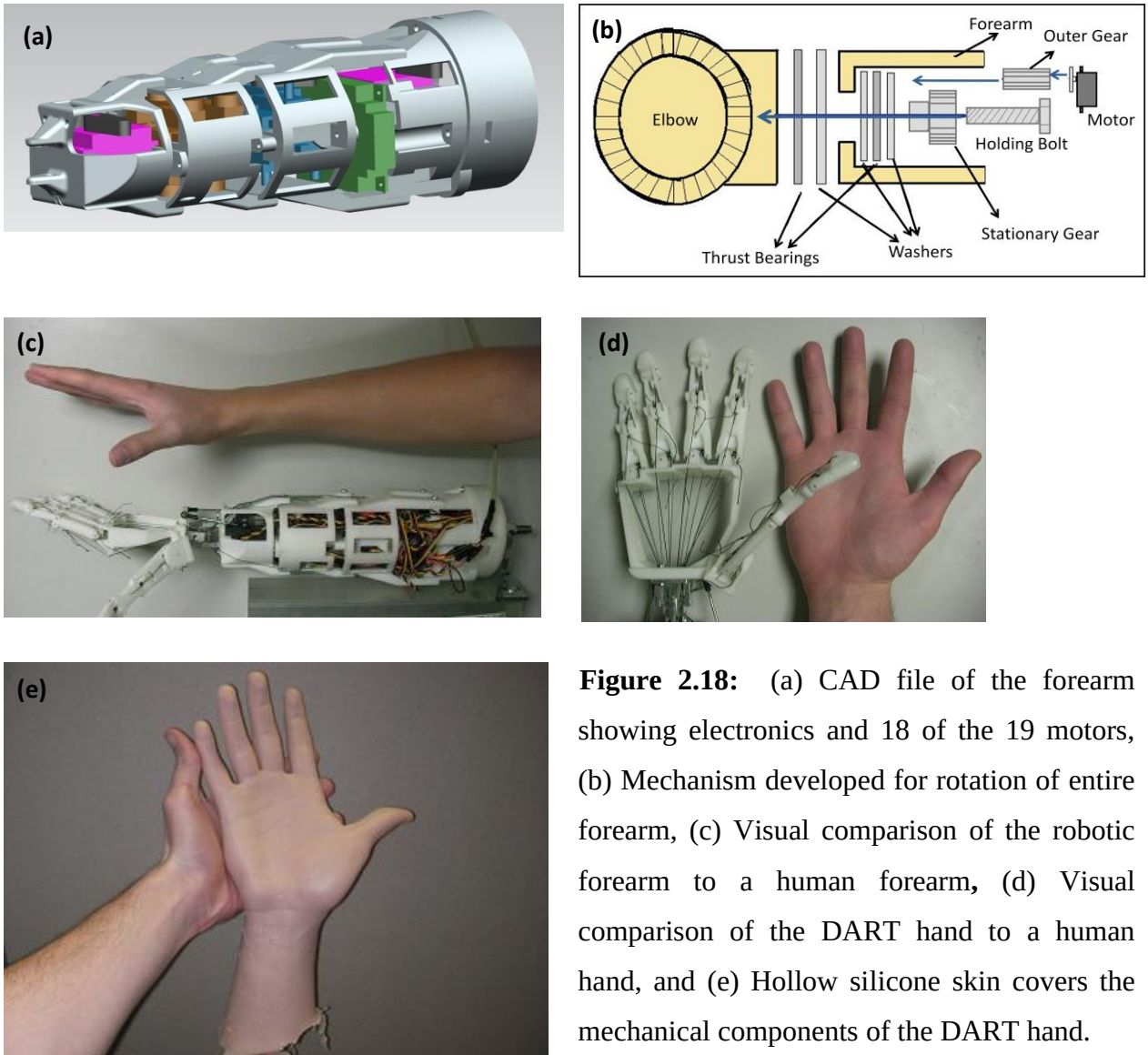

Figure 2.18: (a) CAD file of the forearm showing electronics and 18 of the 19 motors, (b) Mechanism developed for rotation of entire forearm, (c) Visual comparison of the robotic forearm to a human forearm**,** (d) Visual comparison of the DART hand to a human hand, and (e) Hollow silicone skin covers the mechanical components of the DART hand.

The tendons that travel in a human hand pass through the carpal tunnel which acts as a protective sheath and keeps them from separating from the wrist like a string on a bow. Tendons that actuate the human wrist originate in the forearm and insert on the carpal bones to flex and extend the hand. The humanoid wrist utilizes a differential mechanism that combines inputs from two servo motors to rotate about two axes. Instead of using wires which are only capable of pulling, the humanoid wrist uses two rigid rods to push and pull creating a combined moment about the wrist. To flex or extend, both motors move forward or backward and to adduct or abduct the motors move opposite to each other. The carpal tunnel was recreated with a universal

joint that allows the wires in the fingers to pass through it. A picture of the fabricated wrist mechanism is shown in figure 2.19 (a).

In the human wrist, tendons run from muscles in the forearm through the carpal tunnel to their insertion points in the hand. When the wrist rotates some tendons experience tension while others gain slack. Natural elasticity in the human body reduces some of these effects and the brain compensates for any additional forces by contracting other muscles. However, in a robotic system that is rigid, any extra slack or tension will cause unwanted forces that are difficult to be compensated in real time. Without developing a force-feedback system, these effects can be eliminated by routing the tendons or wires through the axes of rotation in the wrist. In a one DOF wrist, wires can be routed along the axis of rotation without experiencing tension. Figure 2.19 (b) shows that if a second DOF is added then the wires must be routed about both axes of rotation (a single point) to avoid unwanted forces. It is difficult to achieve this in practice since there are over 20 wires each with a diameter of 0.5mm. The solution in our design was to rout the wires as close to the center of rotation as possible to help eliminate these effects. Figure 2.19 (c) shows a close up view of the artificial carpal tunnel. The acrylic ring serves to guide wires as well as connect the palm to forearm by acting as the center of the universal joint. The forearm creates 6 separate entrance locations to the carpal tunnel which reduces friction between the wires.

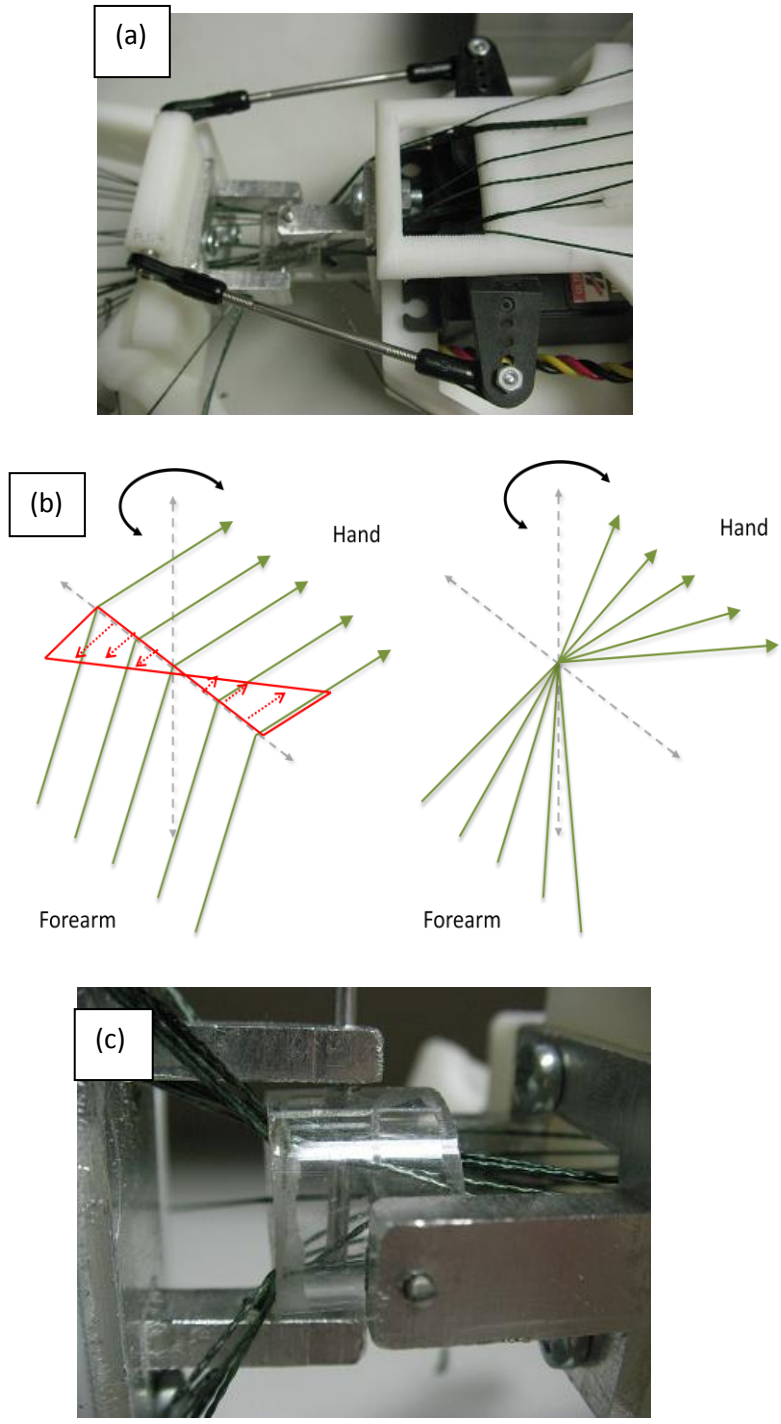

Figure 2.19: (a) Wrist mechanism utilizing two servo motors and a differential system that rotates about a universal joint, (b) Tension forms in wires that are not routed about each axis of rotation. The green arrows represent wires and the red arrows represent tension profiles, and (c) Artificial carpal tunnel which guides wires to the hand.

2.3.3 Kinematics and Control

Our benchmark for success in designing a dexterous hand is to optimize the performance while using a keyboard since typing and piano playing are often considered to be among the more complex forms of skilled serial action performed by human beings [46]. Several systems reported in literature have deployed complex control strategies. The DRL-HIT-Hand [58] utilizes 12 sensors per finger including joint torque and position, motor position, fingertip force and temperature. This hand has demonstrated playing music, autonomously grasping a bottle and tele-operation. A piano playing robot, developed by Huh et al. [40], utilizes 21 degrees of freedom and an inverse kinematic approach to play music. Edin et al. [22] have used on-off contact sensors as well as a custom-made triaxial force sensor based on strain gauges to compare the different dynamic stages of hand while lifting objects. Various other robotic grippers have been developed that perform grasping, lifting and certain dexterous tasks, but to our knowledge there are currently no robotic hands capable of accurately typing on a keyboard at human speed. In this study, we utilize a closed-loop control strategy based on motor and joint position as well as fingertip pressure. The next iteration of our artificial hand will include tension sensors on the wires for redundancy in force-feedback control.

Figure 2.20 (a) shows a flow diagram of control strategy. Input text can come from a voice recognition program or through a keyboard. The word(s) to be typed are separated by character and assigned to finger using standard keyboard finger placements. Motor commands are then sent to motors to hover above the desired key before pressing. After the key is pressed, MATLAB checks to see if this was the desired key. If the pressed key was not the desired key then the hand will hit the delete button, adjust itself accordingly and try again. If the pressed key was the desired key, the program checks to see if it is the last character in the array. If it is the last character then the program ends; if not, then the next desired key is loaded and the cycle starts again.

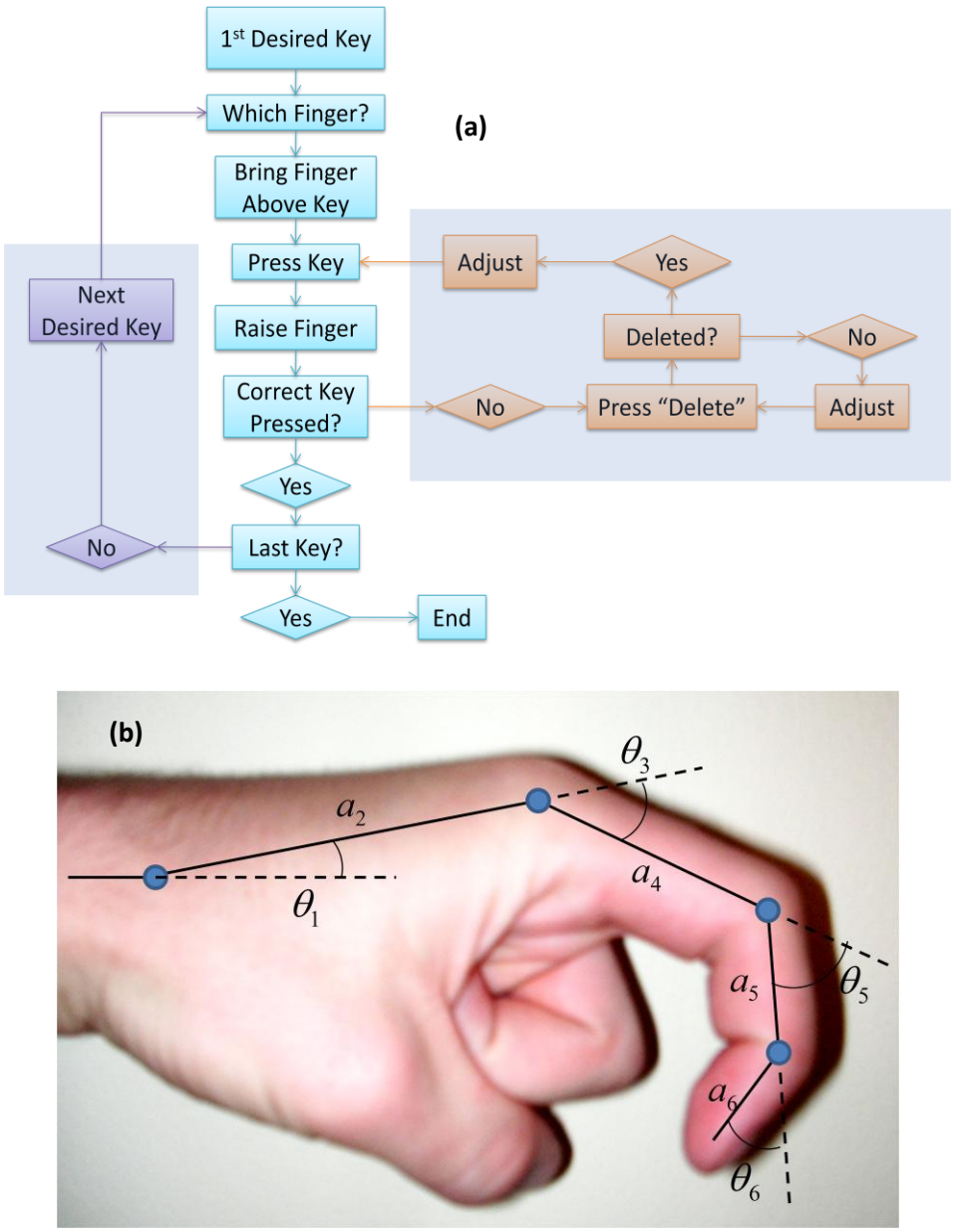

Figure 2.20: (a) Control strategy flow diagram, and (b) DH link and angle labels.

The Denavit-Hartenberg method was used to develop a spatial relationship between each joint. Since joints in the DART hand have a stationary axis of rotation, unlike the human hand, this method is suitable for creating a kinematic model. The D-H method is very attractive in robotics because it makes complex positional calculations of multi-link systems simple by arranging them into a set rotational and translational matrices [86]. If one were to imagine their right hand on a keyboard, ready to type, the global reference frame would be located at the center of rotation of the wrist. The x-axis points toward the left hand, the y-axis points away from the

keyboard and the z-axis points toward the screen. The matrices below represent rotation about the z and x-axis, respectively.

$$\begin{bmatrix} \cos(\theta) & -\sin(\theta) & 0 & 0 \\ \sin(\theta) & \cos(\theta) & 0 & 0 \\ 0 & 0 & 1 & 0 \\ 0 & 0 & 0 & 1 \end{bmatrix} \quad \begin{bmatrix} 1 & 0 & 0 & 0 \\ 0 & \cos(\alpha) & -\sin(\alpha) & 0 \\ 0 & \sin(\alpha) & \cos(\alpha) & 0 \\ 0 & 0 & 0 & 1 \end{bmatrix}$$

In order to find the end effector position in a linkage system where the reference frame rotates about the z-axis then the x-axis, the two matrices above have to be multiplied. The last column of the product then gives equations for the x, y and z position (top to bottom) of the end effector with respect to the global axis. In the DART hand, there are 7 joints which means 7 rotational matrices need to be multiplied together which produces a 4x4 matrix with large equations for x, y and z position. Further details on the D-H method and its derivation can be found in the Ref. [86]. Link parameters for D-H convention are provided in table 2.3 and the schematic in figure 2.20 (b) is labeled accordingly. The notation θ_0 corresponds to rotation of the wrist, θ_2 to wrist abduction/adduction and θ_4 corresponds to MP joint abduction/adduction and cannot be shown in figure 2.20 since they rotate in a plane perpendicular to the figure.

Table 2.3: D-H link parameters for wrist to fingertip

Link	a	α	d	θ
0	0	-90	0	θ_0
1	0	-90	0	θ_1
2	a_2	90	0	θ_2
3	0	-90	0	θ_3
4	a_4	90	0	θ_4
5	a_5	0	0	θ_5
6	a_6	0	0	θ_6

Since key position is the desired location of the fingertip, an inverse kinematic analysis was performed to determine joint angles in the kinematic chain from wrist to fingertip. An issue commonly encountered while modeling complex biological systems is under constraining which leads to an infinite combination of joint angles that create the desired output and requires additional constraining equations to solve each joint angle. There are 6 degrees of freedom

between the wrist and fingertip. Since the IP joints are coupled with a 4-bar mechanism, five of the joint angles need to be solved leaving one joint which can be geometrically calculated. The IP joint angles and fingertip trajectory of the DART hand can be accurately represented (R value greater than 0.98) with the following relationship [16, 24, 57]:

$$\theta_{DIP} = \left(2/3\right)\theta_{PIP} \tag{2.8}$$

$$\theta_6 = \left(2/3\right)\theta_5 \tag{2.9}$$

This simple relationship was derived to simplify kinematic calculations which helped in decreasing the simulation time in MATLAB.

Breaking down the number of possible wrist positions into a finite number of set positions solves for θ_1 and θ_2. The third degree of freedom, θ_0, was determined, through observation, to be 15 degrees. The hand and forearm were properly positioned before typing in order to establish a static global reference frame with respect to the keyboard. To do this, the locations of the keys with respect to the wrist had to be mapped out beforehand. Figure 2.21 shows different keys that can be pressed while the wrist flexes, extends, adducts and abducts. Keys colored light grey in this figure can be pressed while the wrist is in neutral position. Keys colored grey can be pressed while the wrist adducts and abducts and keys colored black can be pressed while the wrist flexes and extends from neutral position. Some of the keys are colored twice which means the wrist must rotate about two axes to reach them.

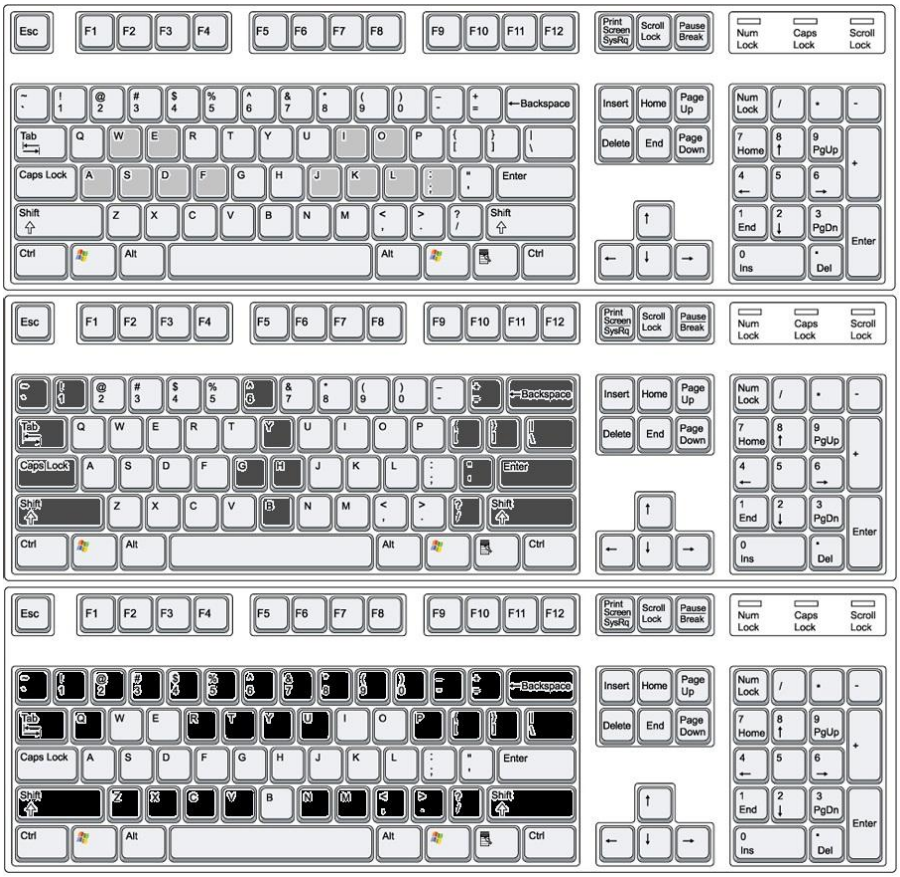

Figure 2.21: Key that can be pressed in different wrist positions. Light grey – neutral wrist position, grey – abducted/adducted wrist position, black – flexed/extended wrist position.

The degree of freedom in the MP joint (knuckle) responsible for adduction/abduction, θ_4, was solved next. Figures 2.22(a) and (b) show that orientation of the palm and finger affects the trajectory of the fingertip on the keyboard. If the plane of the palm was parallel with the plane of the keyboard, the geometry would be simple. But since θ_0 exists, the "X" location of the key must be adjusted.

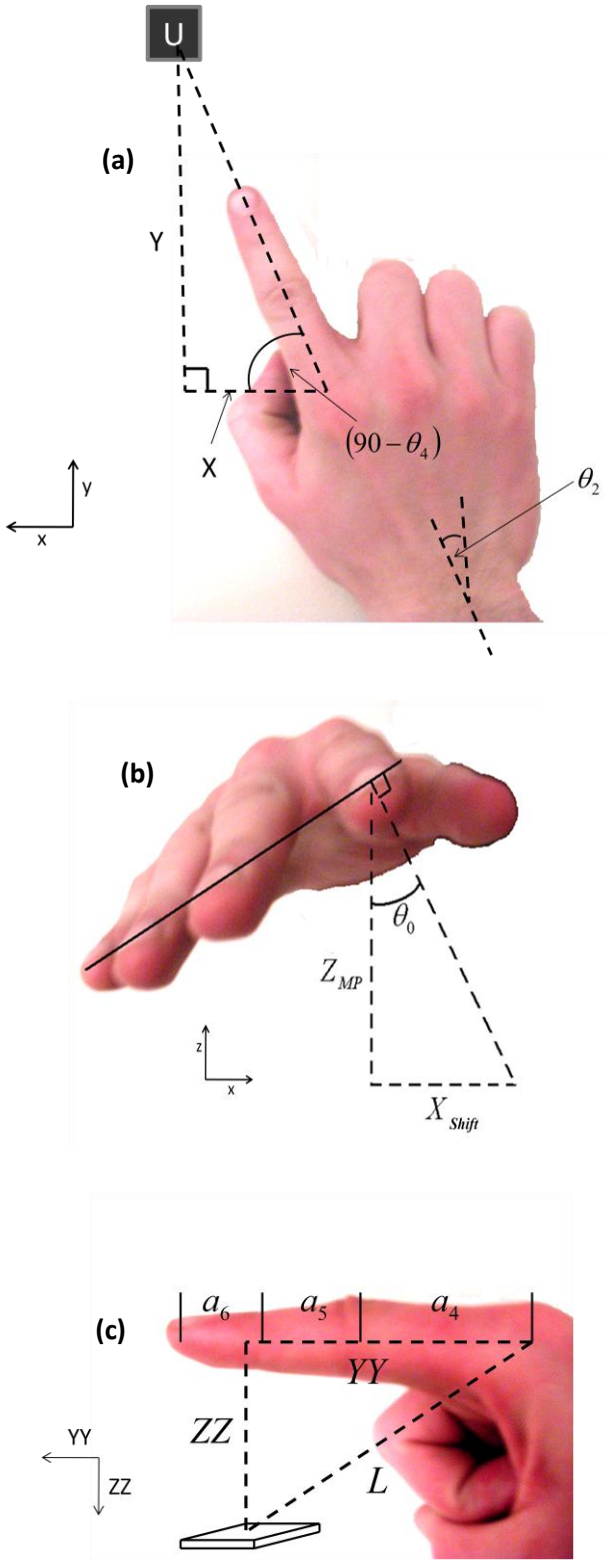

Figure 2.22: (a) X-Y plane view of a hand in the global reference frame, (b) X-Z plane view of a hand in the global reference frame, and (c) YY-ZZ plane view in the "new" coordinate system.

Equation (2.10) was developed using simple trigonometric relationships to solve for adduction/abduction (θ_4).

$$\theta_4 = 90 - \tan^{-1}\left(\frac{Y}{X - X_{shift}}\right) \tag{2.10}$$

$$X_{shift} = Z_{MP}\tan\theta_0 \tag{2.11}$$

This process determines a suitable θ_4 that lines up the finger with the desired key in X-Y plane and enables a two-dimensional analysis of the remaining degrees of freedom in a new reference frame (YY-ZZ). In this new two-dimensional coordinate system, YY represents the axial location of the key with respect to the finger and ZZ represents the distance between the MP joint and the key perpendicular to the YY axis as shown in figure 2.22(c). The minimum distance, L, between the MP joint (knuckle) and desired key can be found because the locations of the knuckle and key with respect to the wrist are known in the global reference frame (X-Y-Z). The relevant expressions are given below:

$$L = \sqrt{\left(X_{MP} - X_{KEY}\right)^2 + \left(Y_{MP} - Y_{KEY}\right)^2 + \left(Z_{MP} - Z_{KEY}\right)^2} \tag{2.12}$$

$$X_{MP} = \mathrm{a}_2\cos(\theta_0)\sin(\theta_2) - \mathrm{a}_2\cos(\theta_2)\sin(\theta_0)\sin(\theta_1) \tag{2.13}$$

$$Y_{MP} = \mathrm{a}_2\sin(\theta_0)\sin(\theta_2) + \mathrm{a}_2\cos(\theta_0)\cos(\theta_2)\sin(\theta_1) \tag{2.14}$$

$$Z_{MP} = \mathrm{a}_2\cos(\theta_1)\cos(\theta_2) \tag{2.15}$$

Now as we try to solve for YY and ZZ components of the finger length in the new coordinate system two equations can be formulated using simple geometry.

$$L_{YY} = a_4\cos(\theta_3) + a_5\cos(\theta_5) + a_6\cos((2/3)\theta_5) \tag{2.16}$$

$$L_{ZZ} = a_4\sin(\theta_3) + a_5\sin(\theta_5) + a_6\sin((2/3)\theta_5) \tag{2.17}$$

Pythagorean's theorem can now be used to set these two equations equal to *L*.

$$L = \sqrt{{L_{YY}}^2 + {L_{ZZ}}^2} \tag{2.18}$$

θ_3 and θ_5 are then solved, since there is only one combination of these angles that will reach the desired key position.

2.3.4 Results and Discussion

It is important to quantitatively compare the design similarity of the DART hand to human and other robotic hands. Factors included in comparison include weight (with actuators), number of fingers (including thumb), DOF per finger and wrist, number of sensor types and fingertip force. DOF per finger means adding every DOF, including the thumb, and dividing by the number of fingers. The wrist is included in this calculation because it considerably amplifies the manipulation capabilities of the hand and is essential to many of the hand's useful actions. The equation used is shown below:

$$\left(\frac{\#of\ \ fingers}{5}\right)\left(\frac{(DOF/\ finger)+(DOF/wrist)}{7}\right)\left(\frac{\#of\ sensor types}{6}\right)\left(\frac{fingertip\ \ force}{50.9\,N}\right)\left(\frac{15\,N}{weight}\right) \tag{2.19}$$

The numbers used for the human hand come from several sources. Clauser et al. [15] reported that the mean mass of male right hand is ~0.4 kg and the forearm mass is 1.13 kg leading to a combined mass of 1.53 kg which is 15 N. Astin [4] has reported the mean strength of the index finger to be 50.9 N. Human hands have six different types of sensors: tactile, pressure, temperature, muscle force, muscle position and joint position [46]. Figure 2.23 shows the comparative analysis using equation (2.19) for various hands reported in literature and table 2.4 lists the parameters for these hands. This graph does not entirely convey anthropomorphism since it is possible to exceed human performance in sensor types, and fingertip force or weight.

Thus, it is more a quantification of functional potential since as the numerical value increases so does the number of actions that can be successfully performed by the hand. Two different scores are shown for each hand: with and without a 3 DOF wrist. This is done to show how the wrist affects numerical scores since most robotic hands in literature do not feature a wrist or forearm mechanism. Figure 2.23 shows that DART hand has exceptional functional potential compared to other artificial hands. Including more sensor types would be the best area of improvement to increase the performance of the DART hand.

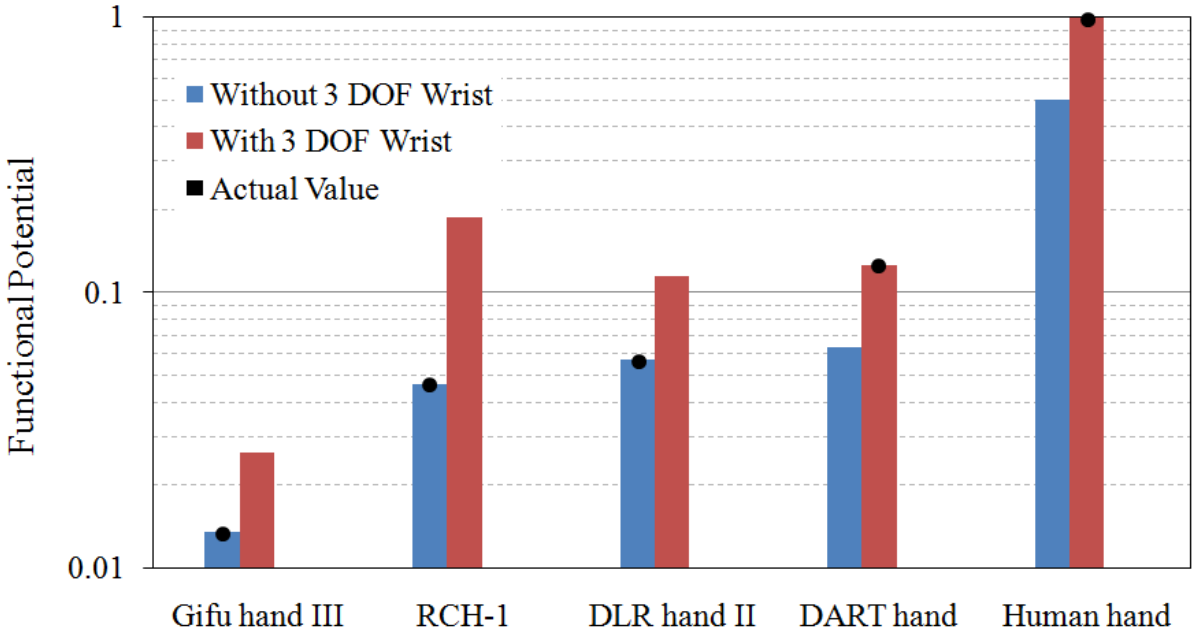

Figure 2.23: Functional potential comparison of the DART hand and other hands reported in literature to the human hand. Black dots represent actual values of the full mechanical systems reported in literature.

Table 2.4: Parameter list of robotic hands reported in literature.

Name	# of Fingers	Wrist DOF	Finger DOF	Weight	Fingertip Force	Sensors
DLR hand II	4	N/A	3	1800 g	10 N	Joint/motor position, joint/fingertip torque, temperature, accelerometers
Gifu hand III	4	N/A	3.25	1400 g	3.4 N	Tactile, motor/joint position
RCH-1	5	N/A	1	920 g	15 N	fingertip force, tactile, joint/motor position
DART hand	4	3	3	1530 g	14.4 N	Joint/motor position, fingertip force

The human body is a closed-loop proprioceptive system that is affluent to recognizing and responding to disturbances. Open-loop control is a suitable approach in robotics as long as the task does not require any reaction to external stimuli and the system is resistant to disturbances or creep. For example, if the artificial hand receives an overzealous high-five, wires could stretch and cause position errors if no sensors are in place to tell it otherwise. Even over time the wires may lose some of their tension and cause similar errors. For these reasons it is important to have sensors in place that keep track of joint position. Analog Hall-effect sensors (part number 785-SS496A from Mouser Electronics) were chosen for this purpose due to their small size and ease of mounting. The sensors were mounted in the 4-bar linkage between the PIP and DIP joints shown in figure 2.24 (a). An example signal from the PIP joint Hall sensor during 90^{o} of travel is also shown in figure 2.24 (a). The signal peaks ranged from 804 mV to 816 mV for the PIP joint while the signal ranged from 812 to 816 mV for the DIP joint due to the difference in mounting orientations.

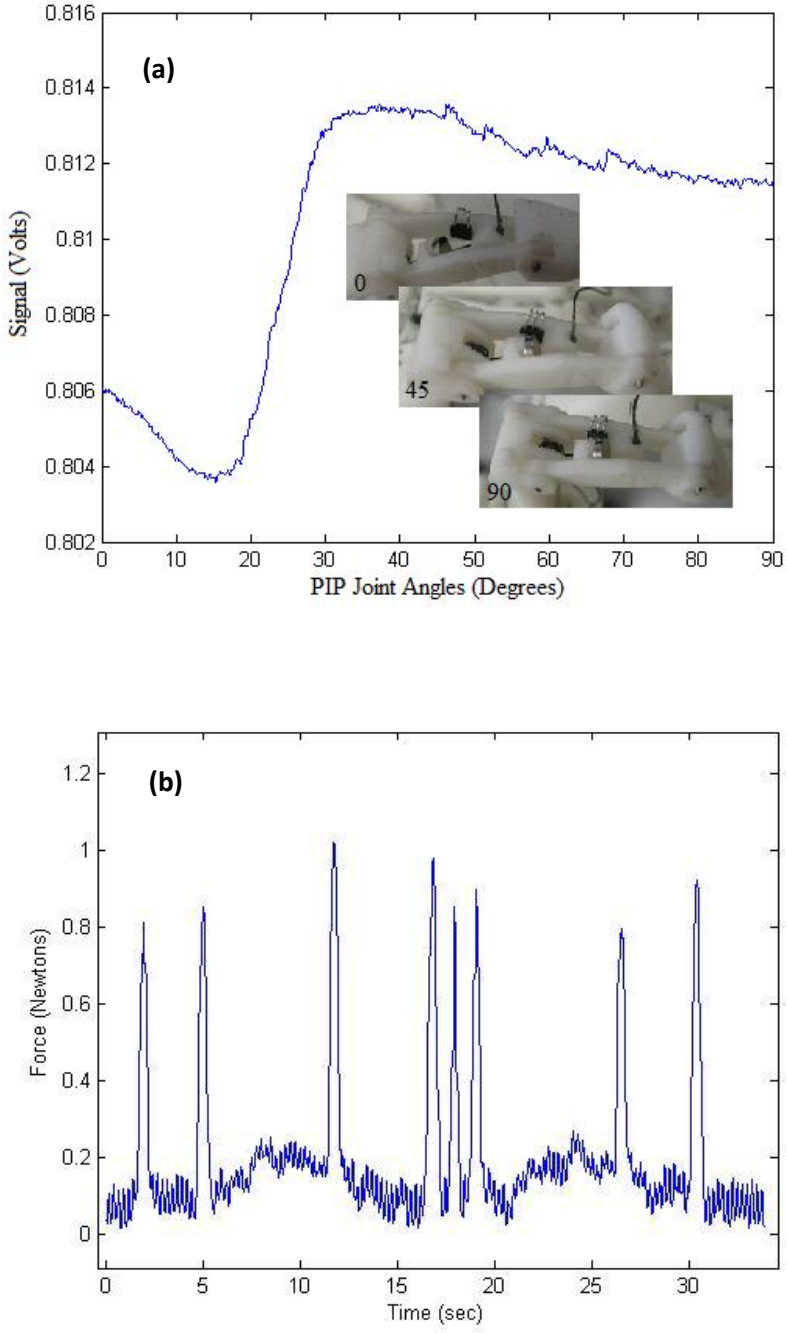

Figure 2.24: (a) Example signal acquired from Hall effect sensor in the PIP joint showing the magnet and sensor positions at 0, 45 and 90 degrees. (b) Example signal acquired from fingertip pressure sensor while typing a full sentence.

Pressure sensors (Tekscan ZFLEXA201-25) capable of measuring forces up to 25 lbs were placed at each fingertip in order to provide feedback as to when a key has been sufficiently

pressed. Figure 2.24 (b) shows the data taken while a human subject types "the quick brown fox jumped over the lazy dog". Each peak represents when the index finger hits a key and has a peak force range from 0.78 N to 1.1 N. This sensor is utilized to stop the MP joint from flexing once it reads a force value greater than 0.6 N so the finger does not continue into the keyboard after the key is struck.

All of the transformation matrices from the DH model as well as sensor inputs and outputs were run through MATLAB. Joint angles were solved and then converted into motor commands which are then sent to the controller through a serial port. With the current code architecture a typing speed of 20 words per minute is achieved using only right hand. With the addition of a left hand, a typing speed of over 30 words per minute is anticipated. Figure 2.25 (a) – (d) shows the prototype hand reaching different keys. While typing, the 19 motors experienced a peak current of 2.7A with a total average power consumption of about 6.4 Watts.

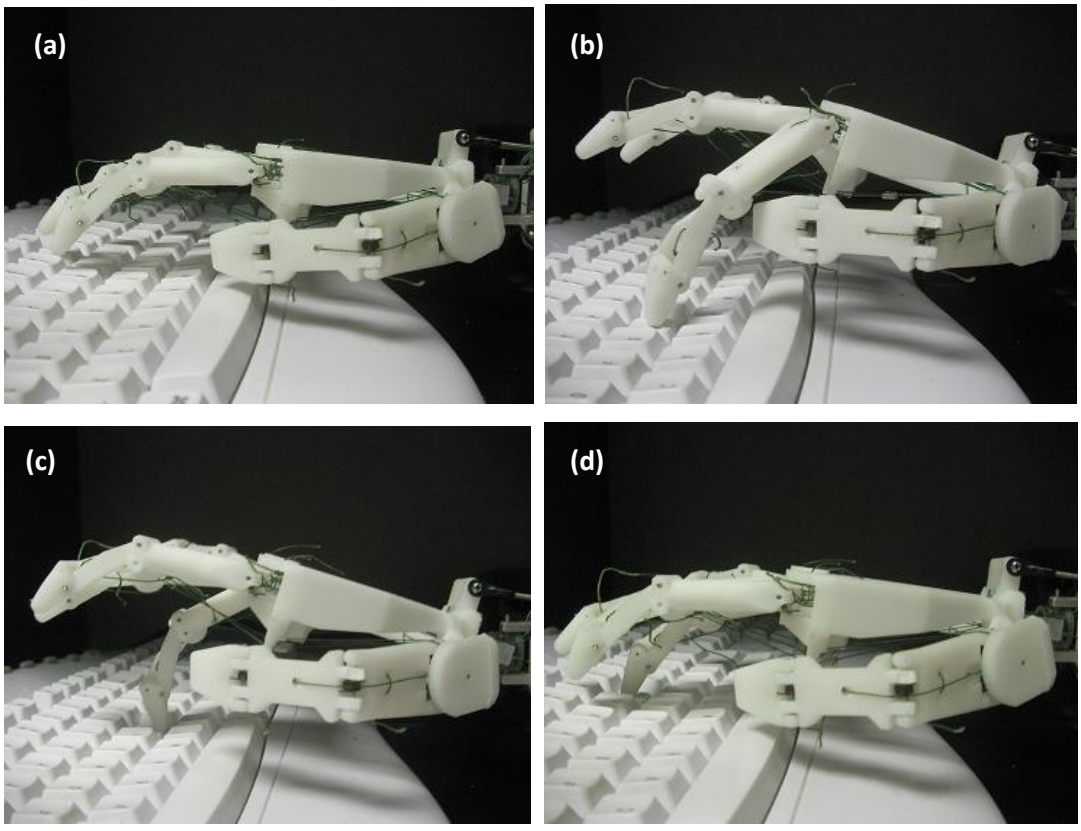

Figure 2.25: (a) – (d) DART hand typing, from top left to bottom right, "Y" "H" "L" "O".

Table 2.5 provides a summary of characteristics for the DART hand and highlights its excellent performance given the cost-effective design of this hand.

Table 2.5: Summary of humanoid and average human hand characteristics

	DART hand	Human (male)
Hand Size	180 x 90 x 50 (mm)	189 x 84 x 48 (mm)
Forearm Size	315 x 100 x 85 (mm)	275 x 88 x 75 (mm)
Hand Weight	0.09 kg	0.40 kg
Forearm Weight	0.96 kg	1.13 kg
Degrees of freedom	19	23
Joint ranges of motion (DIP, PIP, MP)	70, 90, 90 (degrees)	70, 110, 90 (degrees)
Grasp Speed	0.35 sec	0.15 sec
Fingertip Force	15 N	50.9 N
Typing Speed	20 words / minute	33 words / minute

2.5 Elbow and Shoulder Design

2.5.1 Elbow Design

Drivable arms and shoulders will allow us to simulate the combative patient as well as a physical examination in which the doctor gives the patient tasks to perform such as lifting their arms as high as they can. This system must also remain within human dimensions and must be able to carry some type of load, thus we must define some metrics. One of the goals of this project is to create a medical simulator while another future goal would be to branch out and design an elderly home assistant for activities of daily living (ADLs). With the medical simulator, there really is no definite required payload other than being able to lift itself so our system requirements will come from the elderly home assistant. So what types of ADLs would the robot be able to perform if arms were included with the hands? The answer is anything involving reaching objects or placing them down, holding objects in place or reorienting them in space. For instance, if someone were taking the groceries in and had their hands full, they might let the robot hold the bags while they open the door. If there is an object high on a shelf which someone could not reach then the robot could assist.

We start with the elbow and work up to the shoulder and chest. The human elbow is a single degree of freedom joint with approximately 170 degrees of rotation. At about halfway, the elbow is considered at the "carrying angle" which prevents the arm from making contact with the hips while swinging. A gallon of milk weighs roughly 8 lbs and is considered one of the heavier items found in the kitchen therefore we set a carrying weight of 10 lbs as our desired payload at the carrying angle.

We first considered going with a DC motor located in the upper arm and a 90 degree bevel gear transmission. This is an attractive option because the only moving parts would be the gears located at the elbow but that is also its weakness. Having those heavy gears at the elbow creates a significant moment arm when we go to design a shoulder mechanism, so other options were explored. Our final decision become driving the elbow with a stepper motor linear actuator due to its simplicity, low noise level and physical size. The motor would also be located close to the shoulder thus reducing the moment arm at the shoulder. The difficult with this type of actuator arises from the fact that a moment arm lever at the elbow would need to be designed. In this case, making sure the moment arm is long enough to output at least 10 lbs is a vital criteria as well as keeping it short enough to maintain human form. The final criterion is to be able to move from one extreme position to the other in a time that is similar to average human motions. The two parameters that affect these criteria are actuator speed and strength.

Using characteristics of the arm, such as weight and center of mass, two different MATLAB codes were written to visually represent the interaction between our parameters. A simple force balance about the elbow produces equation 2.20.

$$(Actuator\ \ Strength)*(Moment\ \ Arm\ \ Length)=(Lifting\ \ Strength)*17.5\,in \qquad (2.20)$$

Figure 2.26 below which shows the moment arm length versus actuator strength versus lifting strength at the hand. Actuator strength and moment arm length are inputs and the lifting capacity is the output.

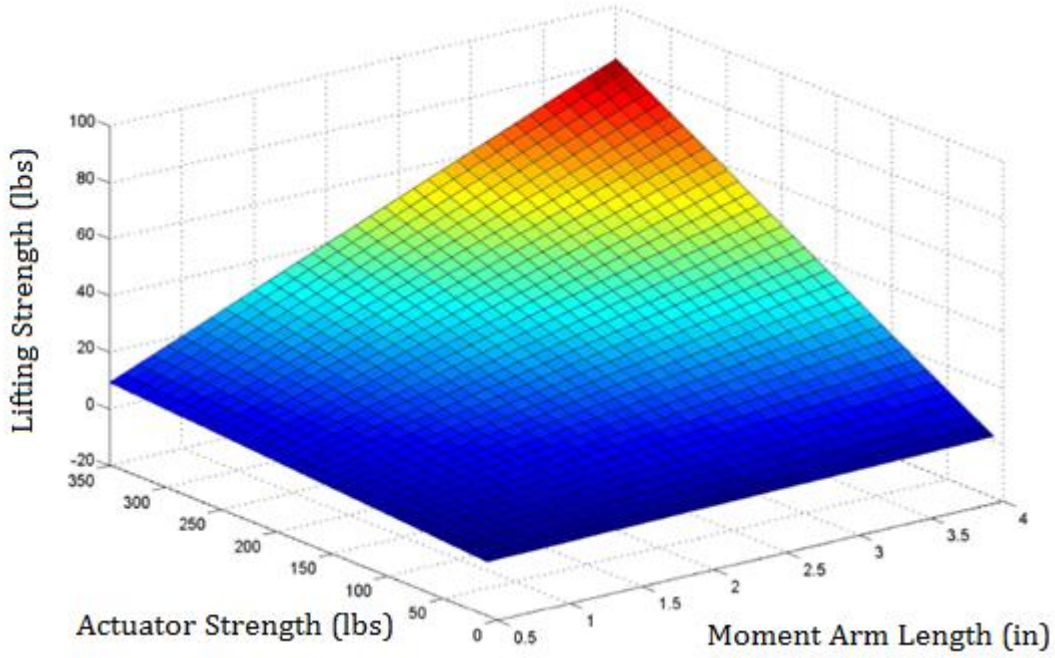

Figure 2.26: This plot shows the moment arm measured in inches versus the actuator strength measured in pounds versus the lifting strength of the arm measured in pounds.

The other critical actuator parameter is actuator speed. Again to visually represent the interaction between parameters, we have MATLAB graph the results which can be seen below in Figure 2.27. The graph compares the moment arm in inches, the actuator speed in inches/second and the time it takes for 90 degrees of rotation measured in seconds. The equation used to produce this figure is also shown below.

$$90\ Degree\ Movement\ Time = \frac{\sqrt{2} * (Moment\ \ Arm\ \ Length)}{Actuator\ \ Speed} \tag{2.21}$$

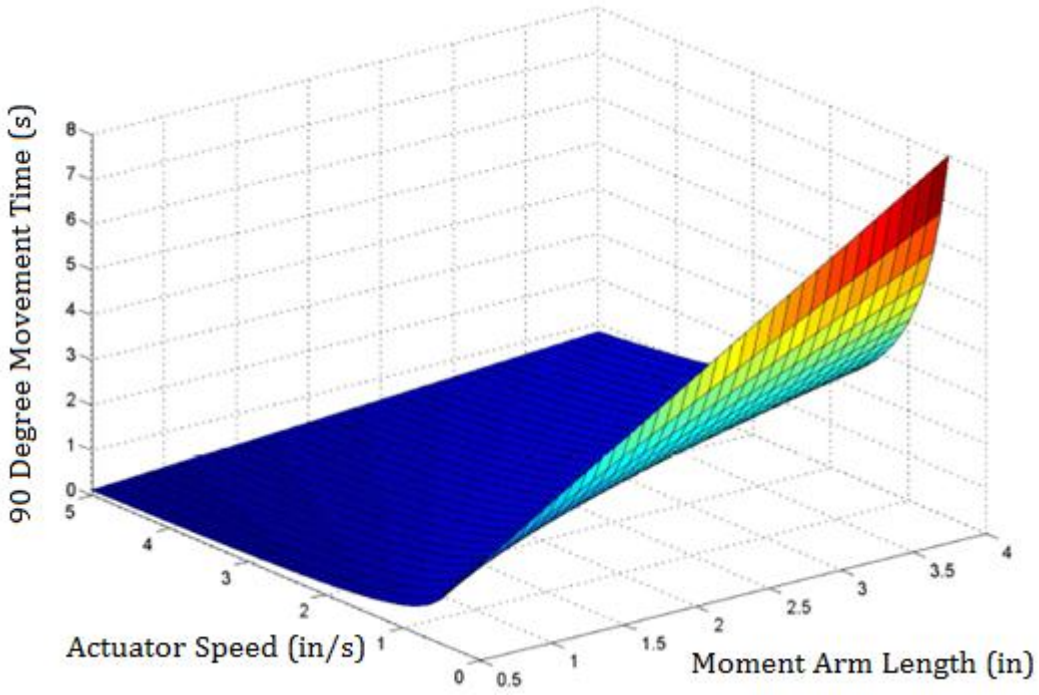

Figure 2.27: This plot shows the moment arm measured in inches versus the actuator speed measured in inches/second versus the time it takes for 90 degrees of elbow movement.

Looking at figure 2.27, the inputs that can be manipulated are moment arm length and actuator speed. The movement time of the arm is the result of the other two inputs. After analyzing the graphs we determined limits in order to narrow down our actuator selection while keeping in mind human appearance and capabilities. It was decided that the arm should move 90 degrees in less than 1 second to represent the movement capabilities of a human. Using this and our 10 pound load requirement, the three dimensional plots were sliced into two dimensions to better visualize the effect that actuator characteristics had on this system. Figure 2.28 (a) shown below represents the actuator strength versus moment arm length assuming a 20lb lifting capacity. An actuator based on a 20lb load requirement will allow for a strength safety factor of 2 which will help with dynamic loading, or unexpected spikes in load due to momentum. Actuator speed and moment arm length relationships are also shown at three different cycle times in figure 2.28 (b).

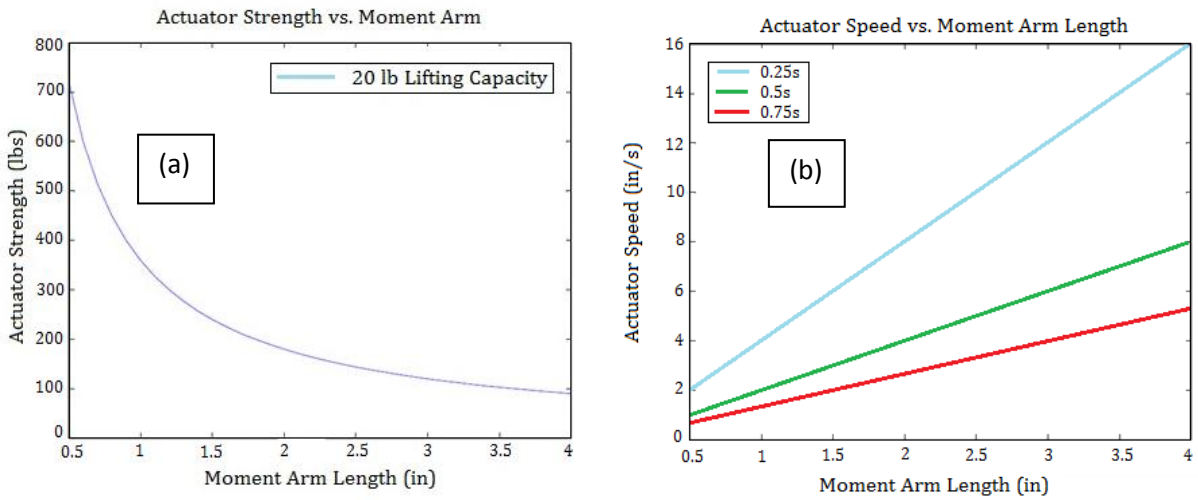

Figure 2.28: Theoretical performance characteristics of the elbow given varying actuator specifications and moment arm lengths.

The 2-D plots were used in the discussion of what length moment arm should be used for the elbow. The conclusion was drawn that a moment arm of 2 inches would satisfy the visual aesthetics of a human arm. From figure 2.28, we can now see that at 2 inches the actuator needs to output at least 200 lbs to meet the 20 lb requirement. We also see that the minimum actuator speed is about 2 inches per second to achieve 90 degrees of rotation in under a second.

A stepper motor based linear actuator that provides a maximum of 392 lbs and 5 in/s was selected and purchased. This actuator is also rated at a 100% duty cycle, which is an important performance characteristic for continuous operation. With the actuator selected, the design of the elbow was modified to fit its geometry. The upper arm frame was designed to use ½" steel square stock and the attachment module to the shoulder is made out of 1/8" plate steel to resist any flexion. The previously mentioned 2" moment arm is also made out of 1" solid square stock aluminum which was shaped to allow the arm to articulate approximately 135˚ to help mimic the natural human range of motion. Figure 2.29 shown below illustrates the elbow actuated in its two extreme positions: fully extended and fully bent.

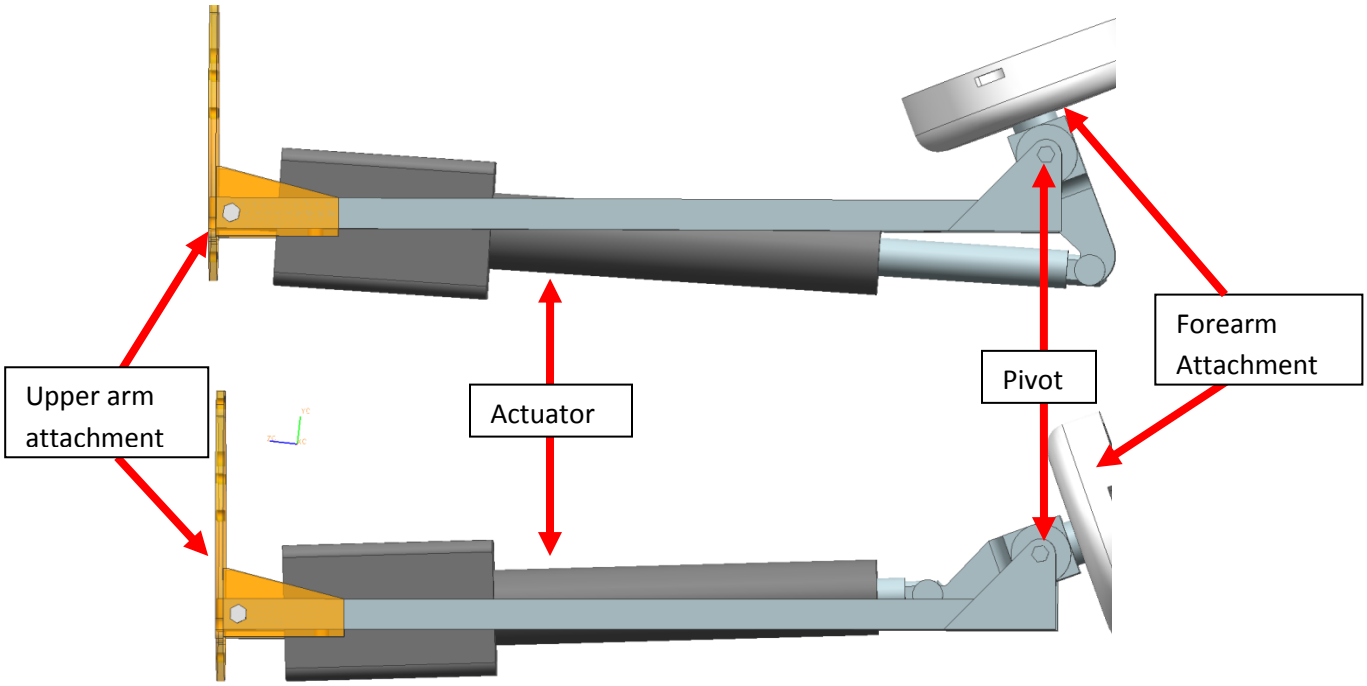

Figure 2.29: The top image illustrates the actuator fully extended which causes the elbow to reach its maximum bending position of 135°. The bottom image shows the actuator fully contracted allowing the arm to be straight.

At the articulation end of the structure, the pivot point is offset 2" forward to the upper arm attachment plate. This is necessary to allow the full 135˚ of motion and yields a more human-like appearance. This offset will allow the linear actuator to be placed on the backside of the arm, while still allowing the elbow to be in line with the shoulder. Placing the linear actuator on the backside of the arm also leaves the top of the arm open for other components.

The upper arm attachment plate can be seen in figure 2.30. Several holes for mounting shoulder actuators are included and will be discussed in the following paragraphs. Mounting braces have been added to the plate to help hold the ½" square stock in place while still providing modularity to the design. The entire design can come apart if the need for servicing or adjustment is necessary.

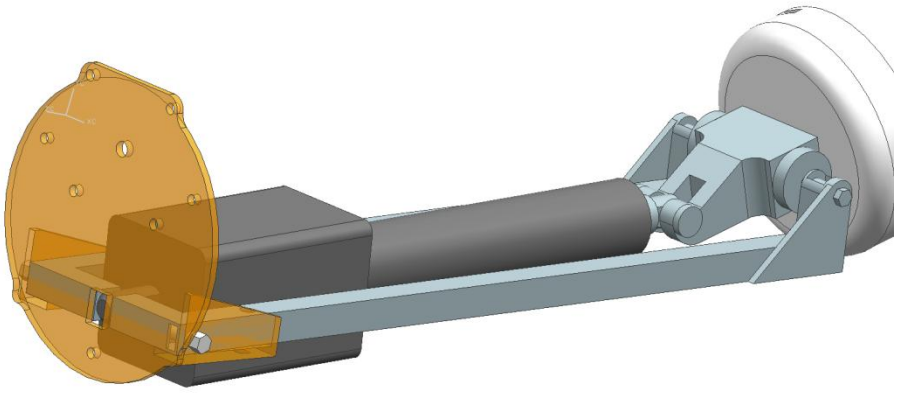

Figure 2.30: The upper arm attachment plate secures the elbow actuator as well as attaches the lower arm to the shoulder.

2.5.2 Shoulder Design

Investigating the human body, [8] shows us that three degrees of freedom are present in a shoulder joint and are illustrated below in figure 2.31. To properly recreate the motions of a human it was determined that each degree of freedom needs its own actuator.

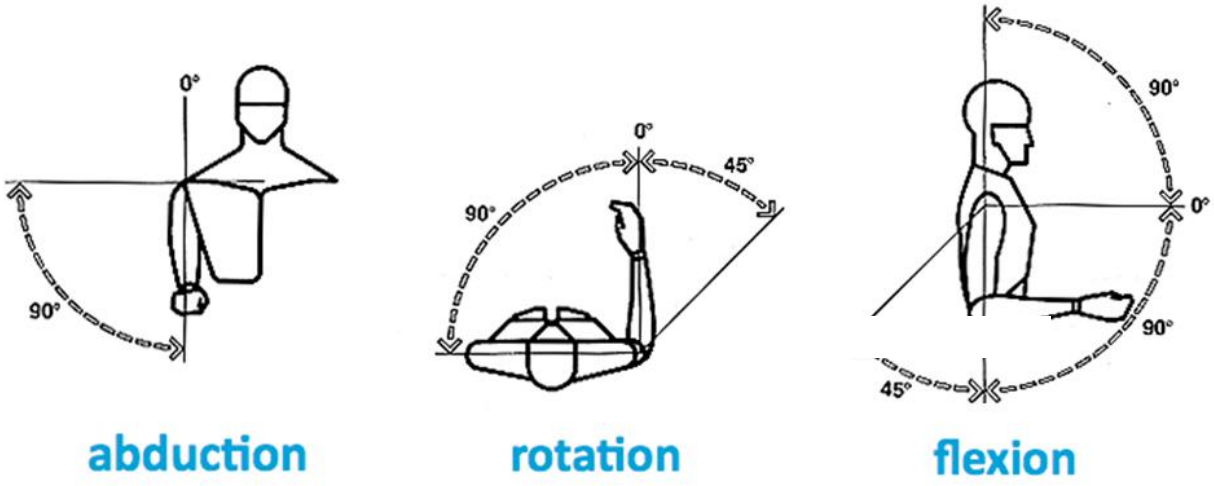

Figure 2.31: The shoulder has three degrees of freedom which are illustrated here.

The first step is to properly size the actuators, which means coming up with a maximum operational load. While the elbow is lifting its maximum rated load, it is assumed that the shoulders will not be actuated. This allows us to create a completely new set of specifications for the shoulder motors.

Maximum shoulder loading will occur when the shoulder and elbow are completely horizontal with the ground and pointing away from the body. We can create a force balance at the shoulder using the weight of the hand, forearm and components of the upper arm based on CAD designs and estimations of material weights. This is shown in figure2.32.

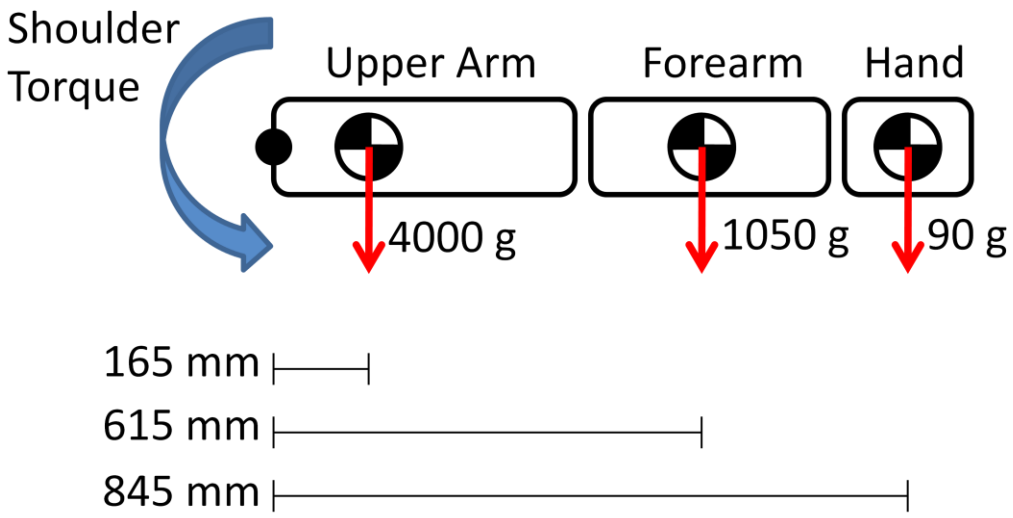

Figure 2.32: Force balance of the entire arm assembly to determine required motor torque at shoulder.

This force balance is calculated in equation 2.22 below.

$$T = g*\left((M*COM)_{ARM} + (M*COM)_{FOREARM} + (M*COM)_{hAND} + (Load\ at\ Hand)*COM_{Load}\right) \quad [2.22]$$

$$T = 9.81*\left(4kg*0.165m + 1.05kg*0.615m + 0.09kg*0.845m + (Load\ at\ Hand)*0.845m\right)$$

When a person reaches for an object in a high place, rarely do they extend their arm into a position like this. A person will most likely reach the object and keep it close to their body while maintaining a vertical forearm position. Thus we decided that 5 lbs (2.3 kg) would be a

suitable maximum load in this position. When we plug this number into equation 2.22 we find that the required torque from the shoulder motor is 32.6 *N-m*.

Several motors were investigated and we discovered that the 34K314S stepper motor from Anaheim Automation [97] met our criteria. The graph below shows the power curve for the motor.

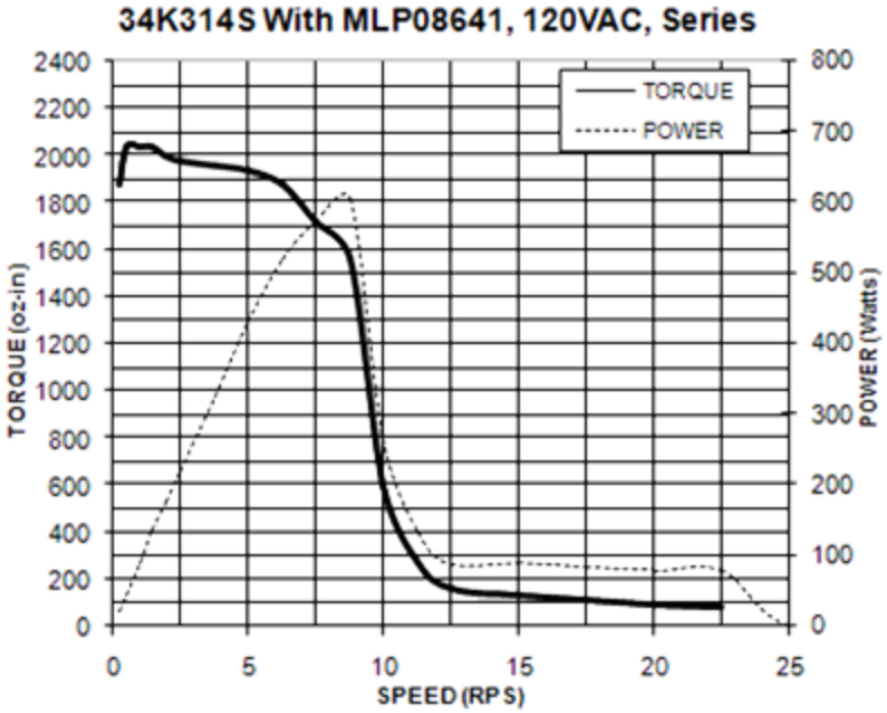

Figure 2.33: Power curve for the 34K314S stepper motor which is used to abduct/flex the shoulder [97].

This graph shows that the optimal speed to run the motor at is about 8 or 9 rotations per second (RPS) and a maximum stall torque of 2050 oz-in (14.2 N-m) at around 2 RPS. Driving the robot arm at 2 RPS would destroy the system thus there needs to be some gearing between the motor and arm to reduce angular velocity. The gearing would also serve to increase the torque output of the shoulder since we need at least 32.6 N-m, thus we choose a 3:1 ratio giving us 42.6 N-m of output torque at the shoulder. A similar procedure is performed to choose the motor for shoulder rotation. We still assume a load of 5 lbs is the maximum load which leads to a maximum moment of 12 *N-m*. The 23L303S-LW8 from Anaheim Automation is capable of outputting 2.26 *N-m* directly so we couple it with a gear-set that has a 10:1 ratio for a final torque

output of 22.6 *N-m*. A CAD rendering of the final shoulder and chest assembly can be seen in figure 2.34.

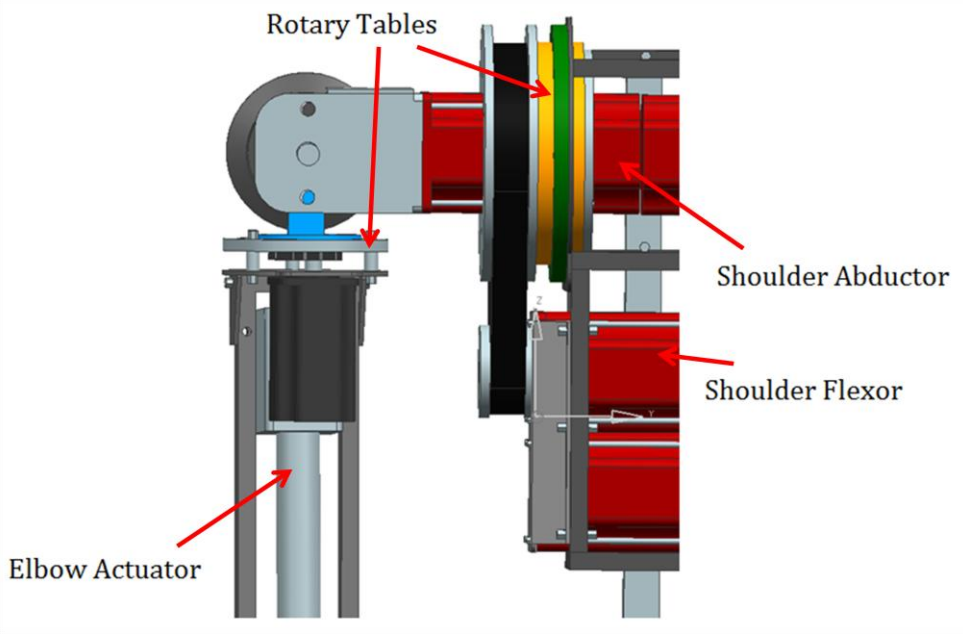

Figure 2.34: CAD file of complete shoulder and chest assembly.

The lower half of the upper arm (where the linear actuator resides) is attached to the outer ring of a rotary table. This rotary table allows the shoulder to rotate while maintaining a rigid connection between the lower arm and motors. Continuing up the arm, a connection piece (blue piece in figure 2.34) was fabricated to attach to the rotary table on one end and the rotating shaft in the gearbox on the other end. This piece utilizes a keyway to ensure a proper fit and transfer of motion from shoulder abductor motor to the entire arm.

This gearbox accomplishes both the gear reduction and 90 degree motion transmission with one set of bevel gears. Figure 2.35 shown below illustrates the new gearbox with one set of reducing bevel gears responsible for the 3:1 reduction and directional change of motion. Covers have also been added to the gearbox to increase rigidity and help protect the gears. Two bearings were used to secure the shaft in place and receive any corresponding loads placed on the system. The larger bevel gear attaches to the connection piece to ensure an even better transfer of force and rigidity on the system. As seen in the figure, extra shaft length was left extruding out of the gearbox for placement of encoders or similar feedback sensors.

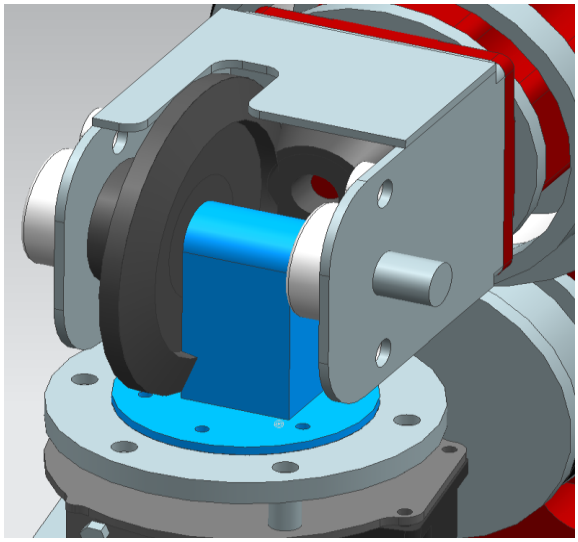

Figure 2.35: Final design of the gearbox achieves speed reduction and change in rotation direction by using beveled gears.

The system utilizes a timing belt system in order to cause flexion and extension of the shoulder. This mechanism actually rotates the motor responsible for abduction and adduction of the shoulder as well as the entire arm. Using a timing belt versus a set of spur gears greatly reduces the weight in the system as well as cost. The pulley design consists of rapid prototyped cores with aluminum sheet bolted to the sides which allow us to create the pulleys exactly as needed. The upper pulley forms directly around the upper stepper motor and the lower pulley attaches to the lower stepper motor's output shaft. A tensioning system is used to adjust the belt tension as needed while still allowing easy assembly and disassembly. Utilizing a tensioner allows the mountings of the stepper motors to be fixed while still having adjustability in belt tension which greatly reduces complexity of the design.

It was at this point that we realized weight might start becoming an issue, especially with 4 motors, each weighing 12 lbs, mounted within the chest. Although we spent a great deal of time designing a three DOF shoulder, we had to eliminate one of them in order to remain within human-like weight. The additional weight would have made it nearly impossible to find a way to actuate the waist. In robotics, weight has an additive effect; the more weight there is, the more weight there will be. In order to actuate heavier systems, heavier motors must be used. For this reason we decided to eliminate shoulder flexion/extension. For the sake of simulating the

combative patient it makes little difference because movable limbs are simply creating the illusion of distress. As for the elderly assistant, a slight modification in the motion planning will have to occur. For instance, instead of simply reaching for the object, the robot will have to twist its torso until it is in the proper orientation, then it can reach for the object in a similar manner. This modification greatly simplifies the design and a picture of the final system can be seen in figure 2.36.

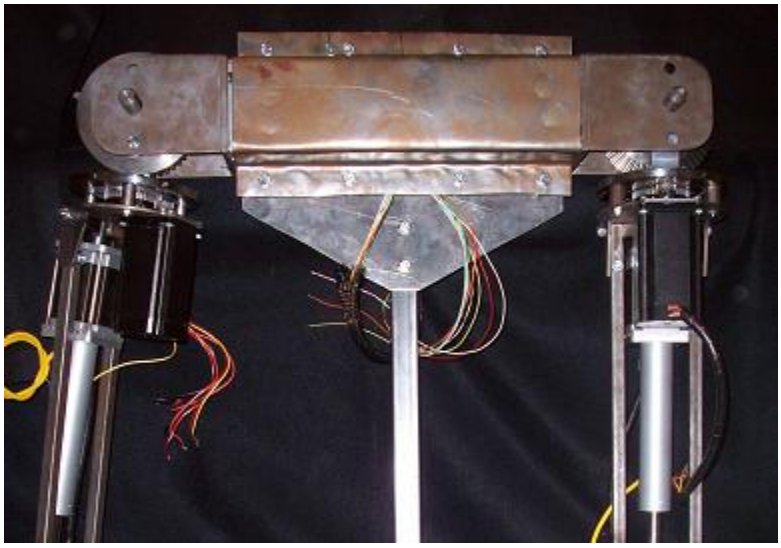

Figure 2.36: Photo of the assembled robotic upper body with elbow flexion/extension, shoulder abduction/adduction and shoulder rotation.

Chapter 3

Biomimetic Face, Eyes and Neck

3.1 Skull Design

3.1.1 Determining Required Muscle Sets

Designing an expressive robotic face requires a balance between functionality and anthropomorphism. The biggest overall challenge is to fit all the necessary hardware into roughly 275 cubic inches. As pointed out in an earlier study [anthropomorphism and the social robot], the goal in design should be to replicate the parameters that play a vital role in creating expressions, not completely mimicking human physiology. The Facial Action Coding System, or FACS [23], is often times used to specify the control points and the direction of action in robotic faces. It provides summary of facial muscle groups, or action units, and how they coordinate to produce expressions. We chose to use FACS to determine the insertion points of all necessary muscle groups as well as to help eliminate those groups that are not essential in communicating patient states in order to meet volume constraints.

Through collaboration with doctors at Carillion Clinic we have determined that the most important facial expression for medical diagnosis is grimacing. For example, if a medical student did a proper exam of the abdomen for appendicitis then the patient might make varying levels of grimacing based on the severity of pain. Coupled with speech and other body gestures, the mannequin becomes an effective communicator of mental and physical state. Grimacing employs action units (AUs) 4, 9 and 20 which can be seen in figure 3.1 (a).

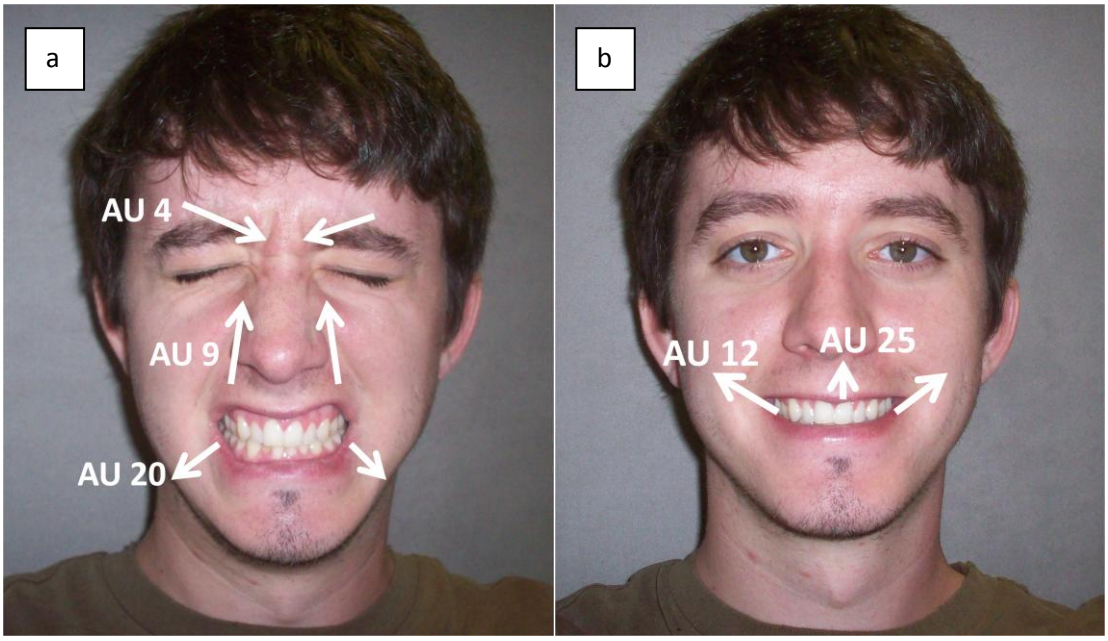

Figure 3.1: Example Action Units responsible for (a) grimacing and (b) smiling.

Initial communication with a patient, or triage, is critical to finding their main complaint. Medical students should be trained to pick up on cues such as eye contact, body language or how the patient answers questions in order to uncover the reason for their visit. For example, after a stroke, the patient may have some memory loss and a slight droop to one side of their face which becomes evident when smiling since these AUs produce a large deformation. The AUs responsible for smiling can be seen in figure 3.1 (b). Other AUs that are important are inner and outer eyebrow raising, blinking and pushing the chin boss upwards. These AUs help in generating facial expressions like fear, anger, disgust, surprise and sadness.

3.1.2 Skull and Skin Fabrication

The function of a skull is to provide a support structure for skin as well as housing for mechanical components, motors and electronics. Creating a skull has been a highly iterative process since there are many methods to do so. We began by capturing the details of a participants face using skin-safe molding putty from Smooth-on Inc. We then covered the inside of this negative mold with a layer of molding clay which will represent the skin on the final product. The thickness was chosen based upon experimental results where a participant pinched several locations of their face while a pair of calipers measured the corresponding thickness and

half of the thickness measured is the thickness of the skin at various locations on the face. A photo of this procedure is shown in figure 3.2. After the clay completely lines the inside of the mold, plaster was poured into the remaining space, allowed to cure and then removed along with the clay.

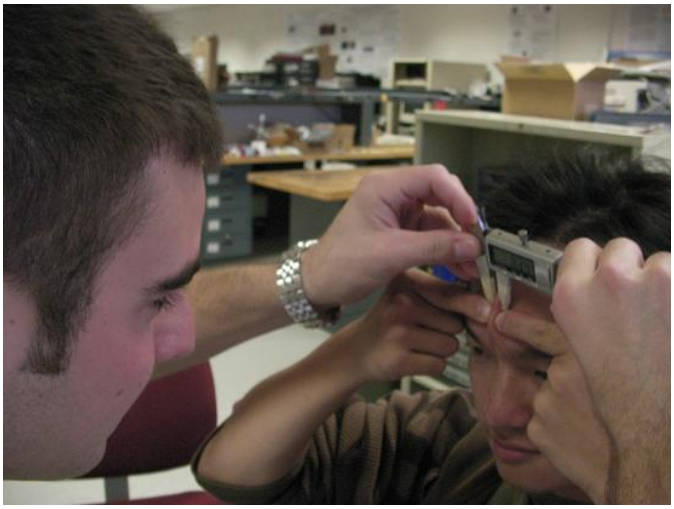

Figure 3.2: Pinch test performed to determine proper skin thickness of the robot

This plaster model now represents the structure that the skin will lay upon. This "skull" was hollowed out in order to create space for motors, mechanical components and electronics. Since this skull was constructed out of plaster it does not have the structural rigidity to handle the forces it will eventually see; therefore, we needed to mold it out of a new material. We selected to create a 3D digital image of our skull using a laser scanner since we can then manipulate the model with CAD software (shown in figure 3.3 (a)). The finished CAD file can be seen in figure 3.3 (b). The beginning of the arrows indicates where the skin will be pulled and the arrowheads point towards the holes in the skull for the wire to enter and eventually attach to an actuator. The circles in figure 3.3 (b) help illustrate the location of these holes. After the CAD file was complete a Dimension series 3D rapid prototyping machine with 100 micron z-axis layer resolution was used to print our skull. The machine prints in ABS plastic which has a high enough modulus to sustain all of our loads. Instead of printing the skull in one solid piece, it was separated into a jaw and two equal halves to improve the failure strength.

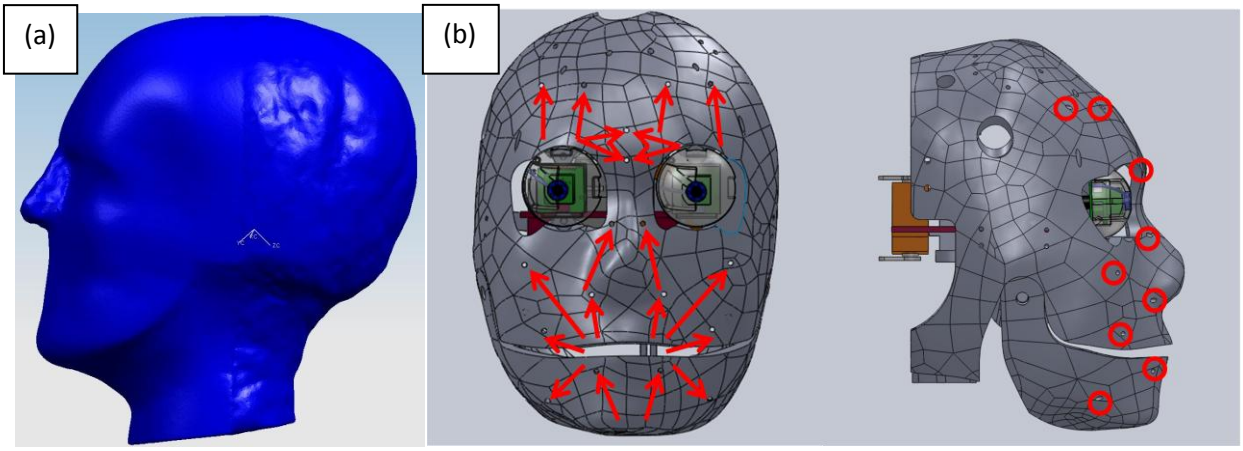

Figure 3.3: (a) Initial and (b) final CAD rendering of our "skull" created from a 3D surface scan.

Silicone is used for several robotic faces [33. 34, 35, 43, 70, 85, 88] because it is easy to work with, cures at room temperature and feels very similar to human skin. Silicone can also achieve large strains with little stress and has a large elastic deformation band. We purchased our silicone from Smooth-on Inc. along with several different silicone pigments to achieve variation in skin tone.

The skin is fabricated by inserting our plaster positive mold of the skull back into the negative mold of our participants face. There is now a void where the clay used to be and this is where the silicone will be poured into. The silicone is a mixture of three parts: part A, part B and thinner. Part A and B will cure into silicone within 45 minutes and the addition of thinner will make the mixture softer after it cures. Several samples with varying levels of thinner were created and tested against the skin on our cheek in order to determine the best feeling skin. We also made sure that the skin did not tear under twice the expected strain seen while making facial expressions. The overall mixture ended up being 27.5% part A, 27.5% part B and 45% thinner. After the silicone mixture was poured into the void and allowed to cure, the negative mold was removed and the skin was painted and modified for mouth and ocular orifices.

The servo motors chosen to drive the hand mechanism were also chosen for the face due to their small volume and low cost. A force sensor was attached to each of the anchor points on the face to test how much force was required to produce the desired amount of facial

deformation. After testing each point, we discovered that the HS-5125 motor had sufficient torque to pull each anchor point to their maximum deformation with the exception of the jaw which is driven with an HS-5645.

3.2 Biomimetic Eye Design

Human eyes provide a wealth of knowledge to a well-trained doctor. Eye contact, gaze direction and duration, movements, dilation, tearing, shape, color and blinking all communicate information that can be used to help establish the state of a patient. It has been pointed out that proper geometry of eyes helps in interpreting the robot's gaze and thus improving interaction [19]. [55] states that expressive faces with the ability to make eye contact and track faces helps in improving the social relationships between robots and humans. DiSalvo et al. have mentioned that people are very sensitive to attentional cues, mutual gaze, and eye contact, thus, how a robot moves its eyes is important so that it feels natural and does not violate people's expectations [21]. They collected 48 pictures of robots with varying levels of human features and asked participants to rate their resemblance to humans. The authors found that eyes were the feature that contributed most to human-like perception. All these prior studies indicate the importance of eyes in an expressive robot and thus we spent significant effort in this study on design and integration of the eyes.

Two DOF for motion, independent upper and lower eyelid motion and independent pupil dilation were chosen as the necessary capabilities to recreate the human eye. It has been shown that the range of motion for the typical human eye is 120 degrees of horizontal rotation and 70 degrees of vertical rotation [8]. These ranges can be achieved at speeds faster than humans can perceive. Saccades, quick movement of both eyes, are typically accomplished in between 20 to 200 milliseconds [12]. Even at these speeds the eyes cannot process the image of the object and must be accompanied by the aid of other motions such as the head to keep the object focused [95]. Eye movement should be quick, similar to that of human eyes; therefore, we decided that full range of motion should be completed in less than 0.5 sec, with blinking and dilation occurring around 200 milliseconds [25]. Most humanoid medical simulators contain only few of these capabilities mainly due to size limitations of the eye.

The entire eye mechanism was designed to fit within the confines of a skull; therefore, the mechanism's platform could be no larger than 120 x 160 mm with a height no more than 50 mm. The eyeball had four major components: an outer shell, iris diaphragm, Microsoft HD 6000 webcam and a universal joint, as shown in figure 3.4. The plastic shell casing was created with a Dimension-series rapid prototyper with a 0.1mm vertical and horizontal layer resolution. The plastic is a semi translucent white color that accurately resembles the hue and texture of a human eye. This shell contains the rest of the eye mechanisms and provides mounting for actuating rods.

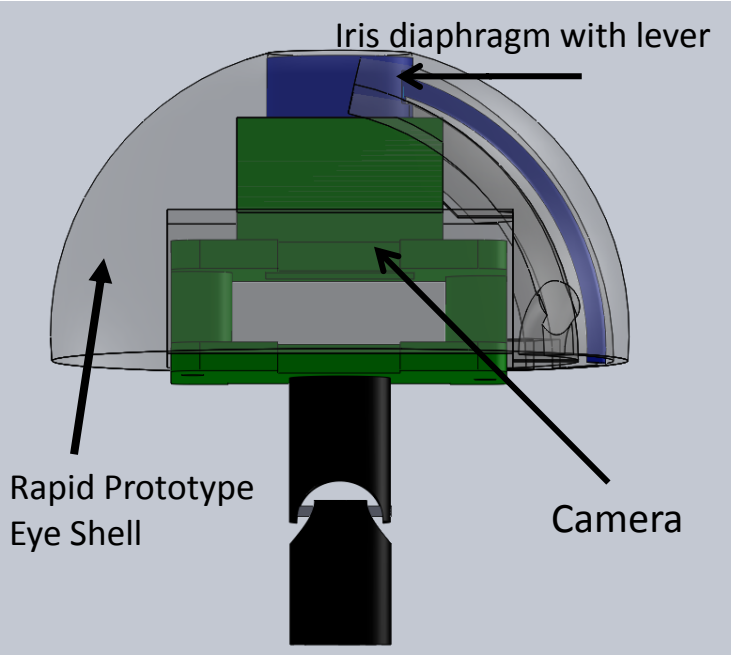

Figure 3.4: The finalized eye design with rapid prototype shell in grey, iris diaphragm in blue with lever, HD 6000 webcam in green, and u-joint in black.

Figure 3.5 shows the CAD file of the eye mechanism and its mounting platform. All the components were mounted on one platform for simplicity of mounting and repair. The assembly can be quickly removed by disconnecting the blinking servo horns and unscrewing two sets of screws. Yellow servos move the eyes by using a dual linkage system that attaches to an adjacent servo horn via ball joints and turnbuckles. This mechanical setup allows us to simulate 4 DOF by using only 2 motors. Blue servos actuate iris dilation and are located on the underside of the platform in order to line up with the exit hole where Bowden cables attach. Our Bowden cable system is a nylon polymer chord in a semi elastic sheath and allows the eyes to move without pulling the iris cable and is critical because the actuator for iris dilation is not located within the

eye. To eliminate as much friction in the cable as possible, large angle bends are avoided and a spray lubricant coats the inside of the cable sheathes. The orange servos will actuate the upper and lower eyelids independently. The eyelid mechanism consists of two thin sheet-steel lever arms which pivot about an axis directly between the eyes. The length of the lever arm was determined by the space required to clear the eye assembly. The area of the mechanism which is adhered to the back of the eyelids is bent to match the profile of the eyes and helps create a seamless transition from skin to eye.

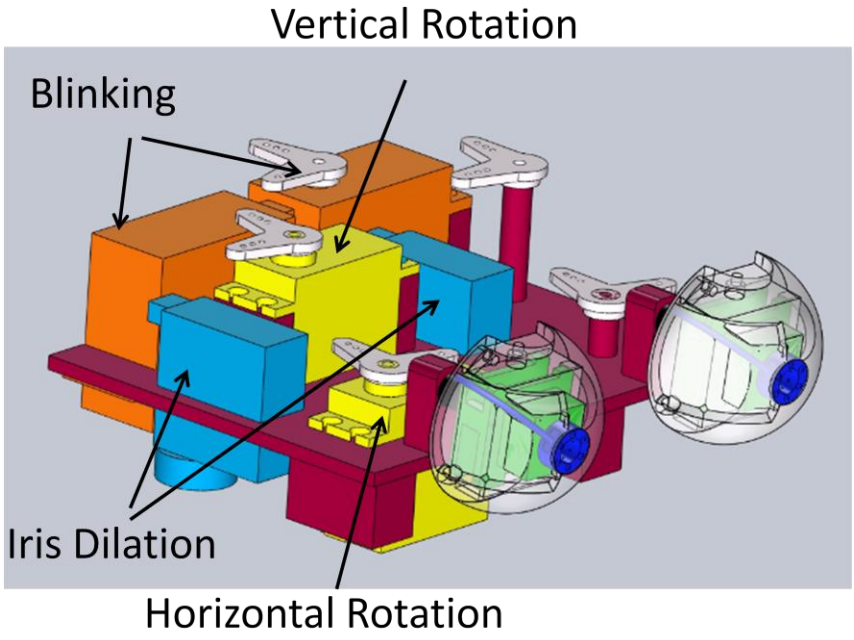

Figure 3.5: Cad model of base platform with movement servos, iris dilation servos, blinking servos and eye assemblies.

Pupil dilation can be used to detect consciousness, brain damage, eye damage and several other medical conditions. We have incorporated this mechanism into our design using a small iris diaphragm aperture created for small cameras and laser applications. The diaphragm is a high performance shutter lens system that is placed between the camera and the outer shell of the eye and is actuated via a Bowden cable which slides a lever to open and close the shutter at desired levels. The device has an outer diameter of 10 mm thus mimicking the size of a human iris. The diaphragm also accepts color which allows us to mimic the natural color of human eye. The Microsoft HD 6000 webcam was chosen for its size, functionality and speed. The camera PCB is

25 x 25mm and the overall height is less than 20mm, which is suitable for fitting in the limited volume of the human eye. Resolution is 720p and it can take video at 30fps over a standard USB connection. A commercial universal-joint was connected to the back of the camera via epoxy that allowed the entire assembly to swivel with 2 DOF. Figure 3.6 (a) shows the final assembly and figure 3.6 (b) shows the iris shudder mechanism in three different positions.

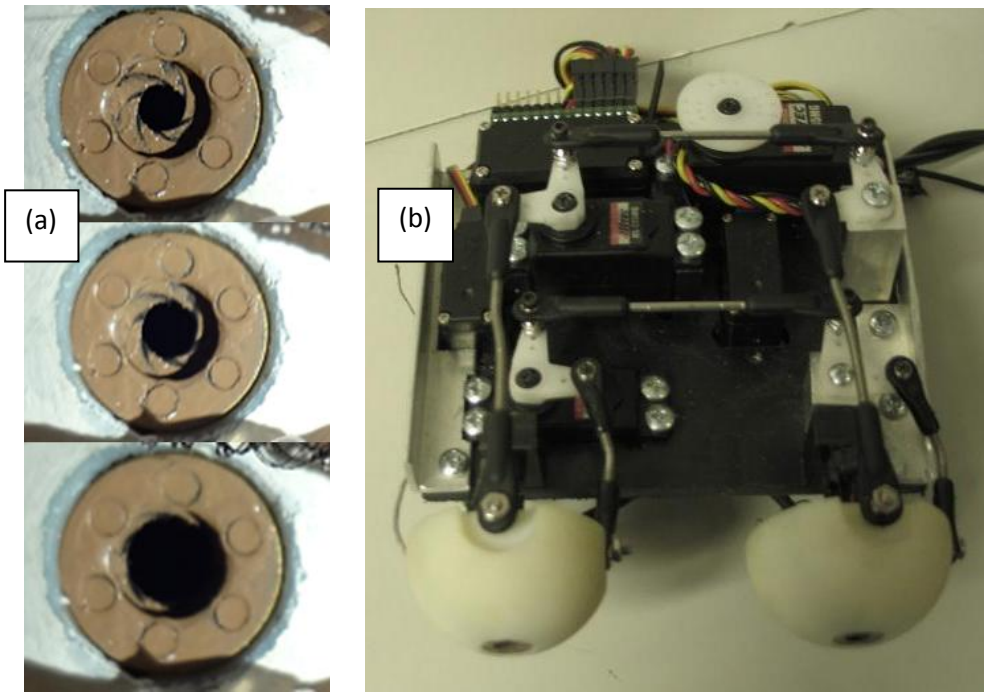

Figure 3.6: Photograph of (a) iris shudder mechanism in three different positions and (b) the prototype eye mounting plate to be placed in the skull.

The weight of the eye assembly was 517g with a volume of 884 cm^3 which is 23% of the 4000 cm^3 within the skull. The movements and speeds were realistic and met the specifications as described later in this paper. Testing for ranges of motion, speed and field of view were done with a high-speed camera and picture overlaying software. Range of motion from left to right was 69° and up to down was 55°. The speed from one extreme to the other in both x and y directions was 210°/sec which results in looking left to right in $1/3^{rd}$ of a sec. This allowed us to decrease the acceleration and velocity of the servos to reduce system noise. Field of view was calculated by measuring the distance at which a 300mm long ruler is completely visible. We found that the field of view was 42° when the iris diaphragm was open and 31° while constricted.

3.3 Analysis of Action Units

3.3.1 Graphical Facial Expression Analysis and Design (GFEAD)

Since the robotic face will be used for medical purposes where it is important to estimate emotional state based on facial expressions, quantifying the degree of an expression becomes important. We began with a tracking technique which measures the perceived deformation of certain areas of a person's face from the frontal plane. Figure 3.7 (a) shows the tracking points and figure 3.7 (b) shows the coordinate system. The participant was asked to make several faces such as surprise, anger, sadness, pain, happiness and fear. Similarly, this technique was performed on the robots face as seen in figure 3.7 (c). The maximum X and Y positions of each point with respect to the origin were recorded and the results are shown in tables 3.1 and 3.2.

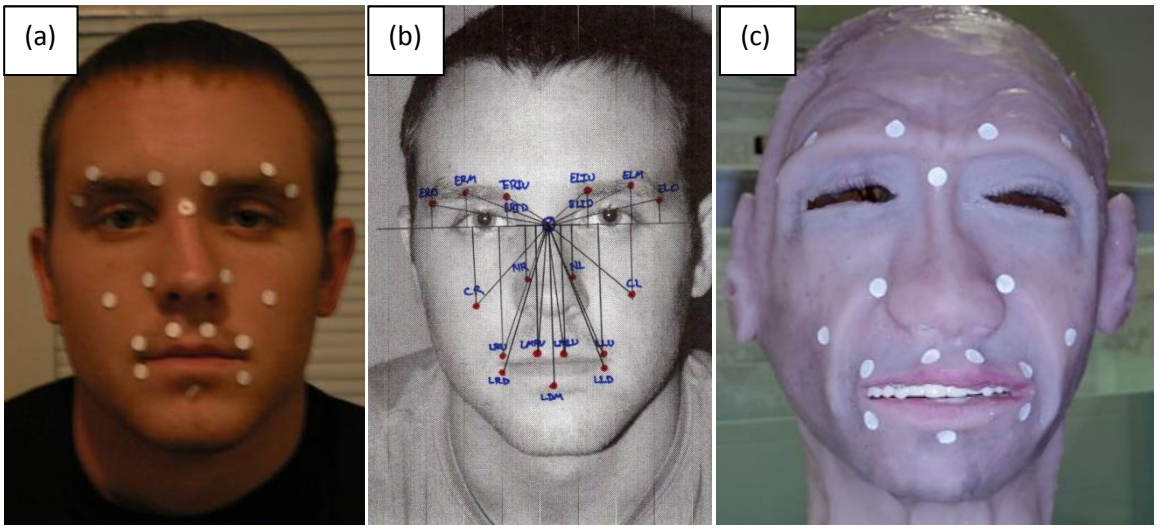

Figure 3.7: Facial tracking points on participant (a) and robot (c) with coordinate system shown in (b).

Table 3.1: Frontal plane deformation results of facial point tracking on human subject

	Frontal Plane Travel (mm)		
Attach. Pt.	X	Y	Abs. Dist.
ERO	6.9	20.3	21.4
ERM	6.9	16.0	17.4
ERIU	4.3	15.0	15.6
ELO	3.0	19.3	19.5
ELM	3.0	16.0	16.3
ELIU	4.3	9.7	10.6
NR	4.1	6.9	8.0
NL	3.0	5.8	6.6
CR	0.0	13.4	13.4
CL	2.5	9.1	9.4
LRU	10.9	4.1	11.7
LRD	7.9	20.8	22.3
LMRU	0.0	5.1	5.1
LLU	15.0	5.1	15.8
LLD	11.9	25.9	28.5
LMLU	0.0	7.9	7.9
LDM	3.1	27.5	27.7

Table 3.2: Frontal plane deformation results of facial point tracking on robot

	Frontal Plane Travel (mm)		
Attach. Pt.	X	Y	Abs. Dist.
ERO	3.0	6.0	6.7
ERM	3.0	13.0	13.3
ERIU	2.0	6.0	6.3
ELO	3.0	5.0	5.8
ELM	0.0	11.0	11.0
ELIU	2.0	5.0	5.4
NR	3.0	7.0	7.6
NL	7.0	10.0	12.2
CR	3.0	8.0	8.5
CL	9.0	7.0	11.4
LRU	8.0	8.0	11.3
LRD	3.5	11.0	11.5
LMRU	3.0	7.0	7.6
LLU	6.0	7	9.2
LLD	3.5	11.0	11.5
LMLU	0.0	8.0	8.0
LDM	2.5	11.0	11.3

A graphical comparison between the absolute distances of the participant and robot is shown in figure 3.8. Certain points like the nose and cheeks deformed similarly while others, like the eyebrows, and lower lips show that the robot falls short of human capabilities. These discrepancies deserve investigation and to do so we used GFEAD [87]. GFEAD is a graphical method of determining the facial deformation of human faces using two dimensional planes. It can be used to analyze the deformation for a given configuration of actuators on the face or it can be used to select. The method formulates successive auxiliary planes to find the exact plane in which the facial control points are located. Once the orthogonal plane holding the control point and action units with their exact length have been identified, the effect of each motor/anchor wire attached to control point can be analyzed. The analysis can be done by observing the effect of anchor wire independently or in combination with other wires for displacement amplification. It can also identify the direction of movement in auxiliary plane and provide its projection in the frontal plane of the face.

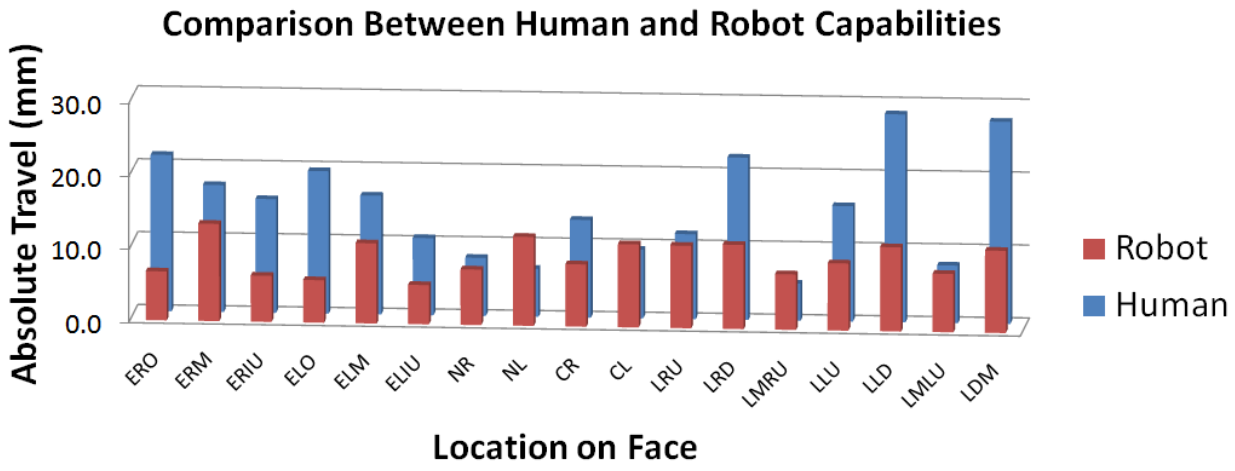

Figure 3.8: Comparison of absolute frontal plane distances from facial tracking experiment.

To utilize the GFEAD we begin by taking three dimensional coordinates of two points along the axis of each motor, sinking points and anchor points. Figure 3.9 shows a CAD file of the skull with the chosen coordinate system and one set of motor, sinking and anchor points. We now draw an arbitrary axis between the side-plane and frontal-plane views of the skull and measure the distance from this axis and the points from the side-plane view. The next step is to find a new two-dimensional plane that the servo resides within at any time. To do that, we draw a new arbitrary axis perpendicular to the line formed between the motor axes (blue) points. We

now project the points in the frontal-plane over to this new plane which we will call the first auxiliary plane (A_1). Since the motor axis lies within the Y-Z plane we only need to produce one auxiliary plane to achieve this view. The radius of the servo horn was 20mm so we can draw a circle around the motor axis which represents all possible locations for the tip of the horn. We also know that the servo can only rotate 90 degrees so when we installed the motors and horns we made sure to take advantage of as much pull distance as allowed by the system. The two lines emanating from the center of the horn in figure 3.10 represent the starting and finishing points of rotation and are synchronized with the sinking point.

Figure 3.11 shows the wire that will travel from the sinking point to the motor horn in the starting and finishing position. The next step was to find a plane that contains all the points of the wire traveling from the sinking point to the motor horn in order to find its true length. To do this, we draw another axis parallel to the wire representing the starting position of the motor and project the sinking point and motor horn tip. The distance between these two points in auxiliary plane 2 represents the true length of wire, L_1, before the motor has rotated. In figure 3.12, the same was done for the line representing the ending position of the horn after the motor has rotated. The difference between L_1 and L_2 represents the total amount of wire that can be pulled through the sinking point given the orientation and placement of the motor in the skull. The last step was to create another arbitrary axis parallel to the line formed between the sinking and anchor point in the first auxiliary plane. These two points are projected into auxiliary plane view 4 and the length between them, L_3, represents the maximum distance that can be pulled without forcing the anchor point into the sinking point.

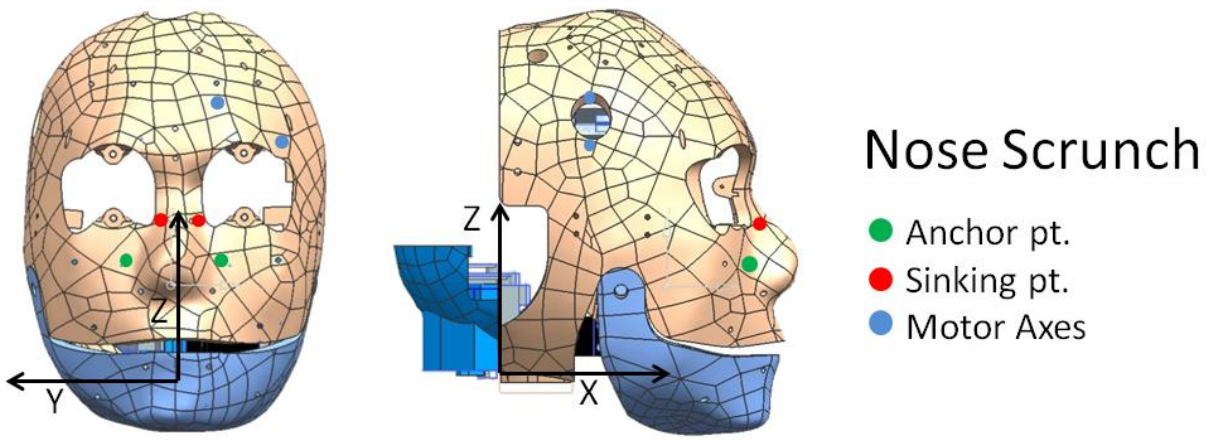

Figure 3.9: Coordinate system and example points used in GFEAD analysis.

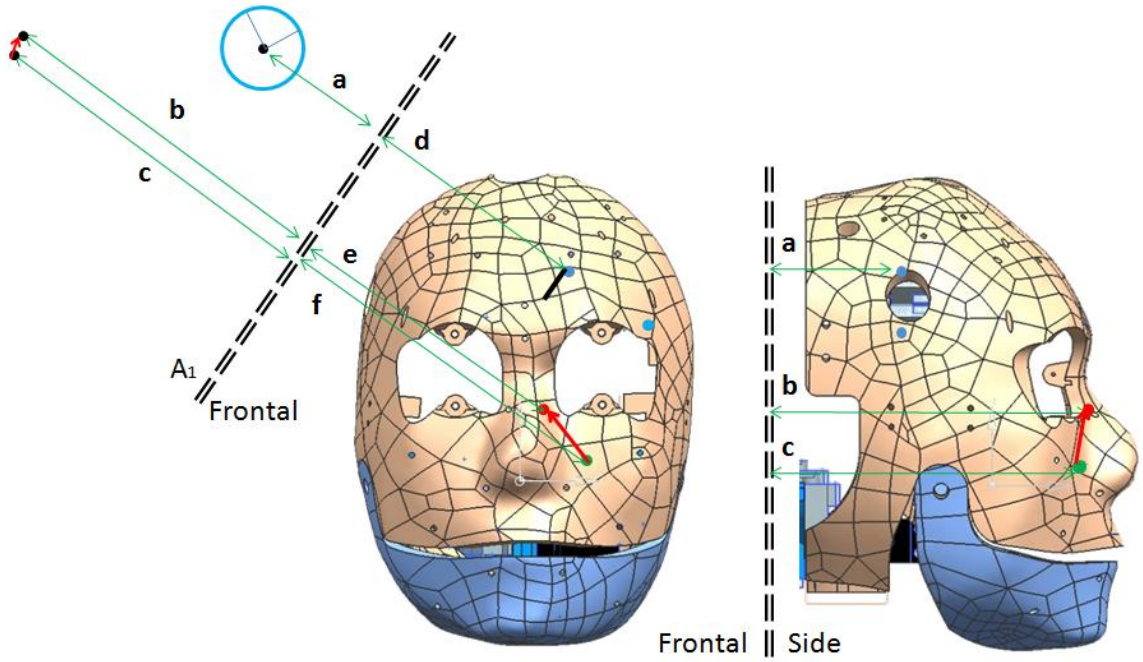

Figure 3.10: GFEAD analysis beginning with frontal and side plane views and first projection onto auxiliary plane 1. The black line in the frontal plane is the servo horn which appears as a line.

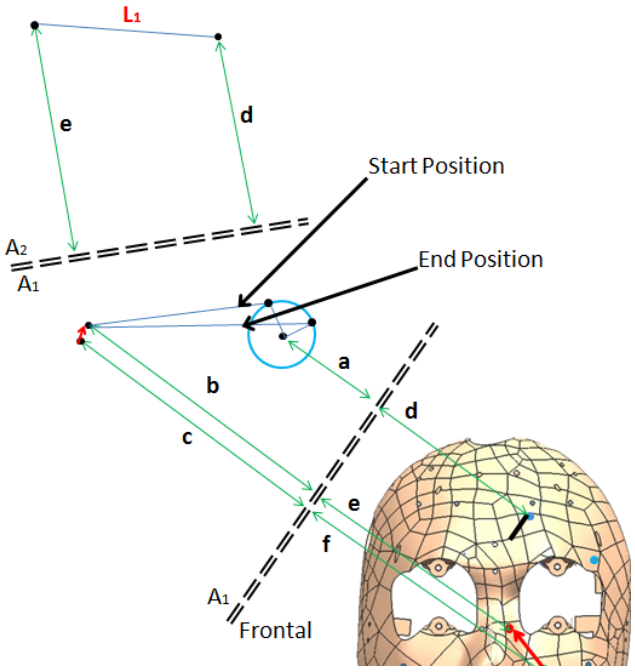

Figure 3.11: GFEAD analysis showing projection onto auxiliary plane two to find true length of wire at starting point of rotation.

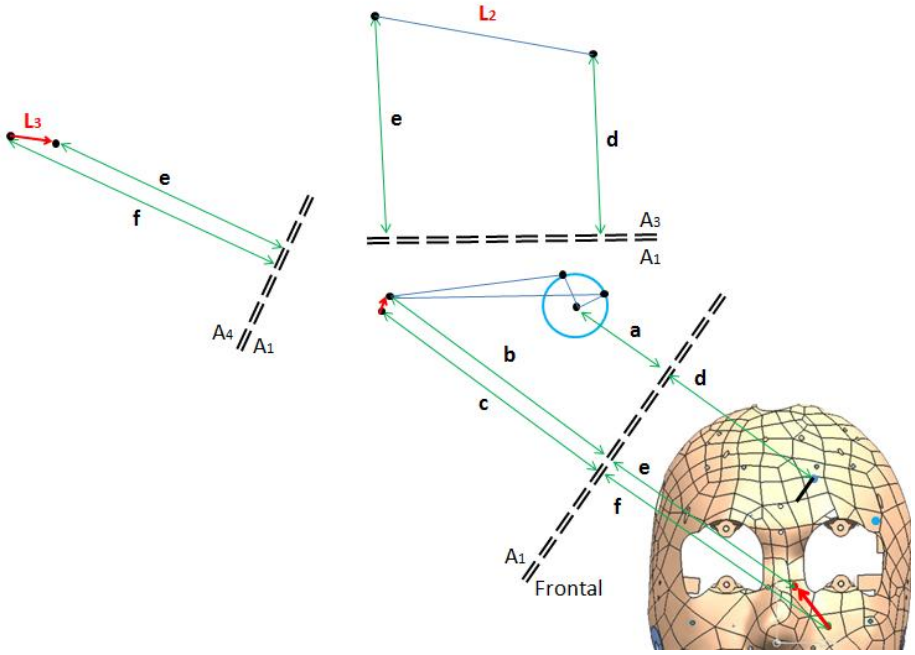

Figure 3.12: GFEAD analysis showing projection onto auxiliary plane 3 and 4 to determine true length of wire at ending point of rotation and available pull distance between anchor and sinking point.

This process is repeated for each arrangement of sinking and anchor points and the results are shown in figure 3.13. Since GFEAD measures anchor points and not the tracked points on the face, there will be discrepancies between the robots predicted (GFEAD) and measured capabilities. These discrepancies are due to the elasticity of our skin. For example, note the large difference between the predicted and measured values for the point "CR" which is on the right cheek. This point has moved the most by an anchor point located about 30mm away. This distance is large enough to create large amounts of strain between the anchor point and "CR" which is why the robot is capable of creating emotions in the first place. Other points like "ERM", "LRD", "LLD" and "LDM" show that the predicted and measured values are very similar. This is because the anchor points are directly under the points that were tracked thus the skin has very little room to stretch.

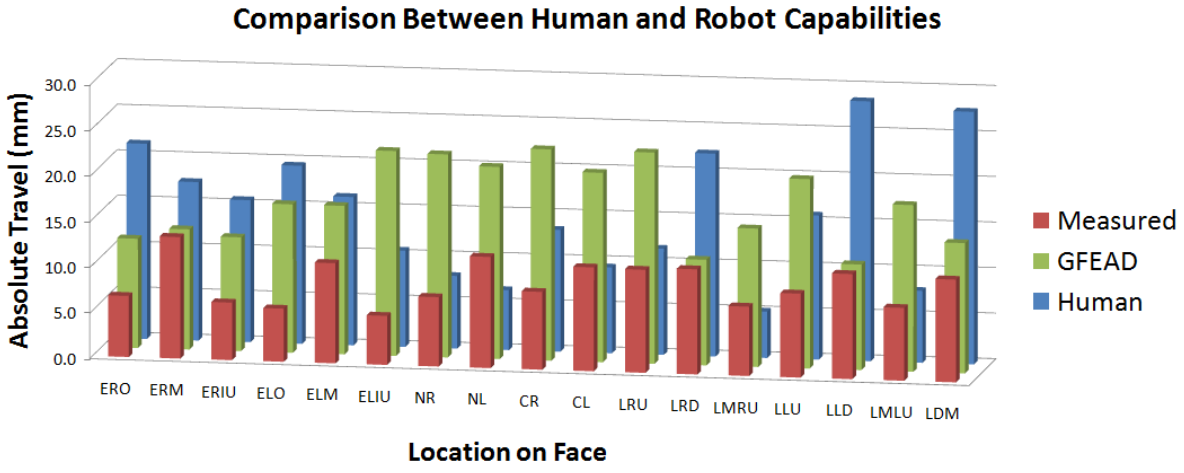

Figure 3.13: Comparison of measured travel of facial points between human and robot as well as predicted values from GFEAD.

The predicted absolute travel must be greater than the measured human capabilities in order for the robot to completely mimic human capabilities. Figure 3.13 shows that there is room for improvement where the predicted values are lower than human values. The two ways to make improvements are: a) to better orient the motors or b) to create more distance between the anchor point and sinking point. Points ELO, ELM, ERO, ERM, ELIU, NL, NR, CL, CR, LLD and LRD all have enough distance available between anchor and sinking points to accommodate for the maximum pull distance of the motor. The remaining points can be pulled more than the available

distance between anchor and sinking points which, if not carefully handled, could cause damage to the robot. Figure 3.14 shows the difference between available distance and maximum possible pull distance for each facial point. Positive values correspond to points where the motor should pull more while negative values correspond to anchor points that need to be farther away from their sinking points.

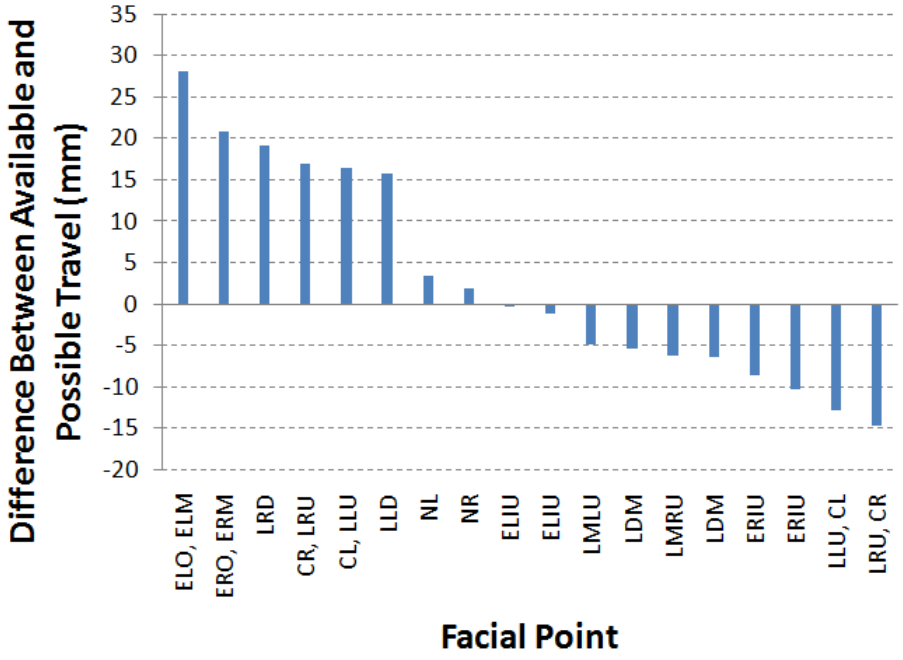

Figure 3.14: Graph of differences between available and possible travel amongst each facial point.

3.3.2 Facial Expression Recognition

In order for this robotic system to be useful in the field, it is imperative that the medical student does not confuse one facial expression for another. Therefore we conducted an experiment with 49 subjects where we asked them to identify the expression on the robot's face from a list of predefined expressions. The list includes several basic emotions/expressions of varying degrees and can be seen in Appendix A. The facial expressions are shown in order in figure 3.15 (1) – (7). We intended the facial expressions to be interpreted as happy, angry,

disgusted, surprised, suspicious, sarcastic and sad. The results from our 49 participants are shown in figure 3.16.

Figure 3.15: Facial expressions used in recognition experiment. 1) Happy, 2) Angry, 3) Disgusted, 4) Surprised, 5) Suspicious, 6) Sarcastic, 7) Sad.

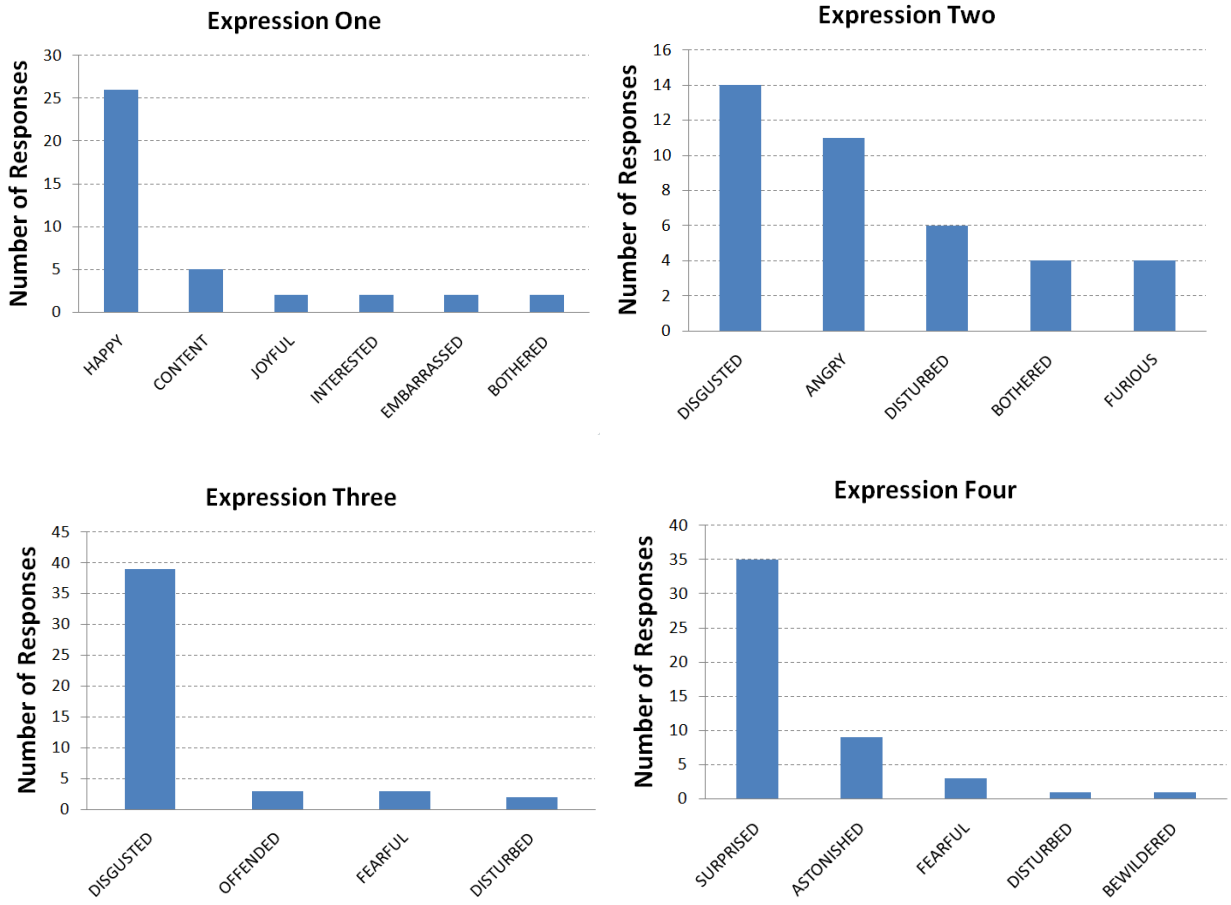

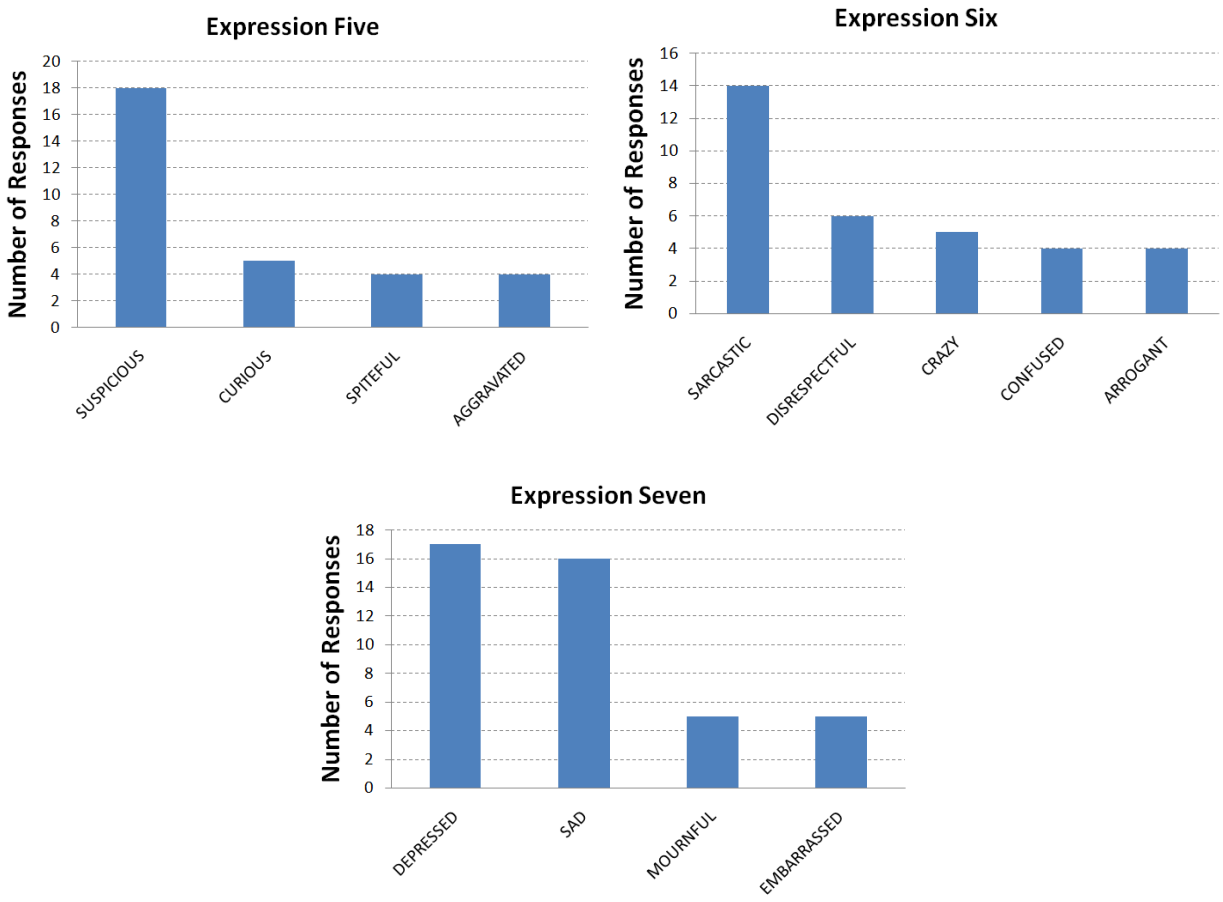

Figure 3.16: Results from the 49 participants of our expression recognition test. The top 4 results from each expression were shown (more if there was a tie).

We discovered several things while performing the test and analyzing the results. We realized that it is difficult to gauge a person's emotional state without any background of their personality. For instance, many people asked to see facial expressions one and two again because they claimed that after they have seen the other expressions they felt like they knew the robot better and could make a better judgment of its intended emotional expression. Several people also said that moving the neck back during "surprise" and forward during "suspicion" really helped with interpreting the expression. Others said it was too exaggerated, but necessary. We also noticed that many people confused anger with disgust. We believe that anger is a difficult emotion to display since it varies so greatly between different people and often requires additional information to identify such as posture or a knowledge of the events leading up to anger. "Sarcastic" was also a difficult emotion for participants to identify because it may require knowledge of the events leading up to the expression as well as an understanding of the robot's

sense of humor. Overall though, the participants were able to accurately identify each of the emotions.

3.4 Neck Design and Characterization

It has been found that the addition of an actuated neck in a humanoid robot increased a participant's willingness to indulge more personal information during conversation [54]. Since eliciting a more powerful emotional connection between student and simulator is our primary goal we decided to create a neck that mimics human capabilities. The human neck contains several vertebrae, each with 6 DOF. Replicating this anatomy would be unnecessarily difficult since the motion output of the head with respect to the upper body contains only translation and rotation about 3 axes and is depicted in figure 3.17. Several robotic necks appear in literature but rarely do they feature more than 2 or 3 DOF [5, 73, 74, 90] because, from a functional point of view, translation of the head is not necessary [5, 32].

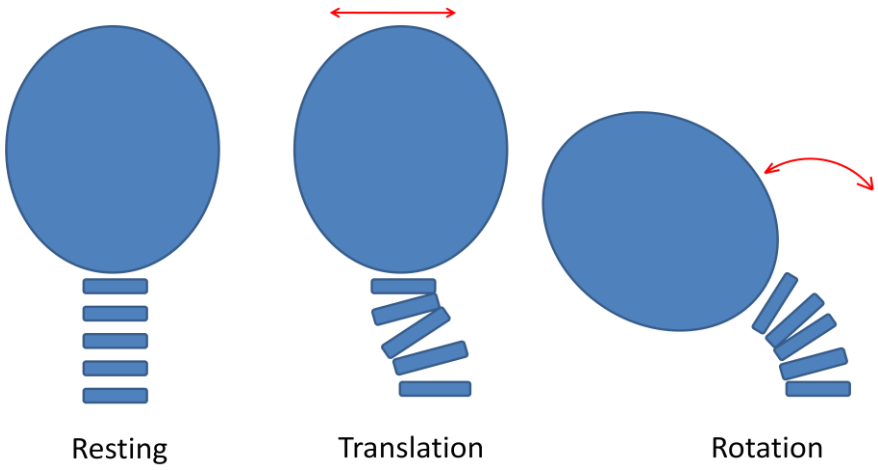

Figure 3.17: Diagram of vertebrae in human neck during translation and rotation.

Several designs were considered, each with their set of advantages and disadvantages. Serial mechanisms are convenient since they are simple to control, have large ranges of motion and can achieve high velocities. Parallel mechanisms are rigid and can withstand larger loads than serial mechanisms but their range of motion and speed are generally lower. It is important to recreate the full capabilities of the human neck due to subtle communication made through posture. If I were to open my eyes wide and lurch my neck forward someone could easily see

that as disbelief or interest whereas if I lurched my neck backwards I could be indicating surprise or uneasiness. We decided against a 6 DOF serial mechanism since the actuators required to support dynamic loads of the head would be too large to maintain human form.

The Stewart platform is a 6 DOF parallel mechanism with a closed chain kinematic structure and is commonly used in flight simulators, precision machining and surgical robots. We decided to design this type of mechanism for its positive attributes mentioned above as well as the information available in literature on its inverse kinematics and control schemes. Its range of motion and velocities are geometry dependent so we can tailor the dynamics to our specifications. [92] took statistical measurement of neck motion from a subject group and showed typical magnitudes of 44^o (standard deviation of $\sigma = 7.3^o$) for rolling, 69^o ($\sigma = 12^o$) for yawing, and 110^o for pitching with a maximum speed of 382^o/s ($\sigma = 72^o$/s). For our application it is more important to achieve human-like range of motion while being able to support a load of approximately 2.5 kg (the head) in any configuration. After an extensive search for small linear motors we decided to use the Firgelli L-12 actuators which can output 48N at 23mm/s. These linear motors can support a load of approximately 4kg while the Stewart platform is parallel with the floor at a diameter of 110mm (similar to that of a human). This reduced the speed to 28^o/s. A list of neck characteristics are shown in table 3.3.

Table 3.3: Comparison between human and robotic neck characteristics

Parameter	**Human (avg.)**	**Robot**
Height (mm)	160	195
Diameter (mm)	135	110
Yaw (deg.)	69	60
Roll (deg.)	44	60
Pitch (deg.)	110	60
Speed (deg./sec)	382	28

A typical Stewart platform (SP) has a top and bottom in the shape of triangles that are offset by 180 degrees. The linear actuators connect from corner of the bottom to a corner on the top. Due to the small size of the SP, the triangles were replaced by semi-symmetric triangles. This modification was made to provide more space to mount the actuators. To prevent the actuators from binding, universal joints were custom designed from 0.5mm thick sheet steel. The top plate had vertical holes for connecting to the head, and the bottom plate had horizontal holes for connecting to a chest. The final prototype is shown in figure 3.18.

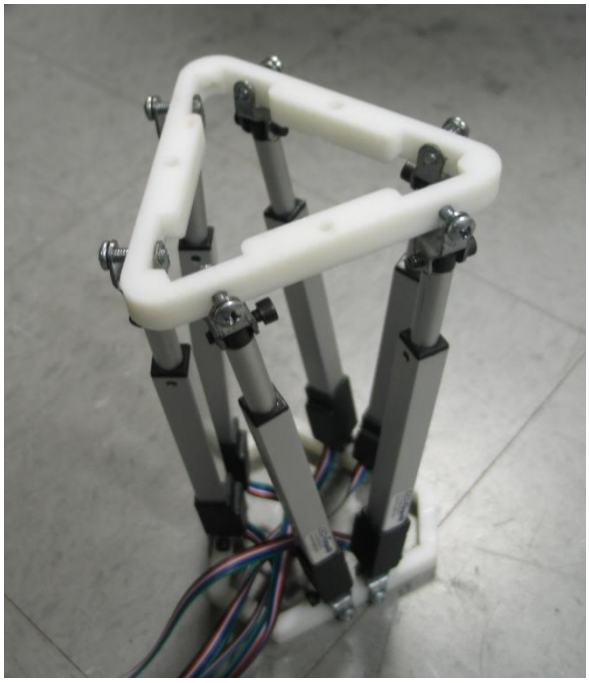

Figure 3.18: Photo of the Stewart-platform-based neck mechanism.

The inverse kinematic method, proposed by Liu, Fitzgerald, and Lewis [59] was used to develop equations that output actuator lengths based on orientation of the top plate. A modification was made due to the differences between the designs of the top plate: a triangle in Liu's design and a semi-symmetric hexagon in our design, as shown in figure 3.19. The geometry of the bottom (B) and top (T) of the platform was analyzed to find the locations of the six mounting locations. The actuators were attached from a point on the bottom designated by 'B#' to a point on the top designated by 'T#'.

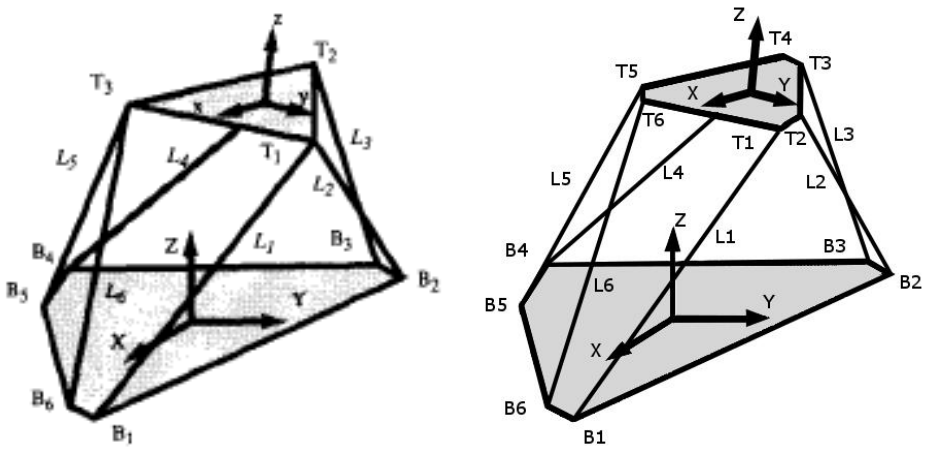

Figure 3.19: Differences between Liu design (left) and ours (right).

The distance along the long side of the hexagon was designated ‘a’ and ‘b’ in the diagrams of the top and bottom, respectively. The length of the smaller side was designated as ‘c’ and ‘d’ in the diagrams of the top and bottom, respectively, as shown in figure 3.20. Since coordinates are relative to a local reference frame, the location of points in the z-direction was zero for the top and bottom plates. A summary of the coordinates are listed in table 3.4, where $Q = {\sqrt{3}}/{6}$ for simplicity.

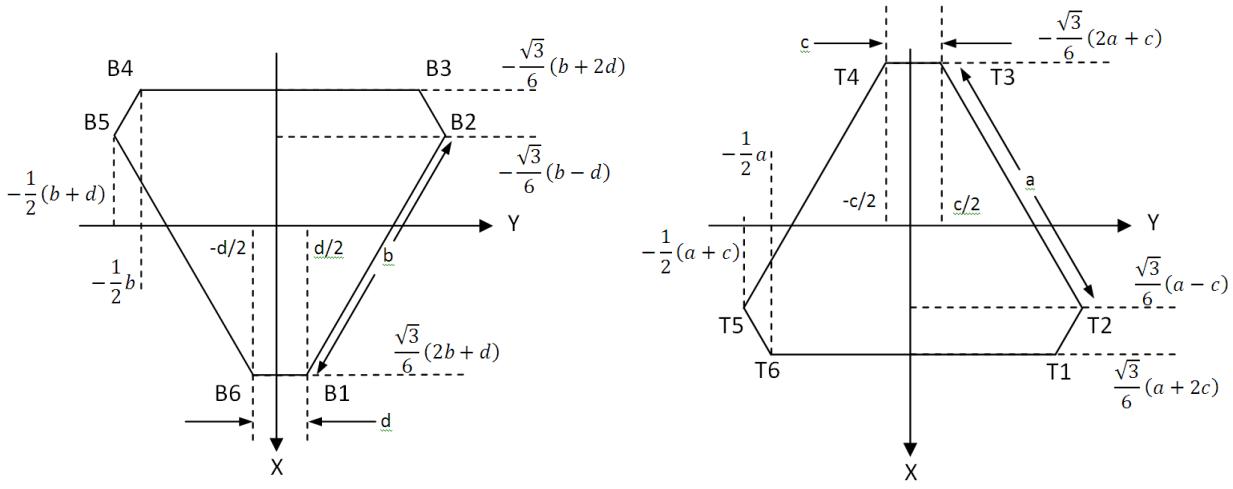

Figure 3.20: Geometric diagram of base (left) and top (right) plates of the Stewart platform.

Table 3.4: Coordinates of attachment points for bottom (B) and top (T) plates.

	X	Y	Z
B1	$Q*(2*b+d)$	$d/2$	0
B2	$-Q*(b-d)$	$0.5*(b+d)$	0
B3	$-Q*(b+2*d)$	$b/2$	0
B4	$-Q*(b+2*d)$	$-b/2$	0
B5	$-Q*(b-d)$	$-0.5*(b+d)$	0
B6	$Q*(2*b+d)$	$-d/2$	0
T1	$Q*(a+2*c)$	$a/2$	0
T2	$Q*(a-c)$	$0.5*(a+c)$	0
T3	$-Q*(2*a+c)$	$c/2$	0
T4	$-Q*(2*a+c)$	$-c/2$	0
T5	$Q*(a-c)$	$-0.5*(a+c)$	0
T6	$Q*(a+2*c)$	$-a/2$	0

The Denavit-Hartenburg method uses a set of transformation matrices to relate one reference frame to a global reference frame. The matrix below represents the 6-axis transformation between the two coordinate systems. Details about this transformation can be seen in [86].

$$T=\begin{bmatrix} cb*cz+sa*sb*sz & cz*sa*sb-cb*sz & ca*sb & x_T \\ ca*sz & ca*cz & -sa & y_T \\ cb*sa*sz-cz*sb & sb*sz+cb*cz*sa & ca*cb & z_T \\ 0 & 0 & 0 & 1 \end{bmatrix} \quad [3.1]$$

Where cb = cos(b), sa = sin(a) etc. The coordinates of the top plate were combined into a matrix C_T, which was then multiplied by the total transformation matrix, T, to find a matrix T_f containing equations for the location of the mounting points of the top plate with respect to the bottom plate. A list of the equations is provided in Appendix B.

$$C_T = \begin{bmatrix} x_{T1} & \dots & x_{T6} \\ y_{T1} & \dots & y_{T6} \\ z_{T1} & \dots & z_{T6} \\ 1 & \dots & 1 \end{bmatrix} \quad [3.2]$$

$$T_f = T * C_T \quad [3.3]$$

Once the locations of the top attachment points are known with respect to the desired translational and rotational inputs, actuator lengths could be found by applying the distance formulation as shown below:.

$$L1 = \sqrt{(X_{T1} - X_{B1})\text{^}2 + (Y_{T1} - Y_{B1})\text{^}2 + (Z_{T1} - Z_{B1})\text{^}2} \quad [3.4]$$

$$L2 = \sqrt{(X_{T2} - X_{B2})\text{^}2 + (Y_{T2} - Y_{B2})\text{^}2 + (Z_{T2} - Z_{B2})\text{^}2} \quad [3.5]$$

$$L3 = \sqrt{(X_{T3} - X_{B3})\text{^}2 + (Y_{T3} - Y_{B3})\text{^}2 + (Z_{T3} - Z_{B3})\text{^}2} \quad [3.6]$$

$$L4 = \sqrt{(X_{T4} - X_{B4})\text{^}2 + (Y_{T4} - Y_{B4})\text{^}2 + (Z_{T4} - Z_{B4})\text{^}2} \quad [3.7]$$

$$L5 = \sqrt{(X_{T5} - X_{B5})\text{^}2 + (Y_{T5} - Y_{B5})\text{^}2 + (Z_{T5} - Z_{B5})\text{^}2} \quad [3.8]$$

$$L6 = \sqrt{(X_{T6} - X_{B6})\text{^}2 + (Y_{T6} - Y_{B6})\text{^}2 + (Z_{T6} - Z_{B6})\text{^}2} \quad [3.9]$$

These equations were entered into Labview 2010 and converted into servo commands which were sent to a Pololu Mini-Maestro 12 servo controller via USB. The graphs in figure 3.21 3.22 and 3.23 show that the algorithm works by comparing the desired input to the actual output for all six degrees of freedom. For angles less than 30 degrees, the Stewart platform does an excellent job following the inputs to the algorithm. Deviations after 30 degrees are probably attributed to poor tolerances in the Firgelli actuators. As larger angles and translations are being performed, there are larger stresses on the actuators due to the nature of the Stewart platform, which also lends to its precision. This added stress causes the shaft of the motor to displace as

much as 5 mm which causes the error seen in the graphs. Future designs will incorporate higher tolerance motors to eliminate such effects.

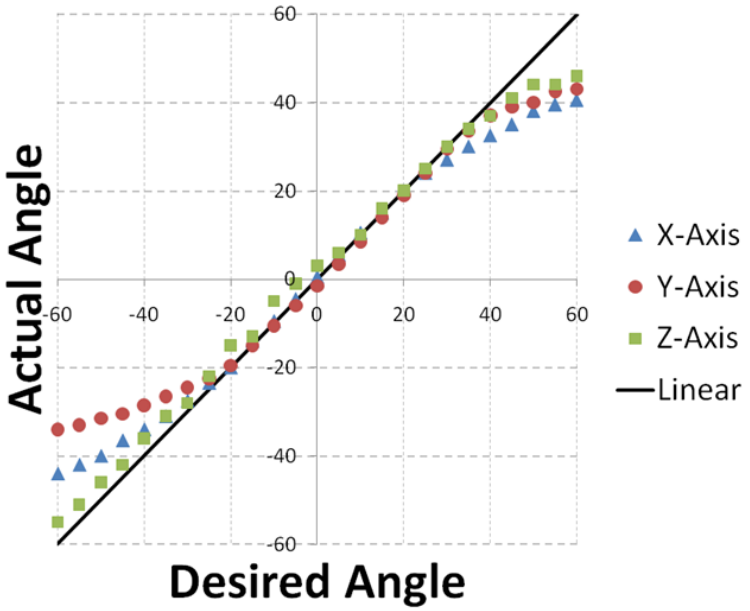

Figure 3.21: Comparison of actual to desired angles of the neck mechanism.

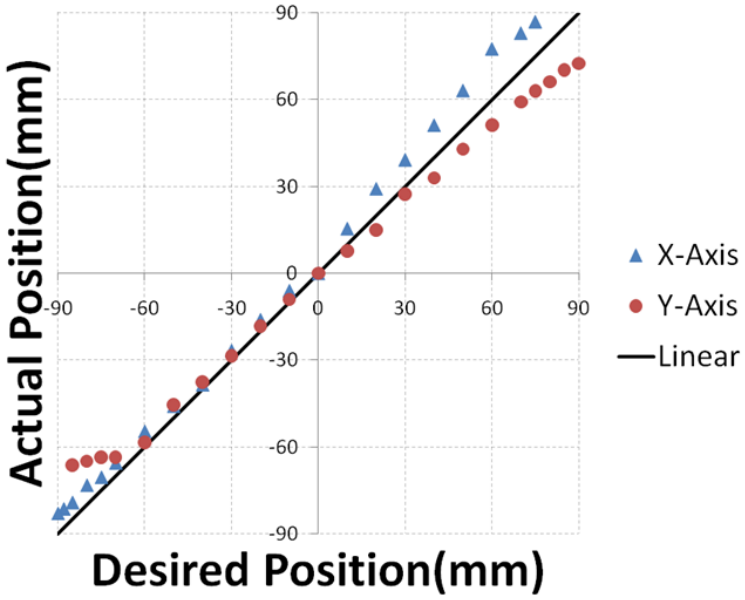

Figure 3.22: Comparison of actual to desired translational positions of x and y axes of the neck mechanism.

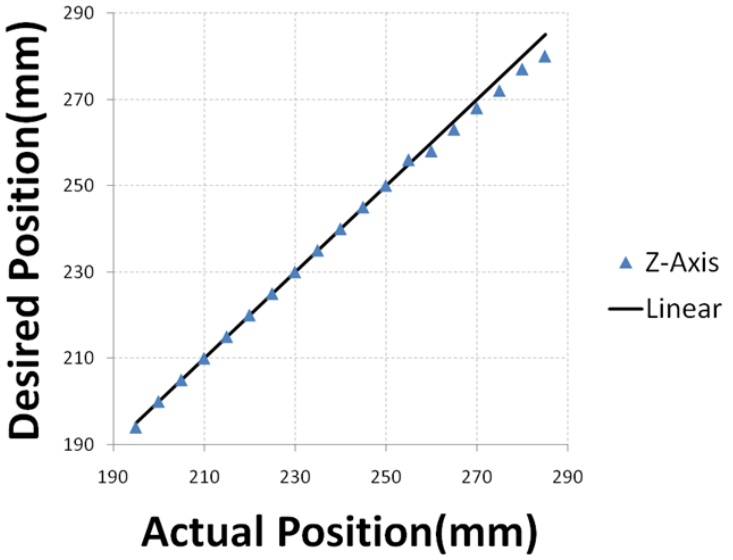

Figure 3.23: Comparison of actual to desired positions of z axis of the neck mechanism.

Chapter 4

Full Body Humanoid Medical Simulator

4.1 Full Body Integration

4.1.1 Torso

The last phase of the project involves taking each component of the humanoid and integrating them into a fully body medical mannequin. The components of the humanoid that will be covered in this chapter are:

- Lower torso
- Legs
- Mobile test bed
- Various sensors and programming

All commercial medical mannequins (described in Chapter 1) lack the ability to sit up and maintain their posture. We felt this was something important to include in the full body design because it allows the mannequin to be either unconscious (laying down) or conscious (sitting up). This is especially important during the screening interview where the doctor and patient have to socially engage with each other. In order to accomplish this, we designed a two degree of freedom platform that allows the upper body to swivel up and down like the patient is doing a sit-up as well rotate so the robot can hang its legs over the side of the bed. A photo of the mechanism can be seen in figure 4.1.

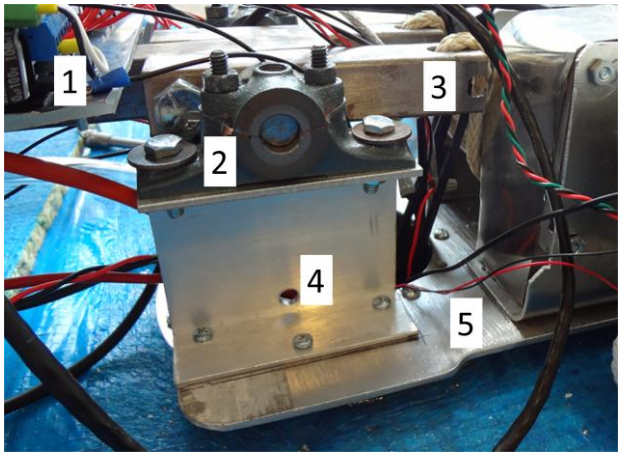

Figure 4.1: Photo of mannequin torso with 2 DOF. 1) Chest/upper body, 2) mounted bearings that provide 1 DOF for sitting up, 3) lower end of upper body that locks into place, 4) Hole through the lower mount to insert a locking pin to maintain posture, and 5) platform where torso and legs connect to the bed which can rotate for the second DOF.

The platform was bolted to a 4 inch ID rotational bearing which was firmly mounted to the test bed. Having a rotational bearing with an open center is very important because we will have a large number of wires originating from components like power supplies, the computer and data acquisition modules that need to pass through the top side of the bed to reach the humanoid. Since we are trying to make this simulator as realistic as possible, an inconspicuous location to hide the wires is vital.

4.1.2 Legs

On the other end of the rotating platform is an L-shaped mount for stepper motors to control a single degree of freedom at the hips. This hip will be the mounting location for the rest of the leg. The design requirements for the legs are fairly minimal, especially since they are not required to walk. This allows us to greatly simplify the design, reduce weight and cost and gives us extra room to mount sensors and other medical components. After speaking with our contact at Carilion Hospital, we were able to identify three areas that the legs could contribute to:

- Combative patient
- Drug delivery
- Physical examinations

When the combative patient enters the hospital they may be flailing their arms and legs so it's important to drive each joint. In order to keep weight down, a single degree of freedom joint was incorporated to the hips, knee and ankle. In reality the hip has 3 DOF, the knee has 1, and the ankle has 3 DOF, but the combative patient can easily be simulated with 1 DOF per joint. Since for an average person the legs are 3 feet long, a small increase of weight will result in a significant increase of the moment at the hip. In order to overcome this problem, we decided to fabricate the legs with carbon fiber rods and Styrofoam. The leg components can be seen in figure 4.2.

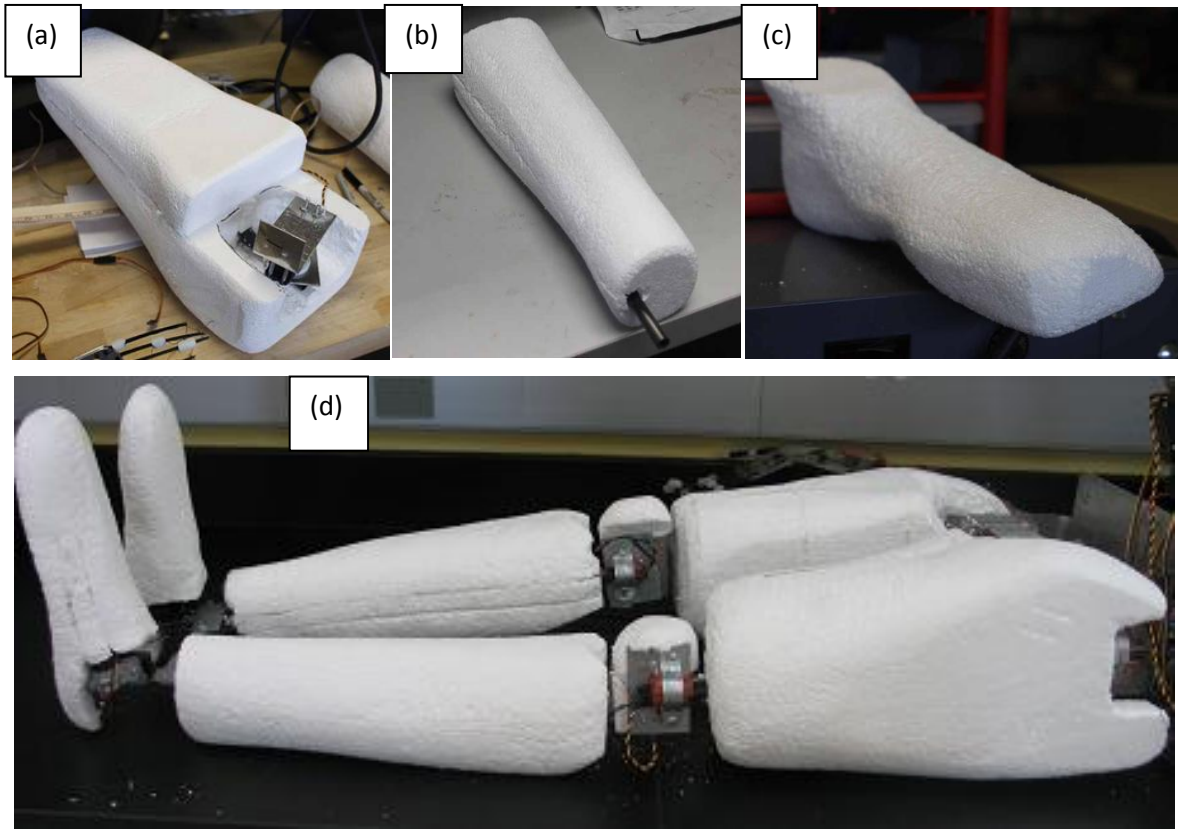

Figure 4.2: Styrofoam components of the leg design. (a) Thigh, (b) shin, (c) foot. The completed assembly is also shown in the figure (d).

Each joint connects the carbon fiber rods with plates and a servo motor. The servo was mounted to the shaft of the upper portion of the leg and the lower portion of the leg was attached to the horn of the motor as shown in figure 4.3.

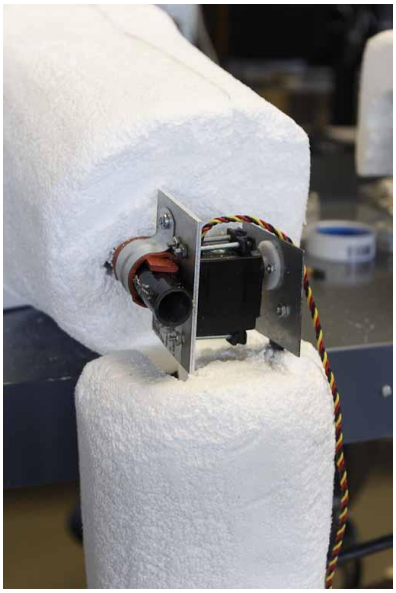

Figure 4.3: Photo of the joint assembly for the legs.

The weight of each component does not exceed 2 lbs and thus small hobby motors were appropriately sized and used except for the hip. After performing a force balance at the hip, we purchased a 34K104S series stepper motor from Anaheim Automation [97] which can handle the load with a safety factor greater than 2.

4.1.3 Mobile Test Bed

In order for robot to be moved easily from one location to the next, a custom bed had to be designed. When the robot was completely assembled, it would stand 78 inches tall and 23 inches wide so the bed was designed to be 84 inches by 24 inches. The bed also needs to be high enough to store all of our power supplies and computing components. Below is a list of all of the components that will be incorporated in the bed of the humanoid medical simulator.

- Power supply for stepper motors
- Power supply for stepper motor controllers
- Power supply for hands and other sensors
- Power supply for face, neck and leg servo motors
- Power supply for linear actuators in arms
- Data acquisition card for sensors

- 2 4-port powered USB hubs
- Desktop computer tower
- Computer monitor

The tallest component in the list is the computer tower (18 inches) so the bed was designed to be 24 inches tall. The frame of the bed was made from pine 2 x 4s. The top and bottom were covered with ¾" plywood and the area where the torso attaches to the bed was reinforced with 2 x 4 cross beams. Four caster-type wheels were attached at each corner which allowed the bed to smoothly roll in any direction and can also be locked to prevent motion. A pullout drawer was built-in to house a monitor which will be used as a vital sign readout. A photo of the test bed is shown in figure 4.4.

Figure 4.4: Photo of the custom built test bed used to house components and transport the simulator.

4.2 Sensor Systems

Sensors facilitate the interaction between the simulator and the medical student by automating the responses of the simulator without the intervention of a human operator. The next several sections will discuss the capability of each of the sensory systems.

4.2.1 Drug Delivery

One of the most important skills that a nurse or doctor can develop is knowledge of available drugs and when to use them. When a crashing patient is rushed into the emergency room, the right drug often makes the difference between life and death. Drug delivery is practiced through several different methods based upon the complexity of the medical mannequin. Some mannequins simply have tubes that run off into a bucket while others have circulating fluids that pick upon the type of drug that was delivered and react accordingly. A more economical approach is drug pouches which are simply hollow pockets of air encased in rubbery plastic and capable of being injected with fluids from a syringe. Several mannequins have barcode readers that scan the bars on a syringe and simulate what a person would do if the drug was administered. This type of method focuses more on administering the correct drug rather than the physical process of delivering the drug. Our collaborators at Carilion Clinic indicated that this was the type of method they wanted to improve upon in this mannequin. Barcode readers are difficult to work with because one has to line up the bar code with the reader. We began investigating the use of radio frequency identification, or RFID tags. RFID works by having a reader/transceiver send out a short-range radio signal. The chip, or tag, uses the radio signal as an energy source to send out its information. This information is then read by the transceiver and can be used to conduct an operation. Having a drug delivery system based on RFID would be a great improvement to the barcode systems used in current systems.

The reader and breakout board we used for this system were the SEN-08419 and SEN-09963 respectively from Sparkfun Electronics. This reader was ideal because of its small size (1” x 1”) and USB output. The RFID tags used were the SEN-09416 and were chosen because of their small size. The tag was a small glass tube and was ideal because it can easily fit within a small syringe which helps in increasing the realism of the drug delivery. The two spots on the humanoid that our collaborators at Carilion Clinic have determined these RFID readers could be used are the inside of the elbow and the thigh. The elbow is a standard location for drug delivery but if there is a combative patient then this location is difficult to utilize and in that case the doctors will inject drugs into a large muscle like the thigh. Pictures of the RFID reader and tags in the humanoid are shown in figure 4.5.

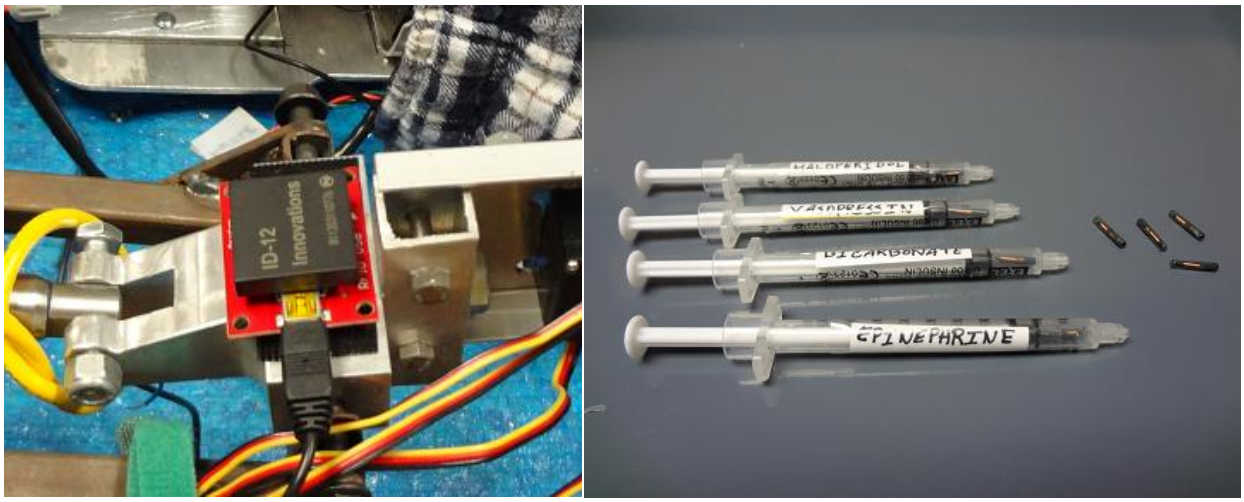

Figure 4.5: (Left) RFID reader and (right) syringes with small glass RFID tags

The important signs that must be monitored for emergency room situations are blood pressure (BP), heart rate (HR) and respiratory rate (RR). Since, in our system, these readings are simulated and not measured they are easy to manipulate. Using Labview 2010, a graph was constantly updated with an artificial EKG signal. Respiratory rate, systolic and diastolic blood pressure were also displayed as numbers as shown in figure 4.6.

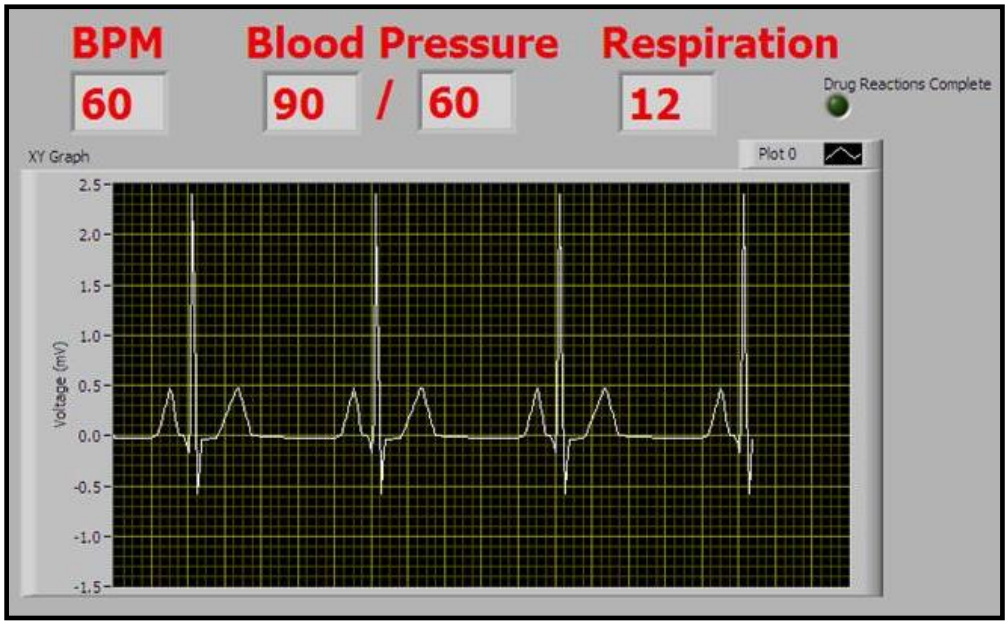

Figure 4.6: Front panel view of Labview program for drug delivery and vital sign readout.

If the simulator is now instructed to enter cardiac arrest then blood pressure would drop and heart rate and respiratory rate would flat-line. The robot now waits for bicarbonate, which is a drug commonly used curing cardiac arrest to increase HR, BP and RR. If the robot does not receive bicarbonate in the appropriate time frame then it will not react to any more drugs, simulating death. Below is a list of commonly used drugs, their corresponding effects and conditions of use.

- **Epinephrine** – Increases HR, BP and RR. Administered if face swells or if there is difficulty breathing or dropping blood pressure.
- **Vasopressin** – Increases BP and decreases water loss through urine. Administered if BP is low
- **Bicarbonate** – Increases HR, BP and RR. Administered during cardiac arrest.
- **Haloperidol** – Anti-psychotic which is used as a tranquilizer.

The program can be adjusted to accommodate as many drugs as the surgeon needs to deliver. The rates at which the drugs are injected are also adjustable and it helps the doctors because they can get immediate feedback.

4.2.2 CPR Sensor

Cardio pulmonary resuscitation, or CPR helps to keep blood and oxygen flowing after the heart and lungs have stopped. There are over 220,000 reported sudden cardiac arrest deaths per year [18] and CPR and defibrillation within the first few minutes can significantly increase ones chances of survival. There are several dedicated mannequins that aid CPR training but are usually limited in their function. Many advanced medical mannequins today do not have this feature due to the amount of components below the chest.

We used a custom fabricated pressure sensor to measure the force being applied during CPR. The sensor was built out of two layers of copper mesh which are separated by 6mm of conductive foam. The upper and lower meshes were connected to the positive and negative leads, respectively, of a 5 Volt power supply. When the conductive foam was compressed the copper meshes come closer to each other, thus allowing more electricity to flow through the conductive

foam. If we put a resistor in parallel with the current we can measure the change in voltage with respect to pressure. The sensitivity of the sensor is inversely related to the value of the resistor.

The magnitude of force used during CPR lies in the vicinity of 100 lbs [96]. Applying more force increases the chance of survival but also increases the chance of breaking ribs. We measured voltage by using the 9215 DAQ module while applying approximately 100 lbs and setting the corresponding voltage as a threshold for an LED indicator on the front panel. If the student applies enough pressure to the chest then they will get a green light. In order to make the chest feel more realistic during CPR, we overlaid the sensor with a 20mm thick layer of silicone as shown in figure 4.7.

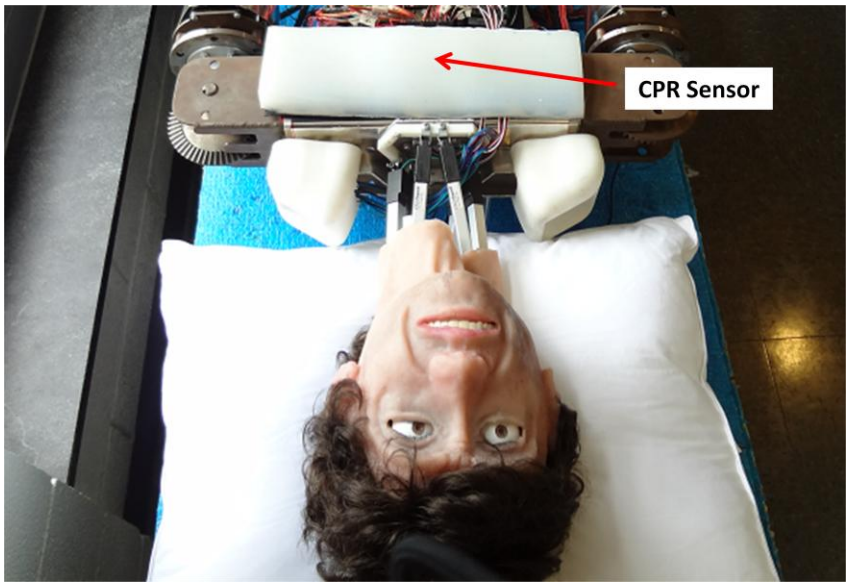

Figure 4.7: Photo of CPR pressure sensor embedded underneath a 20mm thick layer of silicone.

4.2.3 Patellar Reflex Sensor

Part of the physical exam as described by [8] is to test the deep tendon reflexes. The doctor will briskly strike a deep tendon and watch for an extensive or reflexive response. Diminished levels of reflex could indicate diseases of spinal nerve roots, spinal nerves, plexuses, or peripheral nerves. We simulated this in our robot's knee by embedding a piezoelectric sensor where the tendon would normally be found. A photo is shown below in figure 4.8.

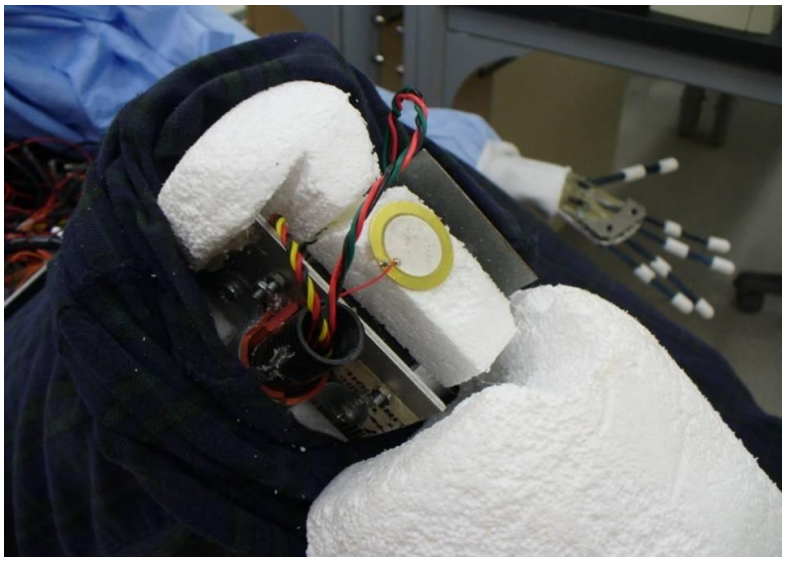

Figure 4.8: Photo of piezoelectric sensor embedded on the knee to simulate the patellar reflex.

The methodology is fairly straightforward: if the sensor reads a value higher than a certain threshold then the motor at the knee will “kick” and “return”. The difficulty arises with sampling rate since the knee strike was so sudden. The program that was created was so large that sometimes it would not run fast enough to detect the brief voltage spike. This was corrected by changing the control methodology of the entire program and will be discussed in the following sections.

4.3 Testing with Carilion Clinic

The final stage of the project was to bring the robotic medical simulator to Carilion Clinic in Roanoke VA and have several faculty members test its capabilities and give us their feedback. Gerald Beltran D.O., Sonya Echols (director of the Center for Experimental Learning at Carilion Clinic), Ashley Miear (Educational Specialist) and Misty Flinchum (Educational Specialist) all attended the demonstration.

4.3.1 Control Interface

The first step was to sit down and show the medical staff how to run the robot from Labview 2010. This was extremely important because certain doctors may want more control over the simulation. For instance, if the examiner wants to suddenly drop blood pressure or have

the simulator seize then the system needs to react quickly to sudden changes in operating modes. Some examiners prefer to hit the "go" button and let the state of the patient play out based on how the medical students treat it. Currently in our program, the examiner must make the changes themselves but automating the patient-state would be a feature that can be included in future programs. Figure 4.9 below shows the front panel of the program we used to control the robot.

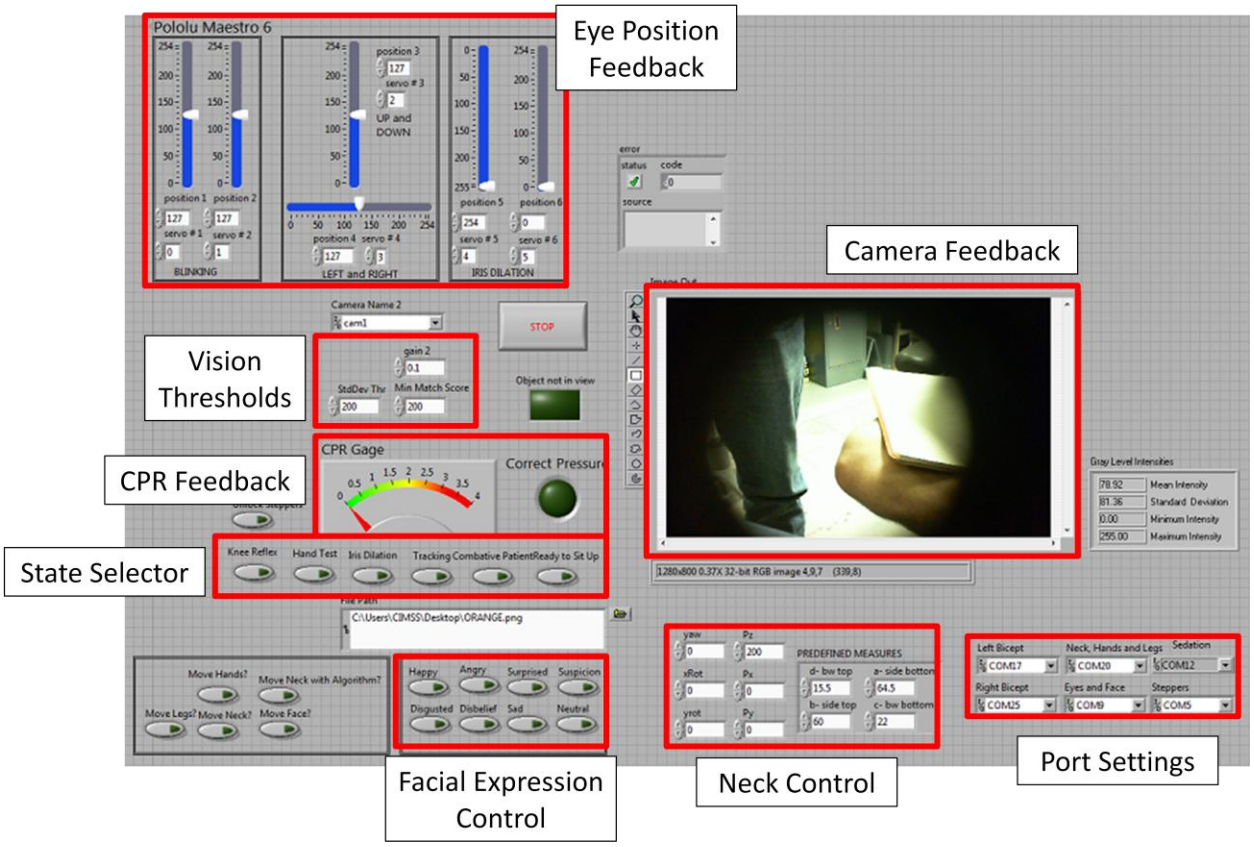

Figure 4.9: Front panel of Labview VI which controls the medical mannequin during operation.

The important features are highlighted with a red box to help visualize the interface. Vision thresholds and port settings are areas that need to be specified before the program is run. Port settings specify which USB port each component is hooked up to on the main computer. Vision thresholds, as previously mentioned, control when the eyes dilate or how sensitive the vision tracking is to a particular template and how quickly to move the eyes to track the object. Eye position feedback simply shows the motor position during motion; this is more to help us troubleshoot the eyes during programming. CPR feedback shows a gauge of how much pressure is being experienced at the sensor. If the correct amount of pressure is applied then the "Correct

Pressure" LED will light up. Camera feedback displays on the front panel show the images captured by the eyes. During tracking, it also shows the region of interest which is the spot on the image that best matches the template as long as it's above the threshold. Neck control is simply where user inputs the values for translation and rotation of the neck. Facial expression control is an array of buttons with pre-recorded facial motor positions which correspond to certain facial expressions. Currently the face is programmed to display happy, sad, angry, disgusted, surprised, sarcastic, suspicious and neutral emotions but can be programmed to make any other expression.

The most important area on the front panel is the state selector area. These buttons are pressed when the user is going from one operating mode to the other, i.e. combative patient to vision tracking. Since the code is so large and Labview is intended to be a development tool, running every feature at once would slow the computer down and cause errors. To counteract this we developed a state-selector architecture where once we select an operation mode, like combative patient, only the features that need to run are turned on. Figure 4.10 shows a screenshot of our block-diagram in Labview.

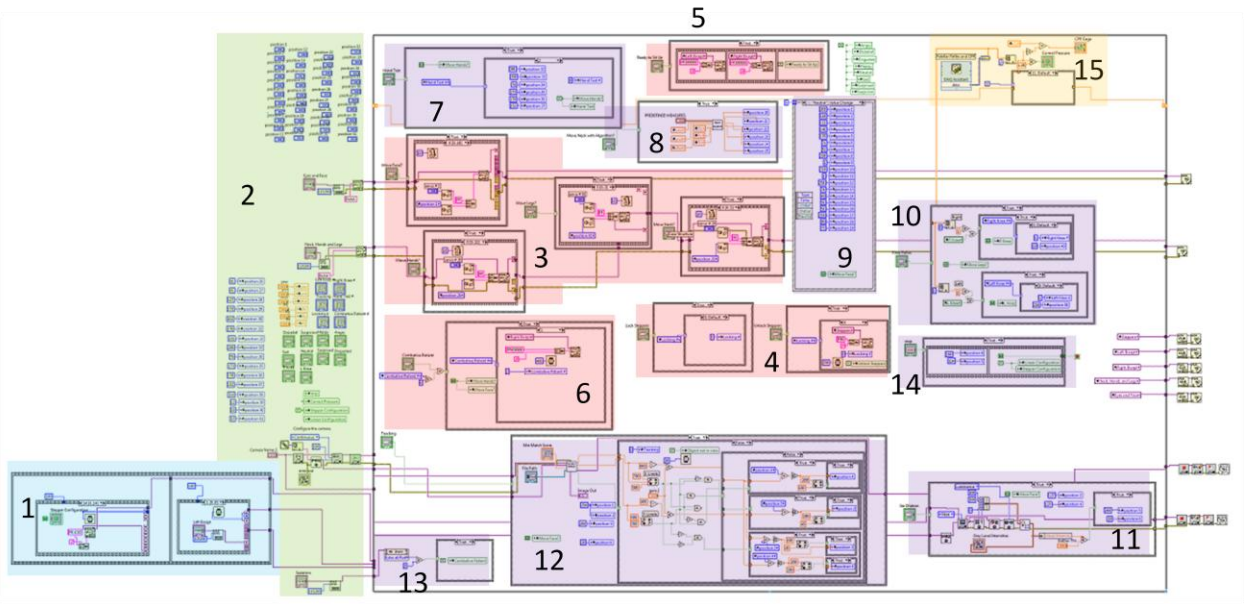

Figure 4.10: Screenshot of the block diagram which controls the whole medical mannequin.

The code runs in a while loop which will continue until the examiner hits the "Stop" button. In figure 4.10 the blue area shows where the Anaheim stepper motors and linear

actuators are given velocity, acceleration and deceleration commands so that they run smoothly. The green area is where local variables, command buttons and communication ports are initialized. After that the program enters its main loop it makes use of local variables that represent the positions of motors. Instead of sending a motor command after computation, the values of local variables are changed. After that iteration of the main loop, case structures that send commands to motors are made true and all of the local variables that were changed are now sent to their respective motors. This type of architecture allows us to separate the program into a computation stage and a command issuing stage. The pink areas in figure 4.10 show where local variables are issued as motor commands and purple areas represent areas where computation is performed. The exact breakdown of the structure is outlined below:

1) Set velocities, accelerations and decelerations to stepper motors and linear actuators
2) Initialize local variables, command buttons and communication ports
3) Sequence structures that send commands to specific servo motors (i.e., face, hands, leg)
4) Sequence structures that allow the stepper motors to be "locked" or "unlocked"
5) Sequence structure that puts the arms in a position for the mannequin to sit up
6) Sequence structure that runs continuous combative patient mode by sending commands to stepper motors.
7) Changes local variable values for the hand to grip, as if it were shaking someone's hand
8) Computes the values for the neck motors based on user inputs and changes local variable values
9) Event structure wired to facial expression buttons. When an expression button is pressed, all of the local variables for that expression are changed.
10) Changes local variable values of knee motor after the patellar reflex sensor reads a high voltage
11) Changes local variables for the eyelids and dilation motors based on the intensity of light seen in the current image (Iris dilation).
12) Changes local variables for eye motion based on the location of the best match to a template in the current image (Vision tracking).
13) Detects if there is a reading at the RFID reader in the leg. If there is, then it turns combative patient mode to "False".

14) When the stop button is pressed the eyelids and iris dilation local variables are changed to a relaxed state.
15) Area where data acquisition is performed to measure the pressure sensor and patellar reflex sensor. Patellar reflex mode can be turned off but CPR sensing is always on.

An overall flow diagram of the program is shown in figure 4.11 while Appendix C shows a more detailed breakdown of each state.

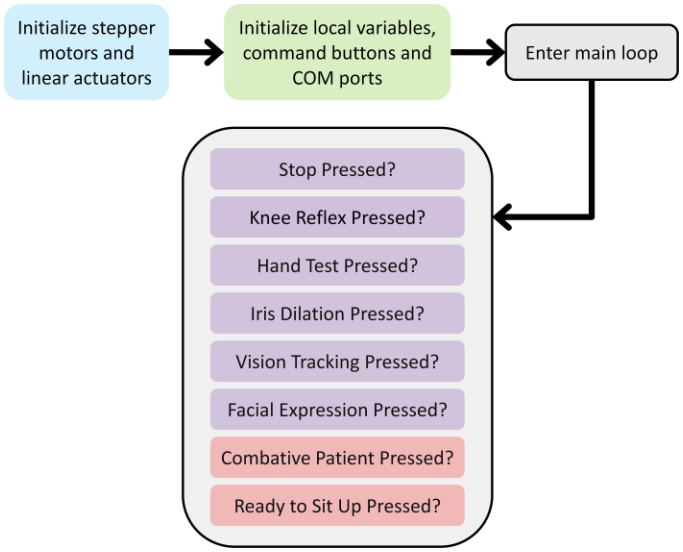

Figure 4.11: Overall flow diagram of how the program performs.

Our collaborators at Carilion said that they "liked how the interface could be controlled all from one screen." Other interfaces have drop down menus and tabs that take time to navigate but this interface is simple. The only drawback is that this program is very simple compared to some of the more advanced medical mannequins. As more features are added to the robot more effort will have to be spent to ensure that the front panel is still simple to use.

4.3.2 Combative Patient

During combative patient mode there is a series of 23 motor commands that are sent to the legs, arms and hands that move the robot in a way that resembles someone flailing on a bed. We were unsure of how close the doctors would be to the mannequin so we made sure it did not swing to the extremes. All of the collaborators at Carillion appreciated the simulation and said it

was a step in the right direction. A few things they mentioned that would help improve the combative mode would be:

- Less motor noise
- More leg kicking
- More yelling and screaming

Dr. Sonya Ranson also mentioned, “So he’s doing all the motions, so the first thing we’re going to do is try to hold him down. So could you have him react to being restrained? Could you stop the movement of a restrained limb?” Currently the robot is incapable of being restrained, combative patient mode is ended by artificial administration of Haloperidol which is commonly used as a sedative. Future prototypes will have to include a mechanism for restraining the full body without causing harm to the medical students. This could be achieved by using strain gauges at major stress points in the shoulder, elbow, forearm, wrist and leg segments. When the gauge experiences a strain outside of normal operating strains then the limb would move into a position that returns it to normal operating levels. The rate and force thresholds of each limb can be tuned by using some form of PID control. Another method would be to line the outside of the mechanical structure with a skin with embedded pressure sensors. When the pressure sensors read a change in voltage then the robot knows it has either run into something or it is being restrained and attempts to return the voltage to normal levels. The limb would be moved in one direction then the sensor value would be read again. If the voltage has gotten closer to normal then continue moving in that direction, if not then try another direction.

4.3.3 Triage

Another important area the mannequin can be used is in Triage or the initial assessment of the state of a patient. Many hospitals call this the “Interview Stage” where the patient sits down and answers questions about medical and family history. For this mode we have the robot sit up and lock into the upright position. The upper body is then turned 90 degrees so that the legs hang over the edge of the bed as shown in figure 4.12.

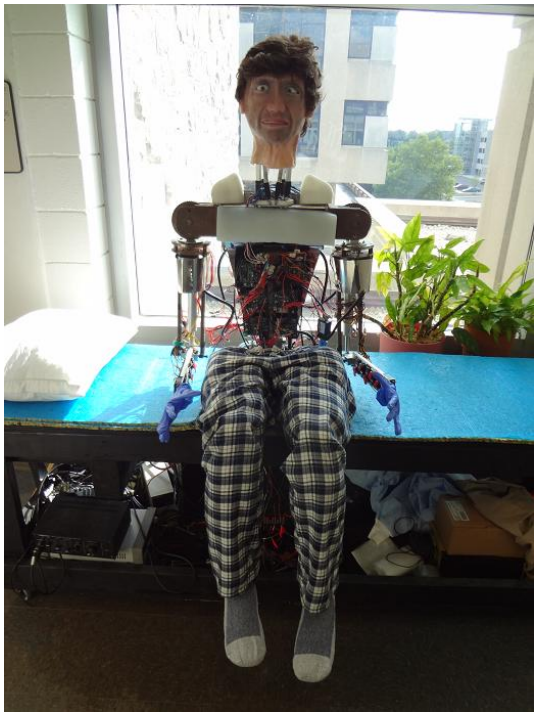

Figure 4.12: Medical mannequin in the upright position which is used during the interview stage.

There is a microphone that drives a compression speaker located within the bed. A long tube runs from the speaker to the neck of the mannequin to make it seem like the robot is speaking. So for this stage, the medical student would be conducting the interview and the examiner would be behind one way glass answering their questions accordingly. The Carilion faculty all wanted to know if the jaw moved while it talked but at this point it does not. Future prototypes will have to include a sensor that picks up the amplitude of noise coming from the speaker and translate that into a certain degree of jaw movement.

During the interview stage it is also important for the medical students to pick up on slight emotional cues, like facial expressions and body language, in order to know where to probe further. After demonstrating the facial expression capabilities of the robot the Carilion faculty had a few comments.

> "Something else you might want to move towards is how fluid the face moves from one expression to the other."

"Sitting up, that was great because our mannequins will sit up in bed but not by themselves. You can prop them up but then they'll fall over. It's simple but really nice because now our mannequins aren't that moveable. When we move them we have to have a structure below them in order for them to sit up and sometimes the arms don't bend, it makes it difficult to dress them."

4.3.4 Physical Examination

The physical examination involves the medical student moving the joints of the mannequin and seeing where there is limited range of motion or pain in the patient. Typically, standardized patients are used for this exam because they can give direct feedback to the medical student. A standardized patient is someone who has agreed to simulate a certain behavior and to answer the medical students questions a certain way. This allows the examiner to test any situation they want without having to find somebody who is legitimately injured or sick.

Our medical mannequin can be in the upright or lying down position for this exam, depending on the type of exam being administered. Since the limbs on the robot are movable the medical student can move them while the examiner sits behind one way glass and gives verbal feedback. The Carilion faculty had a few comments about these capabilities.

"Have you thought about reproducing the deep tendon reflex at the elbows?"

"The hand movements are awesome."

"Most of the ones, as they've said, generally don't move their extremities at all. They have the speaker in the chest that can mimic coughing, so this actually would be much more realistic, and those mannequins are not cheap. So this would be much more improved if you can incorporate movement especially the eyes."

"I think this is getting to the point where you might not need a real patient to simulate some of this stuff. Like right now we have standardized patients, but you can't stick needles into them so we have plastic that you stick the needles into and do the intervention and to intubate and we have the patients to give us the

expressions and do the interview. But if we could bring the standardized patient work into the mannequin, the whole expression thing is great."

"Thy physical exam, they do all the ranges of motion and then when you're doing a test on someone to try to gauge strength, you ask them to "push against me". So if the robot could push against with a certain force that would say "You're normal" or "Oh, you're not." that would be great."

4.3.5 Visual Tests

[8] provides an extensive overview of medical tests doctors should perform to assess the physical, mental and emotional state of an incoming patient. The most abundant area for information in the face comes from the eyes and therefore we aim to simulate as many of these tests as possible. The following tests are considered important areas of examination:

- Visual acuity
- Visual fields
- Conjunctiva and sclera
- Cornea, lens, and pupils
- Extraocular movements
- Fundi, including:
  - Optic disc and cup
  - Retina
  - Retina vessels

We were not able to replicate a few of these tests including conjunctiva, sclera, cornea, lens, fundi, optic disc, cup, retina and retina vessel examinations. These tests involve inspecting color or consistency of biological tissues or inspecting the inner workings of the eyes which, in our case, are cameras. Future improvements to the eyes may include mechanisms that allow the coloring of the conjunctiva and sclera to change.

4.3.5.1 Visual Acuity

Visual acuity is referred to as the "clearness of vision and depends on the sharpness of the retinal focus within the eye and the sensitivity of the interpretative faculty of the brain" [102]. The method commonly used to determine visual acuity is to have a patient sit a certain distance

from a Snellen chart and then ask them to read the smallest possible line of text. A reading of 20/40 would mean that the patient can see a line of text at 40 feet that a person with normal vision could read at 20 feet.

The Snellen chart used in this examination is shown in Appendix D. In order for the robot to recognize letters a library, or series of templates, must be created that contain all the possible characters that will be read. Labview Vision Assistant 2010 has a built in function that allows you to take an image and train it to be interpreted as a character. This is known as Object Character Recognition or OCR. For example, I could load the silhouette of a cat into the vision assistant and train Labview to recognize this arrangement of pixels as the letter "C". So images of all 26 letters of the alphabet and numbers 0 – 9 were loaded into the vision assistant and trained to represent their respective characters.

The difficulty in this application is unwanted interaction with the background. Labview naturally wants to identify everything that could potentially be a character. So to compensate for this, the acuity test was performed against a solid-colored wall. The robot looks at the current frame of video and scans every pixel and associates a score (0 – 1000) to everything that may be a match. A threshold can be set in order to help eliminate background noise so that only matches with a score of 800 or more, for example, may pass as a character. Using the Microsoft HD 6000 webcam full resolution we were able to achieve a visual score of 20/50 which is fairly poor for many people. This may be improved by utilizing higher resolution cameras or more advanced background filtering. By altering which row of above the bottom the robot is reading, we can simulate various levels of visual acuity.

4.3.5.2 Visual Fields by Confrontation

The point of a visual field test is to determine the existence and boundaries of a defect in someone's range of view. The visual field test is performed by asking the patient to stare at the examiner while covering one eye. The examiner then moves his/her hand in and out of the patient's field of view while the patient lets the examiner know when their hand comes back into view. The field of view is broken down into four quadrants: up, down, left and right. Common patterns of defects and their associated names can be seen in figure 4.13. Labview Vision Assistant 2010 was utilized again to create a base code for this examination. We used an orange

ball for recognition since it is easier to distinguish the ball from the background. A template was made for the color and shape of the ball and just like the OCR described in the previous section. The image was read and scanned for a match to the template. A score was associated with each match, then the X and Y pixel coordinates of the highest match were output as the position of the ball. These coordinates differentiate between the four quadrants of one's visual field. The examiner tests for defects by comparing the patient's field of view to their own. This poses a problem for our robotic simulator because, as mentioned earlier, the field of view is only 42^0 whereas a typical human can see up to 170^0 horizontally and 100^0 vertically. To compensate for this, the medical student should step back about 8 feet in order for the fields of view to match up.

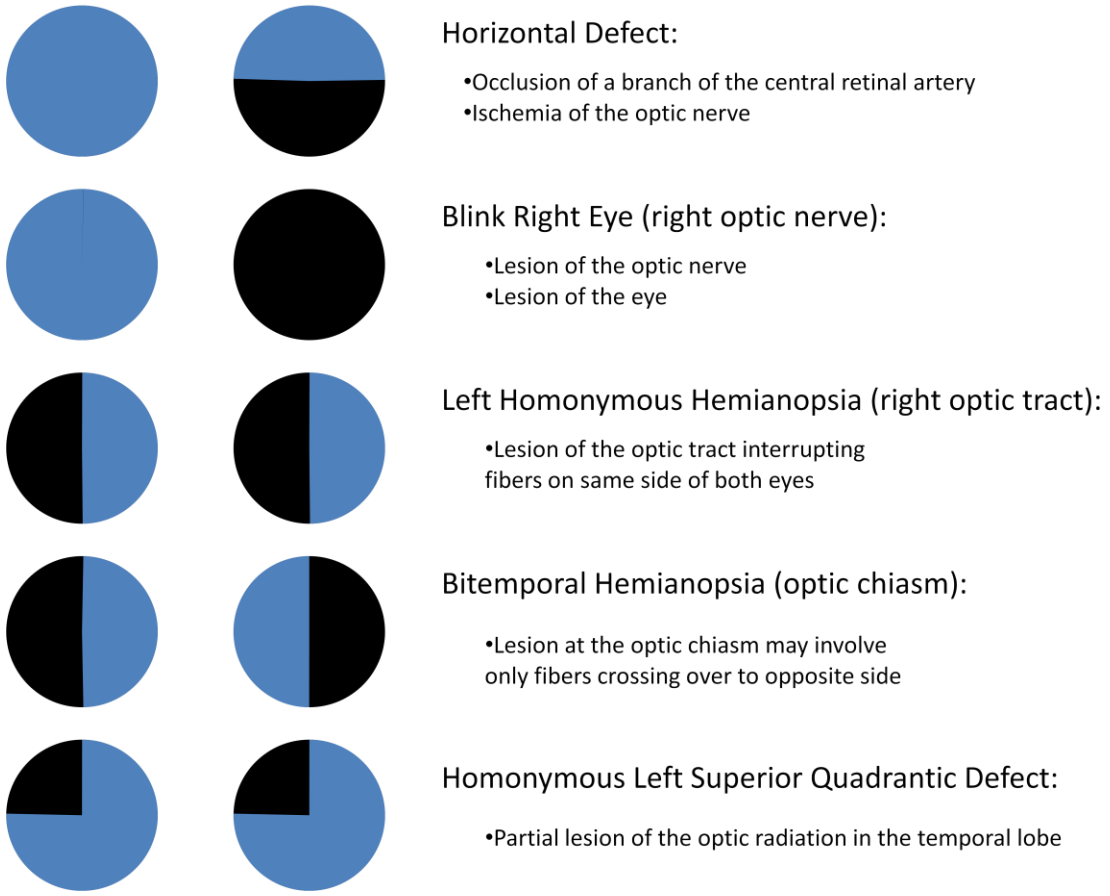

Figure 4.13: Visual field defects and their explanations.

4.3.5.3 Pupil Characteristics

Pupil characteristics include size, shape, symmetry and reaction to light. Typical sizes of human pupils range from 1 to 7mm in diameter where the average is between 3 and 5 in normal lighting. The iris shudder we purchased has a maximum inner diameter of 5mm thus fitting biological requirements. The shape of a normal pupil is circular and since our shudder could not modify its shape we excluded this characteristic from our simulation. Symmetry means having the same diameter pupil for both eyes and since our shudders are actuated independently, this is something we can simulate. Reaction to light is the most difficult test since it is a reaction, therefore, we need some type of feedback about relative lighting. The human pupil constricts when it senses an excess of light in order to prevent damage to the retina. We replicated this by taking the current frame of a video stream and applying a grayscale-intensity filter. This filter takes the grayscale values for every pixel in the image and returns an average value. If we set the threshold at a certain level we can program the robot to know when it has received "too much light" and dilate the pupils accordingly. Doctors look for two reactions: the direct reaction, where the pupil constricts in the eye exposed to light, and the consensual reaction, where the pupil constricts in the opposite eye. An extensive list of pupillary abnormalities with their descriptions and causes is presented in [8].

4.3.5.4 Extraocular Muscles

The extraocular muscles control eye movement and are capable of two types of motion: smooth pursuit and saccades. Smooth pursuit is when the eyes are fixated upon an object while it is moving in their visual fields. Saccades are the rapid movements from one fixation point to another. Saccadic movements can be observed while reading as the eyes quickly move from one series of words to the other. While examining the extraocular muscles, doctors look for a few things:

- Normal conjugate movements in each direction
- Nystagmus, a fine rhythmic oscillation of the eyes
- Lid lag as the eyes move from up to down

Doctors perform the test by sweeping through the six cardinal directions of gaze and ask the patient to follow an object they are holding. Starting to the extreme right, the examiner will move upwards, then downwards and then travel to the extreme left and repeat. An extensive list of dysconjugate gazes with their descriptions and causes is presented in [8].

In order to replicate this examination we first needed to establish a template of an object that will be tracked. In this case again the orange ball mentioned earlier was used. As before, Labview Vision Assistant 2010 was used to create the code for visual filtering. The current frame of the video feed was searched for the best match of template and the program gives a positive reading with coordinates if the match is above a certain value or threshold. We implemented a proportional control scheme which takes the difference between the center of the image and the object and multiplies it by a gain value. This product is then added to the current position of the motors controlling the eyes, thus moving the visual field toward the object. A deadband was used so that when the object is near the center of the image, the motors will not "jitter" back and forth. The deadband was a circular region around the center of the image where we specify the object as "close enough" to the center. While in the deadband the motors are instructed to do nothing until the object leaves again. There have been some computer processing issues while running the cameras at full resolution where the eyes would become very jittery while moving. This was solved by reducing the camera resolution from 1280x720 to 320x240 pixels thus increasing the speed of the overall loop and smoothing out most of the motion. The eyes were able to accurately track the orange ball with a velocity of about 60 degrees per second.

We ended up testing ocular muscles, visual fields and papillary reaction during the demo. Before the faculty arrived we had to create a new template for tracking and set a new threshold for dilation since the lighting was different there from our lab. After performing the visual tests the Carilion faculty had several comments.

"Can you move one eye one way and one eye the other way?"

"I've never had anyone play with the eyes, or the ability to track. Now I've never played with the more expensive mannequins, but I've never seen this before."

In future prototypes it would be important to separately drive the left to right motion of each eye, that way we could simulate convergence and divergence, or focusing on objects that

are coming closer or heading away from the face. Also, the faculty wanted to see faster tracking so future programming would have to include a way to speed up the loop for faster data acquisition. Also, changing the feedback controller from a proportional (P) to a PI or PID would help increase speed and reduce some choppiness.

4.3.6 Drug Delivery

The faculty at Carilion were shown the pullout monitor that displayed vital sign readouts. This is a fairly standard feature with most medical mannequins so this type of technology is well developed. They mentioned that we should work on creating a more random signal since no patient actually has a perfectly rhythmic heartbeat. They also suggested using a larger selection of drugs which is something we plan to continue working on. They were, however, impressed with the use of RFID instead of barcodes. They said it made it a lot easier and more realistic than before. Future prototypes should, however, consider going from computer generated signals to measured signals so that forces on the body, such as those during CPR, have a direct impact on vital sign readouts.

4.3.7 Additional Systems

The faculty at Carilion also identified several important systems that could be included to increase the functionality of our mannequin.

> "What about intubating with a tongue that could swell up?"
>
> "You may want to think about covering the arm and building inter IVs and central lines to administer drugs or IO. If you have a crashing patient with some of those drugs, at some point someone may want to do an IO and follow it up with a central line."
>
> "That's another thing, the whole urinary catheterization because you can draw back urine that could be bloody, too brown, too clear etc."
>
> "The other thing is chest tubes. Usually these simulations are not good on the full body mannequins. So on the side of the chest they try to cut in between the ribs

and insert a big tube then fluids/air comes out. But on the mannequins there are no ribs, there's just a small port and the doctor knows to stick the tube there."

"Replicating internal noises is very important like weezing, crackling and heart murmers."

These capabilities are certainly attainable and are something that will be incorporated into future work.

Chapter 5

Conclusions

5.1 Summary

A robotic medical simulator with important capabilities identified by the training staff at Carilion Clinic was designed, fabricated and tested. It is believed that this simulator will enhance the learning experience of medical students and nurses by providing them a more realistic simulation. Current medical mannequins lack human-like movement and functionalities such as facial expressions, moving limbs and various features in eyes. Thus, this thesis devoted significant effort towards incorporating these basic simulation necessities into the full-body mannequin.

Chapter I of this thesis provided a brief history of medical mannequins. Extensive literature survey was conducted on existing robotic hands and faces. Specific areas for improvement and important design considerations were discussed. An overview of biomimetic actuators was presented which was used to identify the potential solutions for our robotic medical simulator.

Chapter II first provided an in-depth comparison of existing actuator technologies. It was concluded that NiTi shape memory alloy (SMA) meets the requirements in several aspects including energy density, volume, drive voltage and a number of other important parameters. However, the biggest drawback of SMA was the long thermal cycle. We attempted to resolve this problem by developing techniques based upon active cooling. Low / high speed air, fluid quenching, heat sink and thermal gel were all tested to increase the frequency response of SMA. For 100 μm diameter SMA wires actuators, fluid quenching improved the response time from ~1.6 seconds to ~0.2 seconds but cycling water would be too difficult to implement in practical conditions. High speed air cooling was then considered as the best option since the air can dissipate into the ambient air. However, the addition of vacuum pump and casing reduces the energy density to a level which is comparable to commercial servo motors. Since servo motors

are cheap, well understood and easily controlled we decided that they would serve as the optimal actuator in our system until further advancement can be made in the field of smart materials.

Chapter II then discussed the design, fabrication and validation of our robotic hand, elbow and shoulder. A hand with 23 DOF which weighs less than a human hand was developed. A hand with many degrees of freedom was necessary since our benchmark for success was demonstrating the ability to type on a keyboard. Since typing is one of the most dexterous tasks the human hand can perform, it is safe to assume that if the hand types then it will also be able to perform most other activities of daily living such as opening doors, reaching object and tying shoes. This is important to us because we want the hand to do more than simply supplement facial expressions and other body language. Kinematics of the fingers was optimized using dynamic simulation software to closely match that of a human. The Denavit-Hartenberg method was used to develop spatial relationships between joints in order to implement an inverse kinematic control algorithm. A typing speed of 20 words per minute was achieved with a single hand and an expected 33 words per minute is achievable if two hands were utilized. A single degree of freedom elbow and two degree of freedom shoulder were also designed and fabricated. The elbow was capable of lifting 20 lbs and the shoulder was designed to lift 5 lbs from the hand. These joints were also designed to stay within the confines of human form.

Chapter III described the design, fabrication and testing of the robotic face, eyes and neck. An interview with Carilion Clinic faculty members revealed that the action units responsible for grimacing are the most important to replicate. Since this expressions uses action units associated with other expressions, we include other action units that make other generic facial expressions, like happiness and sadness. A skull was developed using a plaster mold which was then 3D scanned and transformed into a CAD model. This model was modified to create structures for motor mounts, electronics and the eyes. A silicone skin that forms the external layer covers the skull and attached to the motors via wires. The skin was designed and optimized to match the thickness of human skin. A pair of eyes were developed that house high resolution cameras as well as iris shudder mechanisms to simulate papillary reaction. The eyes were capable of reading text, identifying and tracking objects which help in simulating certain neurological tests that doctors can perform. An analysis of the facial expressions was performed using the graphical facial expression analysis and design (GFEAD) technique. This method

identified areas where improvements could be made in creating facial expressions by relocating sinking points and reorienting motors within the skull. The basic expressions, happy, sad, angry, surprised, suspicious, disgusted and sarcastic were all simulated and successfully identified by taking statistical data from 49 random participants. Chapter III ends with the design and characterization of the Stewart platform based neck design. This type of mechanism allows all of the human DOF to be replicated in our system. Range of motion and dimension were found to be similar to that of a human.

Chapter IV discusses the design and integration of the remaining systems needed to complete the full body humanoid medical simulator. A mobile test bed was designed to make the system easy to transport as well as to house all the necessary equipment such as power supplies and computers. A torso was designed to allow the body to swivel between two positions: lying down and sitting up. The torso also allows all the cables to run from the equipment in the bed to their respective components in the body. A lightweight pair of legs was developed to assist the simulation of a combative patient where the limbs would flail randomly. Simulated vital signs can be monitored and altered by administering different types of drugs. The drug delivery system consists of RFID readers in the elbows and thighs with corresponding tags in syringes. We successfully simulated the changes in respiratory rate, heart rate and blood pressure that several commonly used drugs would produce. A CPR sensor was fabricated with direct feedback about if the correct pressure has been applied. The sensor self-calibrates before every run in order to eliminate sensor-drift. Patellar (knee) reflexes were replicated using piezoelectric sensors at the knees where as pressure is applied the legs will kick. A fully integrated system was presented to the faculty members at Carilion Clinic where medical personnel had the chance to perform an evaluation. A novel and easy to use interface was developed which allowed the examiner to control every aspect of the simulation. The control methodology utilizes a series of case structures that allow the program to use only parts of the code that are necessary which significantly increases the speed of the main loop. This helps in improving the reaction time of, for example, the knee reflex and vision tracking actions. Several quotes from the faculty members point out areas that were well designed as well as areas that should be augmented with additional medical capabilities.

5.2 Future Work

After fabricating and testing the completed system, we realized there are several areas that could be improved through redesign. Since the hand was fabricated from rapid prototyped plastic, its fracture strength was very low. Future designs should be constructed from more resilient materials such as aluminum or steel and should be able to survive an impact force of several Gs. The linear actuator that was chosen for the elbow was slightly long which makes the overall arm length longer than that of an average human. Since the entire stroke length of this actuator was not utilized, a shorter lead length can be used. In order to successfully create a three DOF shoulder without significantly increasing the weight of the upper body, the stepper motors should be replaced with brushless DC motors. Several motors and gear heads exist that are half the weight with twice the torque output of the motors that are currently used in the upper body. Using brushless DC motors would necessitate encoders to be installed at each joint but the reduced weight, noise and size would compensate for this change.

The location of motors in the skull should be slightly redesigned in order to prevent the wires from experiencing sharp turns before exiting the skull. In particular, the motors in the jaw should be moved to the back of the skull and use Bowden cables to attach to their sinking points (since the jaw and skull are connected at a movable joint). This allows the jaw to be redesigned for the addition of an intubating mechanism which allows students to practice inserting breathing tubes down a patient's throat. The eyes should include an additional motor which allows them to be driven left and right independently. This lets the eyes converge and diverge while tracking as the depth of an object changes. When all of the components were integrated, the system became tightly packed. This created electromagnetic interference (EMI) issues; thus, shielding precautions had to be taken. This shielding was retrofitted but not all of the effects were eliminated. Proper modeling and redesign of the whole system could create a much more effective EMI blocking strategy. Computing power becomes an issue when the program is processing data from the cameras which is due to the large volume of pixel data. Efforts should be made to further reduce the camera resolution as well as utilizing a faster program since Labview is intended to be used as a development tool.

Other systems that could be included which our sponsors at Carilion Clinic have pointed out are:

- Smoother transition between facial expressions
- Synchronization of jaw movements with speaker output
- Covering arms with skin and building inter IVs and central lines to administer drugs or IO
- More ways of restraining the combative patient
- Needle insertion capabilities
- Urinary catheterization
- Chest tube simulations
- Tongue swelling
- Internal noises such as breathing, digestion and heart sounds

5.3 Other Applications

The main objective of this thesis was to create a medical mannequin that had features that current mannequins do not have in order to enhance the learning experience of medical students. In doing so, we also created a system that is not limited just to this market. A robotic system that looks similar to a human being with similar degrees of freedom, ranges of motion and force output could interact with people on a regular basis, performing tasks that were once only believed to be capable by humans. For instance, as people age they may lose the ability to take care of themselves so they rely on help from others to perform activities of daily living (ADLs) such as dressing themselves, opening doors, cooking or reaching objects from kitchen shelves. The robotic humanoid system developed through this research has hands as dexterous as a human and has the range of motion and force output in the shoulder and elbow to assist in many ADLs. More work is required to ensure that the robot operates safely in close quarters with people. Sensors would have to be installed to detect if the robot hits an object or another person then it should be able to stop the motion immediately to avoid damaging something. A combination of visual data and a layout of the house would be used to navigate the robot around objects and through rooms. Random object avoidance algorithms would have to be developed to control the legs to go around or step over objects of differing heights. This means a robust stereo

vision system and walking legs would have to be developed which presents the greatest challenge for this application.

Another potential application would be to use the humanoid to perform a mundane repetitive task such as carrying out a long-term experiment. At Virginia Tech, a Global Magnetoelectric Measurement System (GMMS) exists which measures magnetoelectric properties of single phase and composite materials. These material samples can be shipped from anywhere in the world and the experiment is controlled completely over the internet. This prevents researchers from having to take a flight to use equipment that may not be available to them otherwise. The only area where a human must interfere in the process is taking the sample from where it is delivered to mounting it in the experimental setup. If we used our humanoid robot to perform this step in the process we would achieve complete autonomy in the experimental setup. In this case, the robot would not have to be very mobile if the material samples were delivered to a loading station that the robot could access. The humanoid would determine the orientation of the box using vision algorithms and open it. The sample would have to be packed a certain way to make it easy for the robot to grip it properly and place it in the experimental setup. The difficulty in this application is the precision placement necessary to allow the proper clearance between the magnetic equipment and sample. The less moving joints in the humanoid the better since small positional errors add up quickly in multi-jointed systems.

Bibliography

[1]. Anton, M, et al. "Towards a biomimetic EAP robot." Proc. Towards the Autonomous Mobile Robots (2004): 1-7.

[2]. Ashrafiuon, H, M Eshraghi and M H Elahinia. "Position control of a three-link shape memory alloy actuated robot." Journal of Intelligent Material Systems and Structures 17 (2006): 381-392.

[3]. Associates, Henry Dreyfuss. The measure of man and woman: Human factors in design. New York: Wiley, 2002.

[4]. Astin, A D, et al. "Finger force capability: measurement and prediction using anthropometric and myoelectric measures." Thesis submitted to the faculty of the Virginia Polytechnic Institue and State University (n.d.).

[5]. Beira, R, et al. "Design of the robot-cub (iCub) head." IEEE ICRA (2006): 94-100.

[6]. Bell, C. The hand; Its mechanism and vital endowments as evincing design. London: William Pickering, 1834.

[7]. Bergamasco, M, F Salsedo and P Dario. "A linear SMA motor as direct-drive robotic actuator." Proc. of IEEE Conference on Robotics and Automation 1 (1989): 618-623.

[8]. Bickley, L S and P G Szilagyi. Bate's guide to physical examination and history taking. Philadelphia, PA: J. B. Lippincott Company, 2009.

[9]. Cabas, R, L M Cabas and C Balaguer. "Optimized design of the underactuated robotic hand." IEEE Int. Conf. on Robotics and Automation (2006).

[10]. Caffaz, A et al. "The DIST-Hand, an anthropomorphic fully sensorized dexterous gripper." IEEE Conf. on Humanoids (2000).

[11]. Carrozza, M C, G Cappiello and S Micera. "Design of a cybernetic hand for perception and action." Biol. Cybern. (2006): 629-644.

[12]. Cassin, B and S Solomon. Dictionary of eye terminology. Gainsville, FL: Triad Publishing Company, 1990.

[13]. Chang, L Y and Y Matsuoka. "A kinematic thumb model for the ACT hand." Proc. of IEEE International Conf. on Robotics and Automation (2006): 1000-1005.

[14]. Choi, J M, H M Son and Y J Lee. "Design of biomimetic robot-eye system with single vari-focal lens and winding type SMA actuator." International Conference on Control Automation and Systems (2008): 14-17.

[15]. Clauser, C E, J T McConville and J W Young. "Weight, volume and center of mass of segments of the human body." AMRL TR 69-70 (Wright-Patterson Air Force Base (NTIS No. AD-T10 622)).

[16]. Controzzi, M, C Cipriani and C Carrozza. "Mechatronic design of a transradial cybernetic hand." IEEE/RSJ Int. Conf. on Intelligent Robots and Systems (2008).

[17]. Cooper, J B and V R Toqueti. "A brief history of the development of mannequin simulators for clinical education and training." Qual Saf Health Care (2004): i11-i18.

[18]. Cummins, R O, et al. "Improving survival from sudden cardiac arrest: the "chain of survival" concept. A statement for health professionals from the Advanced Cardiac Life Support Subcommittee and the Emergency Cardiac Care Committee, American Heart Association." Circulation 1991, 83:1832-1847 (n.d.).

[19]. Delaunay, F, J de Greeff and T Belpaeme. "Towards retro-projected robot faces: an alternative to mechatronic and android." IEEE Int. Symp. on Robot and Human Interactive Communication (2009): 306-311.

[20]. Diftler, M A and R O Ambrose. "Robonaut: a robotic astronaut assistant." 6th Int. Symp. on Artificial Intelligence and Robotics and Automation in Space (2001).

[21]. DiSalvo, C, et al. "All robots are not created equal: the design and perception of humanoid robot heads." Proc. of Conf. on Designing Interactive Systems, Processes, Practices, Methods, and Techniques (2002): 25-28.

[22]. Edin, B B, et al. "A bio-inspired approach for teh design and characterization of a tactile sensory system for a cybernetic prosthetic hand." IEEE Int. Conf. on Robotics and Automation (2006).

[23]. Ekman, P and W V Friesen. Facial action coding system. Palo Alto: Consulting Psychologists Press, 1978.

[24]. ElKoura, G and K Singh. "Handrix: animating the human hand." Eurographics/SIGGRAPH Symp. on Computer Animation (2003).

[25]. Fischer, B and R Boch. "Saccadic eye movements after extremely short reaction times in the monkey." Brain Res (1983): 21-26.

[26]. Folgheraiter, M and G Giuseppina. "Blackfingers: an artificial hand that copies human hand in structure, size and functions." IEEE Conf. on Humanoids (2000).

[27]. Foner, L. "What's agency anyway? a sociological case study." Proc. Int. Conf. on Autonomous Agents (1997).

[28]. Fridlund, A. Human facial expression: An evoluctionary view. San Diego: Academic Press, 1994.

[29]. Fukaya, N, et al. "Design of the TUAT/Karlsruhe humanoid hand." IEEE/RSJ Int. Conf. on Intelligent Robots and Systems (2000).

[30]. Fukuda, T, et al. "Facial expressive robotic head system for human-robot communication and its application in home environment." Proceedings of the IEEE (2004): 1851-1865.

[31]. Full, R J and K Meijer. "Metrics of natural muscle." SPIE (2001): 67-83.

[32]. Gao, B, et al. "Development of a low motion-noise humanoid neck: Statics analysis and experimental validation." IEEE Int. Conf. on Robotics and Automation (2010): 1203-1208.

[33]. Hashimoto, M, C Yokogawa and T Sadoyama. "Development and control of a face robot imitating human musclar structures." Intelligent Robots and Systems (2006): 1855-1860.

[34]. Hashimoto, T, et al. "Development of the face robot SAYA for rich facial expressions." SICE-ICASE (2006): 5423-5428.

[35]. Hirth, J, N Schmitz and K Berns. "Emotional architecture for the humanoid robot head ROMAN." IEEE Int. Conf. on Robotics and Automation (2007): 2150-2155.

[36]. Hong, D, M Ingram and D Lahr. "Whole skin locomotion inspired by amoeboid motility mechanism." ASME Journal of Mechanisms and Robotics 1 (2009).

[37]. Hornyak, T N. Loving the machine. Yokyo, New York, London: Kodansha International, 2006.

[38]. Howe, R D, D A Kontarinis and W J Peine. "Shape memory alloy actuator controller design for tactil displays." Proc. of IEEE Conference on Decision and Control 4 (1995): 3540-3544.

[39]. Hugh, H and K Roy. "New horizons for orthotic and prosthetic technology: artificial muscle for ambulation." Proc. SPIE's Smart Structures and Materials: Electroactive Polymer Actuators and Devices 5385 (2004): 1-9.

[40]. Huh, S, et al. "Development of a piano-playing robot system." 11th Int. Conf. on Mechatronics Technology (2007): 5-9.

[41]. Hunter, I W, et al. "Fast reversible NiTi fibers for use in microrobotics." Proc. of IEEE Conference on Micro Electro Mechanical Systems (1991): 166-170.

[42]. Incropera, F P, et al. Fundamentals of heat and mass transfer. Hoboken, NJ, 2007.

[43]. Ishiguro, H and S Nishio. "Building artificial humans to understand humans." Journal of Artificial Organs (2007): 133-142.

[44]. Jacobsen, S C et al. "The UTAH/M.I.T. dexterous hand: work in progress." Int. J. Robot 3 (1984): 21-50.

[45]. Jayender, J, et al. "Modeling and gain scheduled control of shape memory alloy actuators." Proc. of the 2005 IEEE Conference on Control Applications (2005).

[46]. Jones, L A and J J Lederman. Human Hand Function. New York: Oxford University Press, 2006.

[47]. Kaneko, K, et al. "Cybernetic human HRP-4C." IEEE-RAS Int. Conf. on Humanoid Robots (2009): 7-14.

[48]. Kawasaki, H, T Komatsu and K Uchiyama. "Dexterous anthropomorphic robot hand with distributed tactil sensor: Gifu hand II." IEEE/ASME Trans. mechatronics 2 (2002): 296-303.

[49]. Kidd, C and C Breazeal. "Effect of a robot on user perception." Proc. IEEE/RSJ Int. Conf. on Intelligent Robots and Systems (2004).

[50]. Kim, H, et al. "Design of an anthropomorphic robot head for studying development and learning." Proc. IEEE Int. Conf (2004).

[51]. Kornbluh, R, et al. "Ultrahigh strain response of field-actuated elastomeric polymers." Smart Stru. Mat. (2000): 51-64.

[52]. Kozima, H and H Yano. "A robot that learns to communicate with human caregivers." Proc. Int. Wksp. Epigenetic Rob (2001).

[53]. Laschi, C, et al. "Design and development of a soft actuator for a robot inspired by the octopus arm." The 11th International Symposium on Experimental Robotics (2009): 25-33.

[54]. Lee, D W, et al. "Development of an android for emotional expression and human interaction." The International Federation of Automatic Control (2008): 4336-4337.

[55]. Lee, J K and C Breazeal. "Human social response toward humanoid robot's head and facial features." CHI: Work-in-Progress (2010).

[56]. Leo, D J. Engineering analysis of smart material systems: analysis, design, and control. New York: John Wiley and Sons, 2007.

[57]. Lin, J, Y Wu and T S Huang. "Modeling the constraints of human hand motion." Proc. 5th Annual Federated Laboratory Symp. (2001).

[58]. Liu, H et al. "The modular multi mensory DLR-HIT-hand." Mech. Mach. Theory 42 (2007): 612-625.

[59]. Liu, K, J M Fitzgerald and F L Lewis. "Kinematic analysis of a stewart platform manipulator." IEEE Transactions on Industrial Electronics (1993): 282-293.

[60]. Loh, C S, H Yokoi and T Arai. "Improving heat sinking in ambient environment for the shape memory alloy (SMA)." Proc. of IEEE Conference on Intelligent Robots and Systems (2005): 3560-3565.

[61]. —. "New shape memory alloy actuator: Design and application in the prosthetic hand." Proc. of the 27th Annual Conference of the IEEE Engineering in Medicine and Biology (2005): 1-4.

[62]. Luchetti, T, et al. "Electrically actuated antiglare rear-view mirror based on a shape memory alloy actuator." Journal of Materials Engineering and Performance 18 (2009): 717-724.

[63]. Luo, Y, et al. "A shape memory alloy actuator using peltier modules and R-phase transition." Journal of Intelligent Material Systems and Structures 11 (2000): 503-511.

[64]. Madden, J D. "Mobil robots: Motor challenges and material solutions." Science 318 (2007): 1094-1097.

[65]. Madden, J D, et al. "Artificial muscle technology: physical principles and naval prospects." IEEE J. Ocean. Eng 3 (2004): 706-728.

[66]. Moallem, M and V Tabrizi. "Tracking control of an antagonistic shape memory alloy actuator pair." IEEE Transactions on Control Systems Technology 17 (2009): 184-190.

[67]. Napier, J. Hands. Princeton, NJ: Princeton University Press, 1993.

[68]. Nascimento, M M S F and C J Araujo. "Electro-thermomechanical characterization of Ti-Ni shape memory alloy thin wires." Materials Research 9 (2006): 15-19.

[69]. Oh, H U, K Izawa and S Taniwaki. "Development of variable-damping isolator using bio-metal fiber for reaction wheel vibration isolation." smart Materials and Structures 14 (2005): 928-933.

[70]. Oh, Jun-Ho, et al. "Design of android type humanoid robot Albert HUBO." IEEE/RSJ Int. Conf. on Intelligent Robots and Systems (2006): 1428-1433.

[71]. O'Neill, P A. "Myoelectric signal characteristics from muscles in residual upper limbs." IEEE Trans. Rehabil. Eng. 2 (1994): 266-270.

[72]. Otsuka, K and C M Wayman. Shape memory materials. Cambridge, UK: Cambridge University Press, 1999.

[73]. Ott, Ch, et al. "A humanoid two-arm system for dexterous manipulation." IEEE-RAS Int. Conf. on Humanoid Robots (2006): 276-283.

[74]. Park, I W, et al. "Mechanical design of humanoid robot platform KHR-3 (KAIST Humanoid robot-3: HUBO)." IEEE-RAS Int. Conf. on Humanoid Robots (2005): 321-326.

[75]. Pelrine, R, et al. "Applications of dielectric elastomer actuators." Smart Structures and Materials 4329 (2001).

[76]. Pons, J L, et al. "Comparison of different control approaches to drive SMA actuators." Proc. of the IEEE Conference on Advanced Robotics (1997): 819-824.

[77]. Powers, A and S Kiesler. "The advisor robot: Tracing people's mental model from a robot's physical attributes." Proc. ACM Conf. on Human-Robot Interaction (2006): 218-225.

[78]. Qiu, J, et al. "High-speed response of SMA actuators." Proc. of International Journal of Applied Electromagnetics and Mechanics 12 (2000): 87-100.

[79]. Reynaerts, D and H VanBrussel. "Development of a SMA high performance robotic actuator." Proc. of the IEEE Conference on Advanced Robotics 1 (1991): 61-66.

[80]. Rhee, C, et al. "Door opening control using the multi-fingered robotic hand for the indoor service robot." IEEE Int. Conf. on Robotics and Automation (2004).

[81]. Robinson, D A. "The mechanics of human saccadic eye movement." Journal of Physiology (1964): 245-264.

[82]. Rodrigues-Cheu, L E and A Casals. "Sensing and control of a prosthetic hand with myoelectric feedback." 1st IEEE/RAS-EMBS Int. Conf. on Biomedical Robotics and Biomechatronics (2006).

[83]. Russell, R A and R B Gorbert. "Improving the response of SMA actuators." Proc. of the IEEE Conference on Robotics and Automation 3 (1995): 2299-2304.

[84]. Shiraishi, Y, et al. "Development of an artificial myocardium using a covalent shape memory alloy fiber and its cardiovascular diagnostic response." Proc. of the 27th Annual conference of the IEEE Engineering in Medicine and Biology (2005): 406-408.

[85]. Spexard, T P, M Hanheide and G Sagerer. "Human-oriented interaction with an anthropomorphic robot." IEEE Transaction on Robotics (2007): 852-862.

[86]. Spong, M W and M Vidyasagar. Robot Dynamics and Control. New York: Wiley, 1989.

[87]. Tadesse, Y and S Priya. "Determination of the sinking and terminating points of action unit on humanoid skull through GFEAD." Proc. SPIE (2011).

[88]. Tadesse, Y, D Hong and S Priya. "Twelve degree of freedom baby humanoid head using shape memory alloy actuators." Journal of Mechanisms and Robotics (2011).

[89]. Tadesse, Y, et al. "Polypyrrole-polyvinylidene difluoride composite stripe and zigzag actuators for use in facial robotics." Smart Mater. Struct. 17 (2008).

[90]. Tadesse, Y, K Subbarao and S Priya. "Realizing a humanoid neck with serial chain four-bar mechanism." Journal of Intelligent Material Systems and Structures (2010): 1169-1191.

[91]. Tadesse, Y, W G Robert and S Priya. "synthesis and cyclic force characterization of helical polypyrrole actuators for artificial facial muscles." Smart. Mater. Struct 18 (2009).

[92]. Toshima, I, H Uematsu and T Hirahara. "A steerable dummy head that tracks three-dimensional head movment: Telehead." Acoustical Science and Technology (2003): 327-329.

[93]. Trivedi, D, et al. "Soft robotics: Biological inspiration, state of the art, and future research." Applied Bionics and Biomechanics 3 (2008): 99-117.

[94]. Villanueva, A, et al. "Jellyfish inspired underwater unmanned vehicle." Proc. of SPIE 7287 (2009): 72871G.

[95]. Westheimer, G and S P McKee. "Visual acuity in the presence of retinal-image motion." Journal of the Optical Society of America (1975): 847-850.

[96]. Wik, L, J Kramer-Johansen and H Myklebust. "Quality of cardiopulmonary resuscitation during out-of-hospital cardiac arrest." JAMA (2005): 299-304.

[97]. www.anaheimautomation.com.

[98]. www.Gaumard.com.

[99]. www.Laerdal.com.

[100]. www.Maxonmotor.co.uk.

[101]. www.METI.com.

[102]. www.Wikipedia.com.

[103]. Zhang, W, Q Chen and Z Sun. "Passive adaptive grasp multi-fingered humanoid robot hand with high under-actuated function." IEEE Int. Conf. on Robotics and Automation (2004).

[104]. Zhao, J et al. "A five-fingered underactuated prosthetic hand control scheme." 1st IEEE/RAS-EMBS Int. Conf. on Biomedical Robotics and Biomechatronics (2006).

[105]. Zhou, B and S H Yoon. "A new phase transformation constitutive model of shape memory alloys." Journal of Smart Materials and Structures 15 (2006): 1967-1973.

[106]. Zollo, L et al. "Biomechatronic design and control of an anthropomorphic artificial hand for prosthetic and robotic applications." IEEE/ASME Trans. Mechatronics 12 (2007): 418-429.

[107]. Zupan, M, M F Ashby and N A Fleck. "Actuator classification and selection - the development of a database." Adv. Eng. Mater. 4 (2002): 933-940.

APPENDIX A: Questionnaire for facial expression recognition

	EXPRESSION						
	1	2	3	4	5	6	7
Emotion/Expression							
HAPPY							
ECSTATIC							
CONTENT							
JOYFUL							
INTERESTED							
HOPEFUL							
ANGRY							
UPSET							
AGGRAVATED							
FURIOUS							
SAD							
DEPRESSED							
MOURNFUL							
EMBARRASSED							
SHY							
GUILTY							
SUSPICIOUS							
CURIOUS							
UNTRUSTING							
SPITEFUL							
JEALOUS							
SURPRISED							
ASTONISHED							
BEWILDERED							
CONFUSED							
FEARFUL							
DISGUSTED							
BOTHERED							
DISTURBED							
OFFENDED							
SARCASTIC							
ARROGANT							
DISRESPECTFUL							

APPENDIX B: Equations for coordinates of top plate with respect to bottom plate of Stewart platform

$X_{T1} = x_T - (a * (cb * sz - cz * sa * sb))/2 + (3\text{^}(1/2) * (cb * cz + sa * sb * sz) * (a + 2 * c))/6$
$Y_{T1} = y_T + (a * ca * cz)/2 + (3\text{^}(1/2) * ca * sz * (a + 2 * c))/6$
$X_{T1} = z_T + (a * (sb * sz + cb * cz * sa))/2 - (3\text{^}(1/2) * (cz * sb - cb * sa * sz) * (a + 2 * c))/6$
$X_{T2} = x_T - (cb * sz - cz * sa * sb) * (a/2 + c/2) + (3\text{^}(1/2) * (cb * cz + sa * sb * sz) * (a - c))/6$
$Y_{T2} = y_T + ca * cz * (a/2 + c/2) + (3\text{^}(1/2) * ca * sz * (a - c))/6$
$Z_{T2} = z_T + (sb * sz + cb * cz * sa) * (a/2 + c/2) - (3\text{^}(1/2) * (cz * sb - cb * sa * sz) * (a - c))/6$
$X_{T3} = x_T - (c * (cb * sz - cz * sa * sb))/2 - (3\text{^}(1/2) * (cb * cz + sa * sb * sz) * (2 * a + c))/6$
$Y_{T3} = y_T + (c * ca * cz)/2 - (3\text{^}(1/2) * ca * sz * (2 * a + c))/6$
$Z_{T3} = z_T + (c * (sb * sz + cb * cz * sa))/2 + (3\text{^}(1/2) * (cz * sb - cb * sa * sz) * (2 * a + c))/6$
$X_{T4} = x_T + (c * (cb * sz - cz * sa * sb))/2 - (3\text{^}(1/2) * (cb * cz + sa * sb * sz) * (2 * a + c))/6$
$Y_{T4} = y_T - (c * ca * cz)/2 - (3\text{^}(1/2) * ca * sz * (2 * a + c))/6$
$Z_{T4} = z_T - (c * (sb * sz + cb * cz * sa))/2 + (3\text{^}(1/2) * (cz * sb - cb * sa * sz) * (2 * a + c))/6$
$X_{T5} = x_T + (cb * sz - cz * sa * sb) * (a/2 + c/2) + (3\text{^}(1/2) * (cb * cz + sa * sb * sz) * (a - c))/6$
$Y_{T5} = y_T - ca * cz * (a/2 + c/2) + (3\text{^}(1/2) * ca * sz * (a - c))/6$
$Z_{T5} = z_T - (sb * sz + cb * cz * sa) * (a/2 + c/2) - (3\text{^}(1/2) * (cz * sb - cb * sa * sz) * (a - c))/6$
$X_{T6} = x_T + (a * (cb * sz - cz * sa * sb))/2 + (3\text{^}(1/2) * (cb * cz + sa * sb * sz) * (a + 2 * c))/6$
$Y_{T6} = y_T - (a * ca * cz)/2 + (3\text{^}(1/2) * ca * sz * (a + 2 * c))/6$
$Z_{T6} = z_T - (a * (sb * sz + cb * cz * sa))/2 - (3\text{^}(1/2) * (cz * sb - cb * sa * sz) * (a + 2 * c))/6$

APPENDIX C: Flow diagrams of how functional states are handled in Labview.

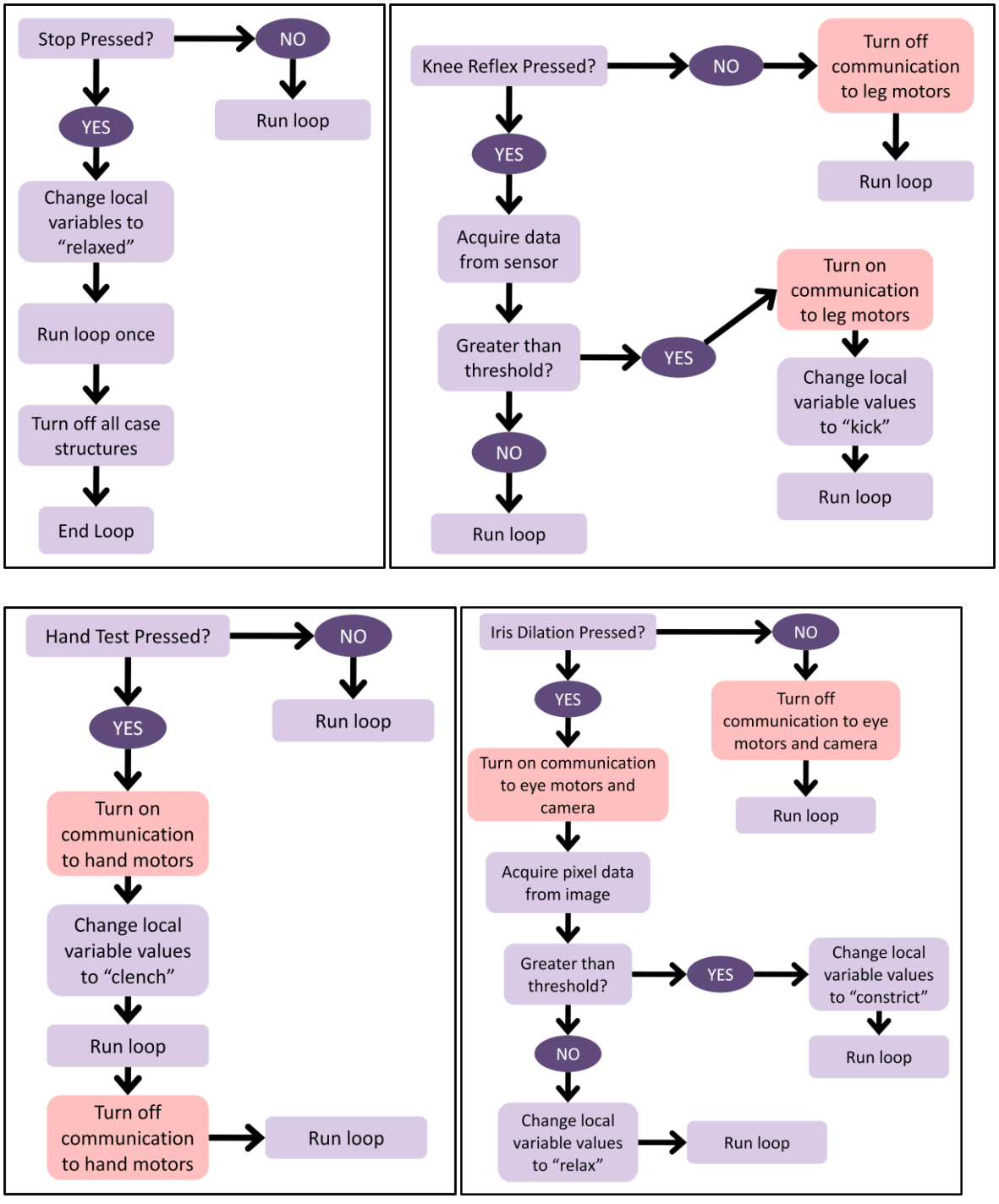

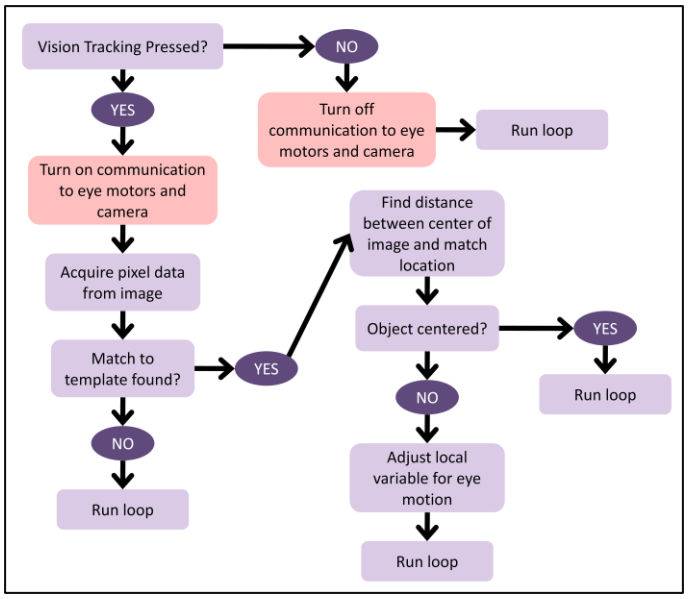
Vision Tracking Pressed?
NO
YES
Turn off communication to eye motors and camera
Run loop
Turn on communication to eye motors and camera
Acquire pixel data from image
Match to template found?
YES
Find distance between center of image and match location
Object centered?
YES
Run loop
NO
Adjust local variable for eye motion
Run loop
NO
Run loop

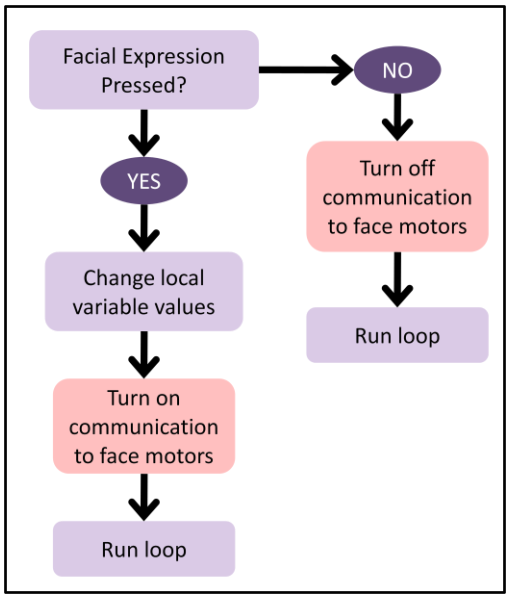
Facial Expression Pressed?
NO
Turn off communication to face motors
Run loop
YES
Change local variable values
Turn on communication to face motors
Run loop

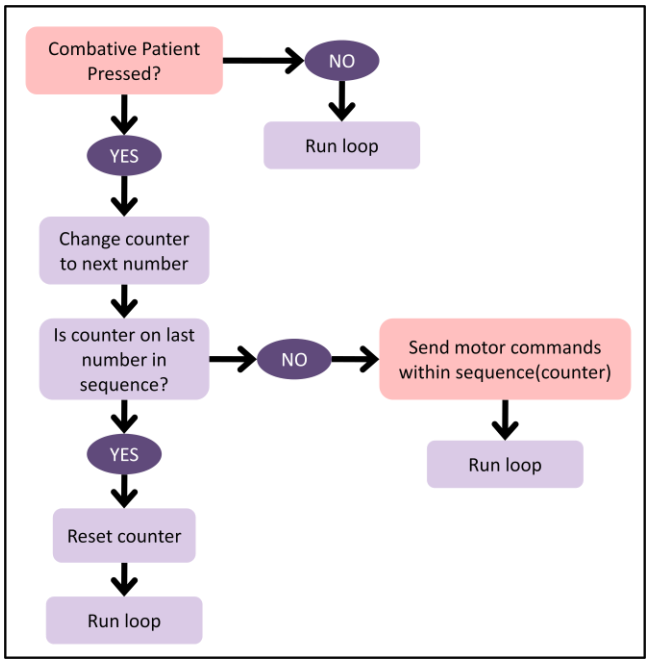
Combative Patient Pressed?
NO
Run loop
YES
Change counter to next number
Is counter on last number in sequence?
NO
Send motor commands within sequence(counter)
Run loop
YES
Reset counter
Run loop

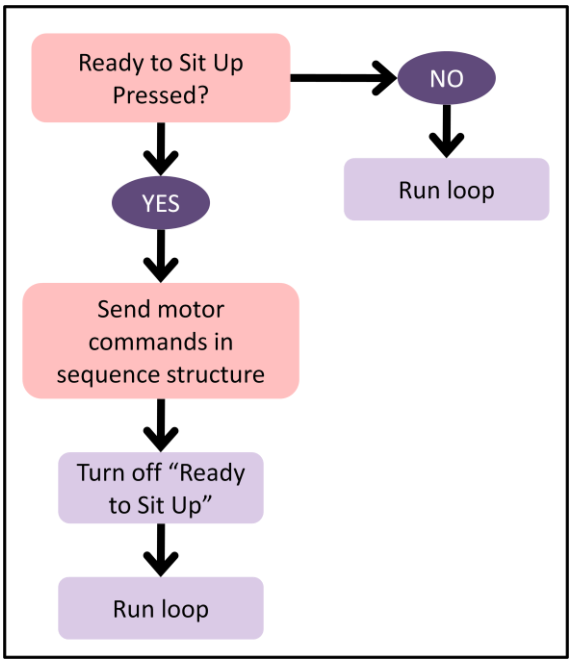
Ready to Sit Up Pressed?
NO
Run loop
YES
Send motor commands in sequence structure
Turn off "Ready to Sit Up"
Run loop

APPENDIX D: Snellen chart used for visual acuity tests